NASA
Contractor
Report
CR 170619

April 1984

User's Guide for ERB 7 MATRIX

Volume I
Experiment Description and Quality Control Report for Year 1

Richard J. Tighe
Maria Y. H. Shen

(NASA-CR-170619) USER'S GUIDE FOR ERB 7 MATRIX. VOLUME 1: EXPERIMENT DESCRIPTION AND QUALITY CONTROL REPORT FOR YEAR 1 (Systems and Applied Sciences Corp.) 197 p HC A09/MF A01 CSCL 09B G3/61

N84-31960

Unclas 21268

NASA

NASA
Contractor
Report
CR 170619

1984

User's Guide for ERB 7 MATRIX

Volume I
Experiment Description and Quality Control Report for Year 1

Richard J. Tighe
Maria Y. H. Shen

Prepared For:

NATIONAL AERONAUTICS AND SPACE ADMINISTRATION
GODDARD SPACE FLIGHT CENTER
GREENBELT, MARYLAND 20771

Prepared By:

SYSTEMS AND APPLIED SCIENCES CORPORATION
5809 ANNAPOLIS ROAD, SUITE 414
HYATTSVILLE, MARYLAND 20784

UNDER CONTRACT NO. NAS 5-28063
TASK ASSIGNMENT 03

ACKNOWLEDGEMENTS

We would like to thank Mr. Harold Soule (RDS) for providing the preprint which forms Section 1. We also thank Dr. Herbert Jacobowitz (NOAA) for the preprint in Section 2. We would like to acknowledge Mrs. Jenny Kolbe (SASC) for word processing, editing, and preparation of the User's Guide. We also thank Dr. K.L. Vasanth (SASC) and Dr. H. Lee Kyle (NASA ATR) for reviewing the document and suggesting many improvements. The computer-generated plots presented in the Science QC section were produced on the IBM 3081 at the GSFC Science and Applications Computer Center.

TABLE OF CONTENTS

TABLE OF CONTENTS
(Continued)

LIST OF TABLES AND FIGURES

LIST OF APPENDICES

ACRONYMS

AN	-	Ascending Node
CAT	-	Calibration Adjustment Table
DN	-	Descending Node
ERB	-	Earth Radiation Budget
ITCZ	-	Inter-Tropical Convergence Zone
LW	-	Long Wave
MAT	-	Master Archival Tape
NET	-	Nimbus Experiment Team
NFOV	-	Narrow Field of View
PTM	-	Platinum Temperature Monitor
SQC	-	Science Quality Control
SW	-	Short Wave
TDF	-	Trailing Documentation File
WFOV	-	Wide Field of View
NH	-	Northern Hemisphere
SH	-	Southern Hemisphere

INTRODUCTION

This guide is intended for the users of the Nimbus-7 ERB MATRIX tape. MATRIX scientific processing converts the input radiances and irradiances into fluxes which are used to compute basic scientific output parameters such as emitted LW flux, albedo, and net radiation. These parameters are spatially averaged and presented as time averages over one-day, six-day, and monthly periods. All the parameters are written on the MATRIX tape as world grids, mercator projections, and north and south polar stereographic projections.

MATRIX data for the period November 16, 1978 through October 31, 1979 are presented in this document. A detailed description of the prelaunch and inflight calibrations, along with an analysis of the radiometric performance of the instruments in the Earth Radiation Budget (ERB) experiment, is given in Section 1. Section 2 contains an analysis of the data covering the period November 16, 1978 through October 31, 1979. These two sections are preprints of articles which will appear in the Nimbus-7 Special Issue of the Journal of Geophysical Research (JGR), Spring 1984. When referring to material in these two sections, the reader should reference the JGR. Section 3 contains additional material from the detailed scientific quality control of the tapes which may be very useful to a user of the MATRIX tapes. This section contains a discussion of known errors and data problems and some suggestions on how to use the data for further climatologic and atmospheric physics studies.

Volume II contains the MATRIX Tape Specifications that provide details on the tape format and contents.

SECTION 1. THE EARTH RADIATION BUDGET (ERB) EXPERIMENT - AN OVERVIEW

THE EARTH RADIATION BUDGET (ERB) EXPERIMENT AN OVERVIEW

by

Herbert Jacobowitz
NOAA/National Environmental Satellite Data and Information Service
Washington, DC 20233

Harold V. Soule
Research and Data Systems, Inc.
Lanham, Maryland 20706

H. Lee Kyle
NASA/Godddard Space Flight Center
Greenbelt, Maryland 20771

Frederick B. House
Drexel University
Philadelphia, PA

and

The Nimbus-7 ERB Experiment Team

PREPRINT
Special Nimbus-7 Volume, Journal Geophysical Research, 1984

TABLE OF CONTENTS

TABLES

FIGURE LEGEND LIST

DEDICATION

The authors wish to dedicate this paper to S. Rangaswamy, president of Research and Data Systems, Inc., in recognition of his important contributions leading to the development of the earth radiation budget (ERB) data system. His tragic death on December 29, 1982, was a tremendous loss to all of us who worked so closely with him. Everyone who knew him was impressed by his keen wit and his depth of understanding of the problems encountered in analyzing remotely sensed data from a satellite platform. We will always miss him.

THE EARTH RADIATION BUDGET (ERB) EXPERIMENT
AN OVERVIEW

1. INTRODUCTION

The Earth Radiation Budget (ERB) instrument aboard the Nimbus-7 satellite is an experiment for providing measurements of the radiation entering and exiting the earth-atmosphere system which when completely processed and analyzed are expected to greatly enchance our understanding of weather and climate. Specifically, the objectives of ERB are to:

(1) Obtain accurate measurements of the total solar irradiance, to monitor its variation in time and to observe the temporal variation of the solar spectrum;
(2) Determine over a period of a year or more the earth radiation budget on both the synoptic and planetary scales from simultaneous measurements of the incoming solar radiation and the outgoing earth reflected and earth emitted radiation, the outgoing radiation fluxes to be determined from fixed wide angle sampling at the satellite altitude as well as from scanning narrow-angle observations of the angular radiance components;
(3) Acquire and analyze detailed observations of the angular distribution of the reflected and emitted radiation for various geographical and meteorological situations in order to develop angular distribution models for the interpretation of narrow-angle scanning radiometer measurements.

The management of the Nimbus-7 spacecraft and all the experiments on board are the responsibility of the NASA Goddard Space FLight Center (GSFC). The GSFC was also responsible for instrument procurement and development. By means of an "Announcement of Opportunity" a Nimbus Experiment Team (NET) was selected for ERB which consisted of experts in the field to aid in prelaunch planning, calibration, algorithm development, post-launch sensor performance evaluation and initial data analysis. Table 1 lists the names and affiliations of the team members.

Table 1

ERB NET Members

*Jacobowitz, H.	NOAA/NESDIS
**Arking, A.	NASA/GSFC
**Campbell, G.G.	CIRA, Colorado State U.
***Coulson, K.L.	University of California, Davis
Hickey, J.R.	Eppley Lab., Inc.
House, F.B.	Drexel University
Ingersoll, A.P.	California Inst. of Technology
**Kyle, L.	NASA/GSFC
**Maschhoff, R.H.	Gulton Industries Inc.
Smith, G.L.	NASA/LaRC
Stowe, L.L.	NOAA/NESDIS
Vonder Haar, T.H.	Colorado State University

*Elected NET Leader

**Elected Members

***Left the NET because of other committments

2. DEVELOPMENT OF ERB OBSERVATIONAL SYSTEMS

Four factors can be identified that have influenced the development of satellite instrumentation for measuring earth radiation budget:

(1) spacecraft constraints - power, data storage, mode of stabilization and satellite control;

(2) viewing geometry - fixed wide/medium field of view radiometers and scanning medium/high resolution radiometers;

(3) spectral band-pass requirements - isolation the spectrum into its shortwave ($0.2\mu m$ - $4.0\mu m$) and longwave ($5.0\mu m$ - $50.0\mu m$) components;

(4) on-board calibration - shortwave using direct solar radiation and space, and longwave using a warm blackbody source and cold space.

These factors allow a logical breakdown of ERB observational systems into three generations of instruments leading to the ERB experiment currently on Nimbus-7 satellite.

Historically, the development of ERB observational systems on low-altitude satellites has paralleled the overall advancement of rocket and spacecraft technology. Concurrently during the past two decades, the NIMBUS series of satellites were developed, providing a spacecraft platform for testing experimental concepts from 1964 through the 1970's (Raschke, et al., 1973). Interwoven among these various satellite programs were a number of scientific experiments that relate to observations of the earth radiation budget.

The first generation of ERB type sensors were flown on satellites with mid-latitude orbit inclination angles, spin/space stabilized, lifetimes of months, and with modest or no data storage capacities. Some experiments employed fixed field, hemispherical radiometers with bi-color separation of spectral regions. The first such ERB measurements were initiated with the launch of the Explorer 7 satellite on 13 October 1959 (Suomi, 1961). Other experiments utilized the spin of the

spacecraft to scan the earth with instruments having telescope optics and band-pass filters. Both fixed and scanning radiometers were on several of the TIROS satellites.

In the second generation of ERB instruments, rockets were powerful enough to inject satellites into polar, sun-synchronous orbits providing the opportunity of global data coverage every day. Spacecraft lifetimes extended to several years duration. Attitude control improved to 2 axes stabilization for the ESSA cartwheel configuration, and to 3 axes in the case of the NIMBUS series. Flat fixed field radiometers were flown on several ESSA spacecraft and later on the ITOS satellites having medium and wide field spatial resolutions. Shortwave response of instruments was monitored by direct solar calibration. Medium and high resolution scanning radiometers were flown on NIMBUS spacecraft employing a variety of band-passes in the shortwave and longwave regions of the spectrum. Longwave radiometers used a warm black source and cold space for on-board calibration. In addition, visible and infrared window radiometers on the ITOS satellites provided a wealth of ERB observations during the 1970's.

The third generation of observational systems led to the development of the complete ERB instrument. It measured separately direct solar radiation, earth reflected solar and emitted terrestrial radiation (Smith, et al., 1977 and Jacobowitz, et al., 1978). Two ERB instruments have flown on NIMBUS 6 and 7 satellites in 1975 and 1978, respectively. Both fixed field radiometers and bi-axial scanning telescopes measured the shortwave and longwave radiation exiting the earth. Ten solar channels observed the solar spectrum during each orbit. It is noteworthy that channel 10c on NIMBUS 7 provided the first time series of accurate observations of the "variable" solar constant. The ERB experiment on the NIMBUS 7 satellite continues to provide observations as of this writing, and is the subject of this paper.

3. INSTRUMENT DESCRIPTION

Three separate groups of sensors were used in the ERB aboard the Nimbus-7 which became operational in November 1978 (Jacobowitz et al., 1978). An almost identical sensor package was flown on the Nimbus-6 satellite which was launched in June 1975. A summary of these sensor details is given by Soule (1983a).

One group of ten sensors monitors the solar flux over the spectral ranges given in Table 2. Another group of four sensors monitors the earth flux seen at the satellite altitude. As noted in Table 3 these sensors accept radiation from the near ultraviolet out to 50 μm. The third group of sensors consists of relatively narrow-field-of-view (FOV) earth scanners. As Table 4 indicates, they operated in the visible through the near infrared out to the very long wavelength portion of the spectrum. Four identical telescope scanners were required to cover most of the earth viewed by the wide FOV sensors so that intercomparisons could be made. Figure 1 shows the ERB sensor assembly mounted on the Nimbus satellite.

ERB radiation measurement requirements included a fairly uniform sensitivity to a range of wavelengths from 0.3 to 50.0 μm and a linear response to changes in irradiance levels of several orders of magnitude. In addition, an excellent long-term (years) stability of detector response in a space environment was required. Thermopile detectors were selected for the solar and fixed earth-viewing channels 1 through 14 primarily because in addition to having the desired spectral sensitivity, they also had the required response time capability. Pyroelectric sensors were used for the scanning channels 15 through 22 because of their very short response time.

3.1 Solar Channels

Figure 2 shows a cross-sectional drawing of the typical-filtered solar channel. Incoming radiation enters the sensor through a protective window. After passing through a spectral filter, it passes through a second window and strikes a 3M black-painted thermopile detector surface. The first protective window minimizes the effects of charged particles, whereas the second window reduces the effects of solar heating of the filter and reradiation to the detector. The whole interior of the cell was anodized to reduce the reflection of solar radiation onto the detector.

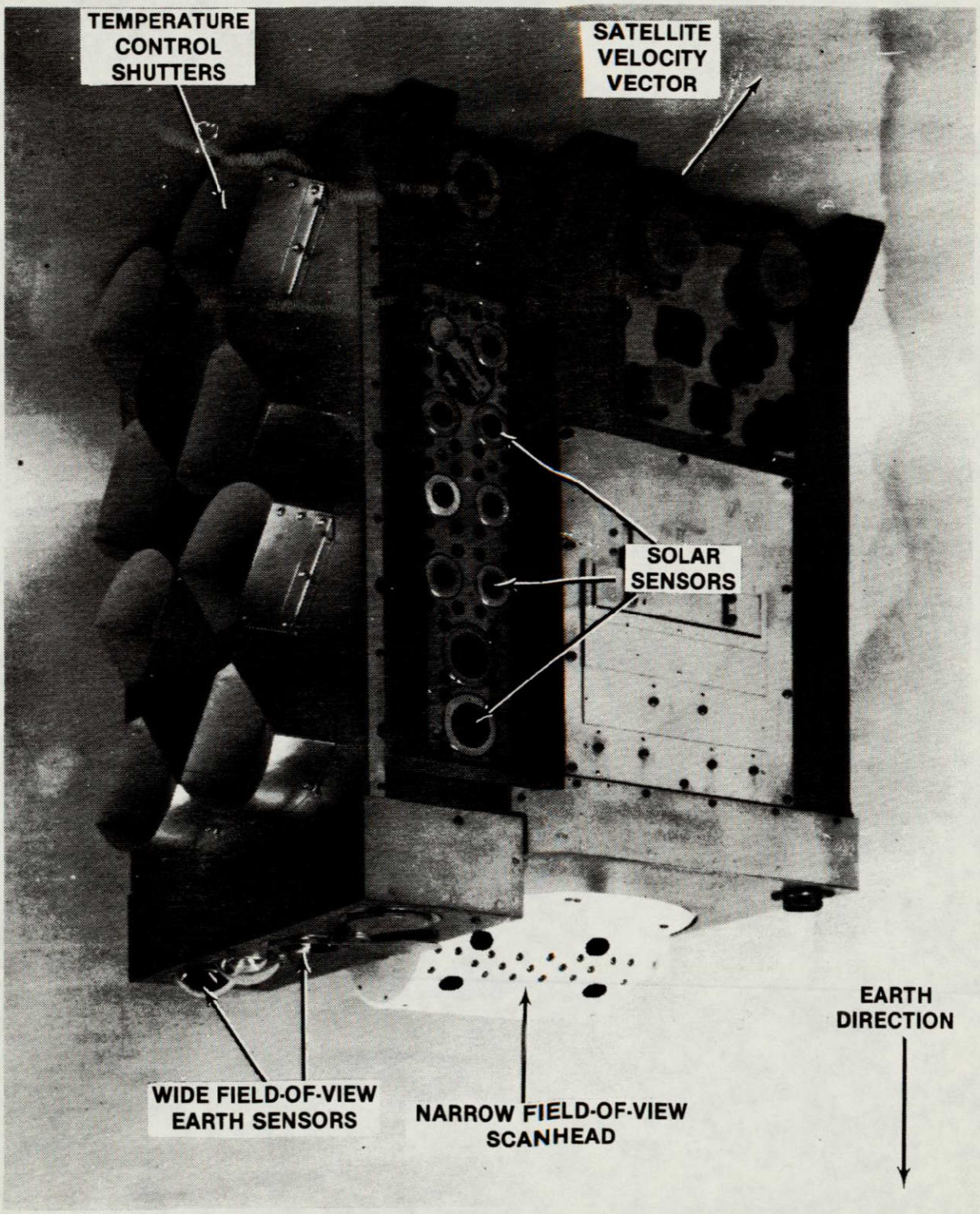

Figure 1 Earth Radiation Budget Sensor System

TABLE 2 Characteristics of ERB Solar Channels

Channel	Wavelength Limits, μm	Filter	Noise Equivalent Irradiance, W m^{-2}
1	0.2–3.8	Suprasil W	1.77×10^{-2}
2	0.2 3.8	Suprasil W	1.77×10^{-2}
3	(0 2 to) 50	None	1.43×10^{-2}
4	0.536–2.8	OG530	1.94×10^{-2}
5	0.698–2.8	RG695	1.91×10^{-2}
6	0.395–0.508	Interference Filter	3.58×10^{-2}
7	0.344–0.460	Interference Filter	5.73×10^{-2}
8	0.300–0.410	Interference Filter	7.55×10^{-2}
9	0.275–0.360	Interference Filter	0.94×10^{-2}
10C†	(0 2 to) 50	None	2.39×10^{-2}

The unencumbered FOV for all channels is 10 ; the maximum field is 26 for channels 1 through 8 and 10C. The maximum FOV for channel 9 is 28 . All are types of Eppley wire-wound thermopiles. Values obtained from adjusted NIMBUS 6 results

TABLE 3 Characteristics of ERB Fixed Wide-Angle FOV Channels

Channel	Wavelength Limits, μm	Filter	Irradiance Range Anticipated, W m^{-2}	Noise Equivalent Irradiance, W m^{-2}
11	<0 2 to >50	None	−200 to +600	6.55×10^{-3}
12*	<0.2 to >50	None	−200 to +600	6.55×10^{-3}
13	0.2 to 3.8	Two Suprasil W hemispheres	0 to 450	6.55×10^{-3}
14	0.695 to 2.8	RG695 between two Suprasil W hemispheres	0 to 250	6.65×10^{-3}

All channels have type N3 thermopile sensors. All channels have an unencumbered FOV of 121 and a maximum FOV of 133.3 . Channel 12 has an additional FOV selection of 89.4 unencumbered, 112.4 maximum. Output of these channels is a 3.8-s integral of the instantaneous readings

*Channels 11 and 12 are redundant channels. Channel 11 has black-painted baffles and is used for in-flight calibration of channel 12. Channel 12 has polished aluminum baffles as did both channels NIMBUS 6.

TABLE 4 Characteristics of ERB Scanning Channels

Channel	Wavelength Limits, μm	Filter	Noise Equivalent Radiance, W cm^{-2} sr^{-1}	NEP, W $H_z - \frac{1}{2}$	FOV, deg
15 18	0 2–4 8	Suprasil W	3.7×10^{-5}	6.65×10^{-9}	0.25 × 5.12
19–22	4.5–50	Deposited layers on diamond substrate	1.8×10^{-5}	1.73×10^{-9}	0.25 × 5.12

Each of the ten solar channels is an independent, individual modular element with a mated amplifier as part of the unit. The sensors are advanced versions of wirewound-type thermopiles. There are no imaging optics in the solar channels; only filters, windows, and apertures. No optical amplification is required to maintain high signal-to-noise ratios because of the high thermopile sensitivities and state-of-the-art electronics used. Channels 1 and 2 are duplicate, Channel 1 being the reference for Channel 2 for the in-flight calibration program. Channel 1 is normally shuttered.

Channels 4 and 5 contain broad bandpass filters with transmittance spectra matching those of the standard Schott glasses, OG530 and RG695, of the World Meteorological Organization. (The RG695 glass is also used in Channel 14, one of the shortwave fixed earth-flux channels). The interference filters are deposited on Suprasil W (grade III) fused silica substrates to minimize degradation. The transmittance of a 2 mm thick piece of Suprasil W from 0.2 um to 5 um is shown in Figure 3. Blocking outside the primary transmission bands, is acheived by interface layers only. No radiation absorbing glasses are used.

The spectral intervals in the 0.2 μm to 0.526 μm, 0.526 um to 0.695 μm, and 0.20 μm to 0.695 μm is obtained by differential treatment of the channel 4 and 5 data, together with readings obtained from Channel 2. Channels 1 through 8 have type N3 thermopiles; Channel 9 has type K2. Channel 10C has a modified model H-F self calibrating cavity element. The cavity is mounted onto a circular wirewound thermopile. The electric heater used for self calibration is energized when a "GO/NO GO" heater command is issued. The thermopile output and the heater voltage and current are then sub-multiplexed into the Channel 10C data stream.

The solar channel assembly is located on the side of the spacecraft facing in the direction of spacecraft motion. The assembly can be rotated 20 degrees in 1 degree steps to either side of the spacecraft forward direction in order to acquire an on-axis view of the sun under the expected variation of the satellite orbit plane with respect to the sun. As the satellite comes over the Antarctic region the sun is viewed within the unencumbered field for about three minutes. The unencumbered field is that for which the entire sun's image is contained in the receiver FOV. The

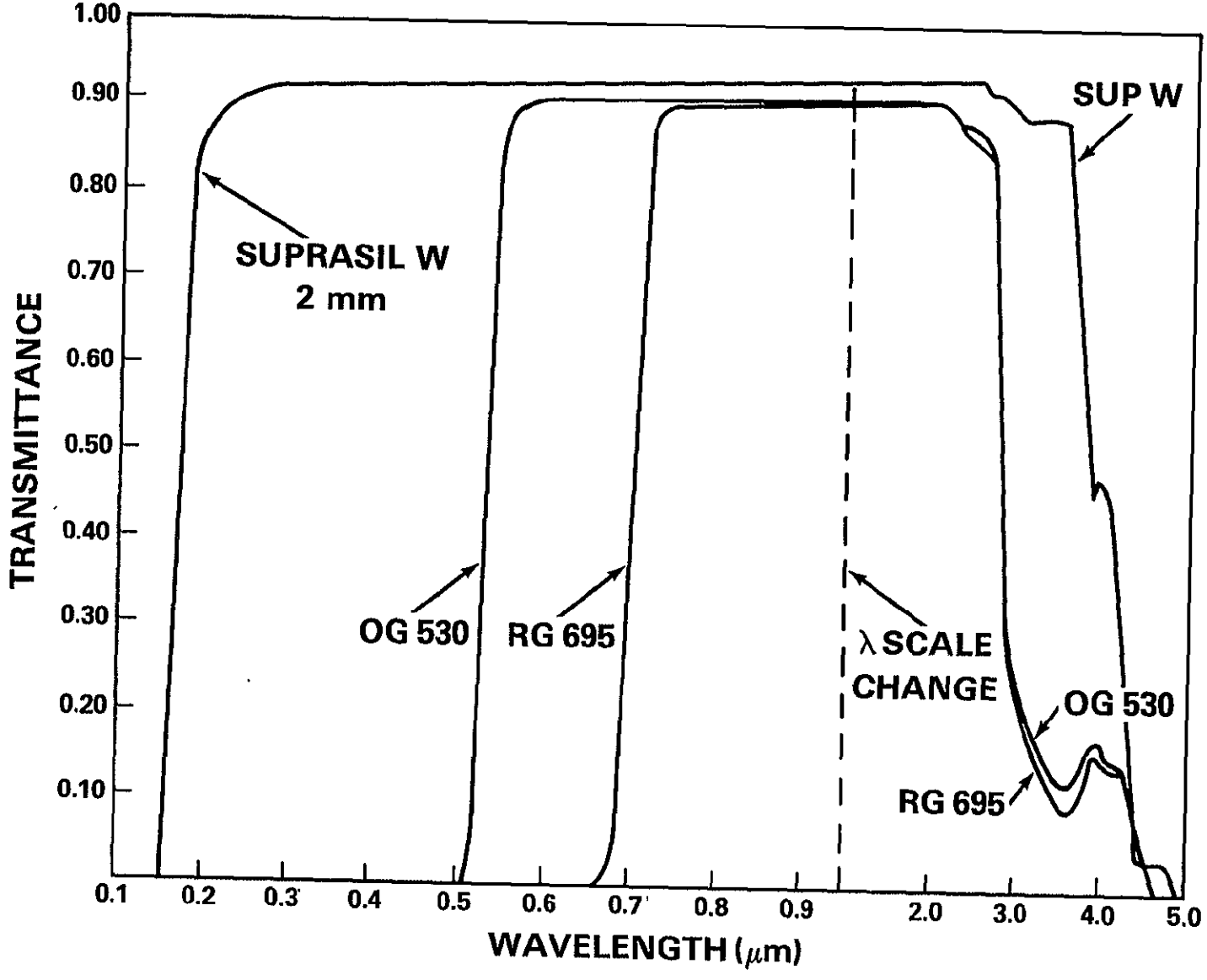

Fig. 3. Transmittance of Suprasil W and Schott colored glasses.

solar channels are monitored before and after solar acquisition in order to obtain the space radiation reference (or "zero-level" response). The outputs of the solar channels are sampled once per second.

3.2 Wide-Angle Field-of-View Channels

Figure 4 shows the typical optical arrangement of channels 13 and 14 earth-observing WFOV channels. The domes on channels 13 and 14 provide the same charged particle and infrared attenuation filtering as is the case for the solar channels. Channels 11 and 12 have no hemisphere-shaped windows and sense the entire spectral range from about 0.2 to 50 um. The FOV of each channel encompasses the entire earth surface visible from the Nimbus orbit. To allow for the possibility of a small angular misalignment of these channels with respect to nadir, the FOV acceptance angle is slightly larger than that required to view the earth disc. In addition, Channel 12 has an insertable stop, so that upon command, it can view slightly less than the entire earth surface.

Channel 11 (normally shuttered) is a duplicate of Channel 12 and is used only occasionally as a calibration check of Channel 12. For Nimbus-7 the Channel 11 baffles have been painted black in order to investigate a so called "space loading" induced signal offset. The earthward-facing surfaces of these channels are highly polished. Each employs a type N3 thermopile with a circular receiver.

Channel 13, the shortwave (0.2um to 3.8 um) fixed earth-flux channel, is equipped with two hemispheres of Suprasil W (grade III) fused silica. The spectral band matches that of solar Channels 1 and 2. The difference in measured radiation between Channel 11 (or 12 with full field) and Channel 13 is the longwave terrestrial component. Channel 13 is similar to a precision pyranometer.

Channel 14 has a broadband (RG695) filter hemisphere, to match the band of Channel 5. The RG695 hemisphere of Channel 14 is between two Suprasil W, fused silica hemispheres. The outer one is thick to attenuate particle radiation which might damage the glass. The inner hemisphere is a characteristic IR blocker included in all precision pyranometers.

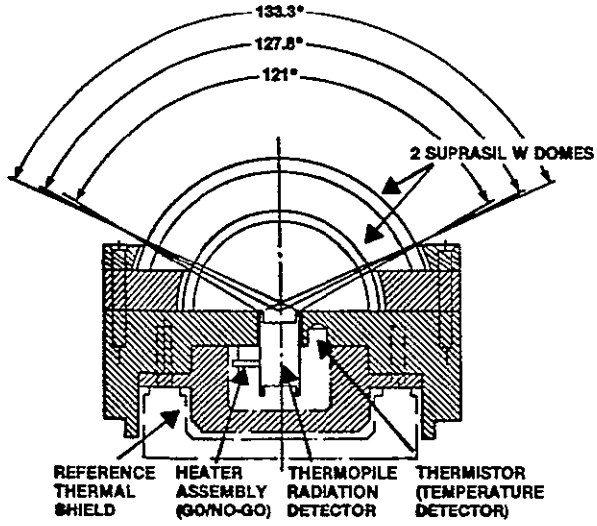

Fig. 4. Typical wide-field-of-view earth-viewing sensor

The measured irradiance values of channel 13 (0.2 to 3.8 μ m) and channel 14 (μ0.7 to 2.8 μm) are determined from the measured counts. The difference between these two channels lies in the 0.2 to 0.7 μm and 2.8 to 3.8 μm spectral range. Portions of both of these spectral regions are highly absorbed by the atmosphere. However, in the 2.8 to 3.8 μm a very small amount of energy compared to that in the visible spectral region, is radiated into space. Thus, the approximate irradiance difference between these two channels can be determined for channel comparison purposes.

3.3 Narrow-Angle Field-of-View Scanning Channels

The ERB has four optical telescopes arranged in a fan shape. Each telescope contains a short wave and long wave optical system. As shown in Figure 5, the optical hardware schematic of the narrow field-of-view (NFOV) scanning channels, the telescope focuses collected radiation alternately on one of two apertures. This is performed using a chopping wheel with mirrored teeth. When the mirrors are in the radiation beam, the radiation is reflected into the infrared optical system. The openings in the mirror teeth pass the radiation to the short-wave relay assembly. As noted in Figure 5, the short-wave relay assembly focuses reflected radiation via M3 through an appropriate filter onto the pyroelectric detector.

The longwave portion of the scanning channels operates in a rather unique fashion. When a reflecting tooth is in the radiation beam the reflected radiation passing through the aperture is focused on the pyroelectric detector by the M5 mirror. It passes through a coated diamond longwave interference filter before striking the detector.

When the openings between the mirror teeth are in the optical path, blackbody radiation produced by a flat surface surrounding the aperture is reflected by M4 and passes back through the aperture slit as shown in Figure 5. This reference radiation then is reflected by M5 passing through the coated diamond filter to the detector. As a result, the pyroelectric (ac) detector senses the difference between the Earth/atmosphere or external blackbody radiation and the internal reference blackbody radiation.

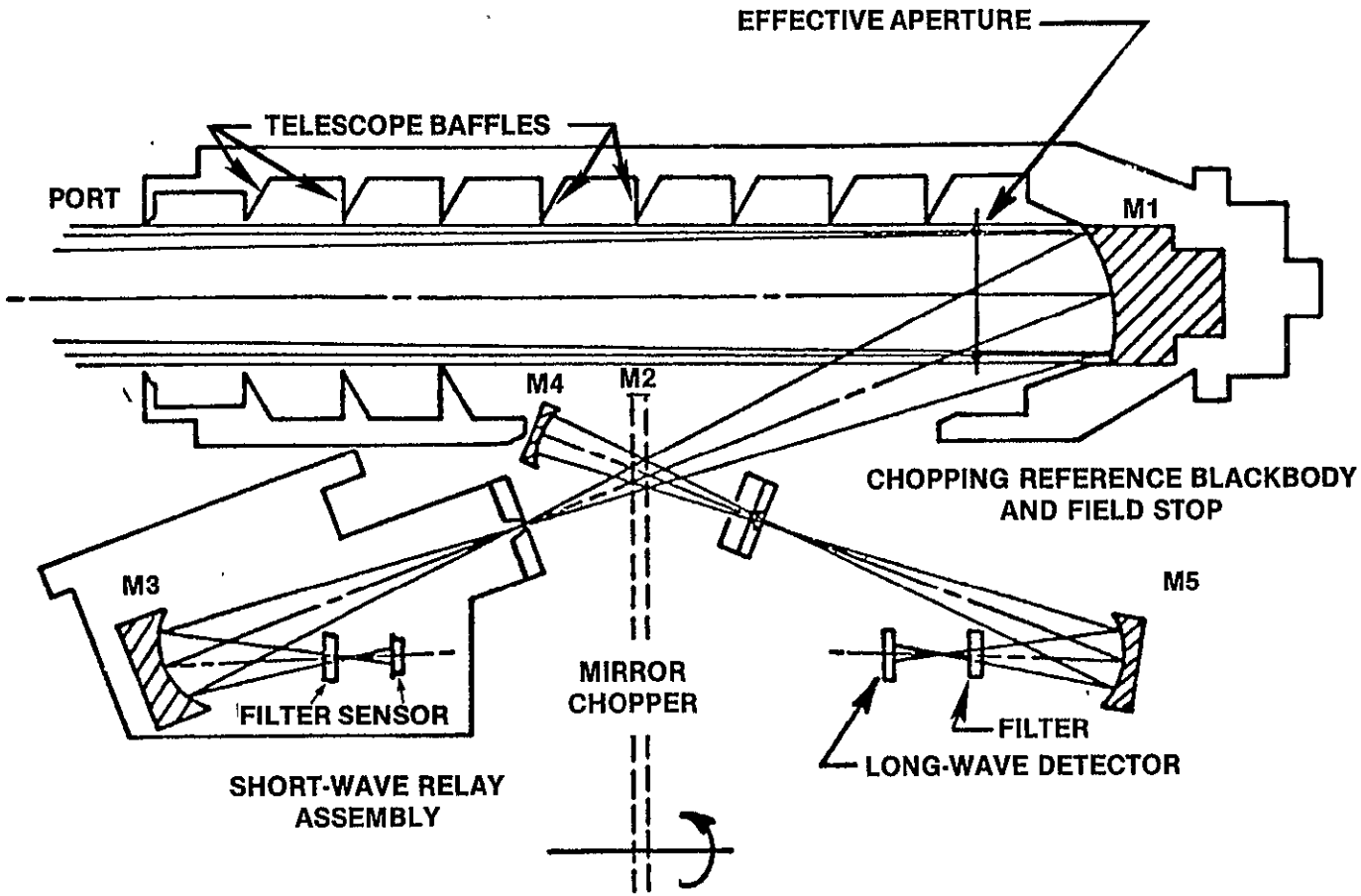

Fig. 5. ERB scanning channel optical schematic.

The scan head is on a gimbal mounted on the main frame of the radiometer unit. The gimbal arrangement allows the pointing direction of the scan head to be varied within a vertical plane by rotation of the scan head, and within a horizontal plane by rotation of the gimbal. The vertical motion is accomplished with a stepper drive which rotates the scan head in steps of 0.25 degrees. The horizontal gimbal rotation is driven by a stepper motor which rotates the gimbal in steps of 0.5 degrees.

The FOV's of the four telescopes are rectangular, (0.25 degrees x 5.12 degrees), and are arranged so that at the horizon the upper corners of the FOV's lie along the earth's horizon as shown in Figure 6. The narrow-angle (0.25 degrees) side of the FOV is in the direction of vertical motion. The FOV's of the short wavelength channels (15 through 18) are coincident, respectively, with those of the long wavelength channels (19 through 22).

The scanning channel data is recorded at 0.5 second intervals. Thus to produce the various integrated 0.25^{o} x 5.12^{o} aperture fields-of-view shown in Figure 6, the scan head is made to rotate at different stepping rates. For instance, for the approximate five by five degree field-of-view, the scanner is stepped twenty times in 0.5 seconds. The resultant integrated signal is recorded. In a simular manner the 2.5^{o} x 5.12^{o} FOV's are produced by stepping the scanner ten times during 0.5 seconds and recording the resultant integrated signal.

To observe the radiance from various scenes over a wide variety of incident and emerging angles, there are five different scan modes. These routines are schematically illustrated in Figure 7. Four scan patterns are a composite of long and short grids shown in Figure 6 (a long grid in the forward direction is followed by a short grid in the cross-track direction and then concluded with a long grid in the aft direction). The fifth scan pattern is a composite of scan pattern 3 followed immediately by scan pattern 4. Scan modes 1, 2, 3, and 4 obtain a maximum number of angular independent views of a given geographical area. When the instrument is in one of these four modes of operation, that scan pattern is repeated every 112 seconds or every 700 km along the subpoint track. These four scan modes ensure the ability to obtain numerous observations in the principal plane of the sun, the plane in which the greatest angular variations in reflected sunlight

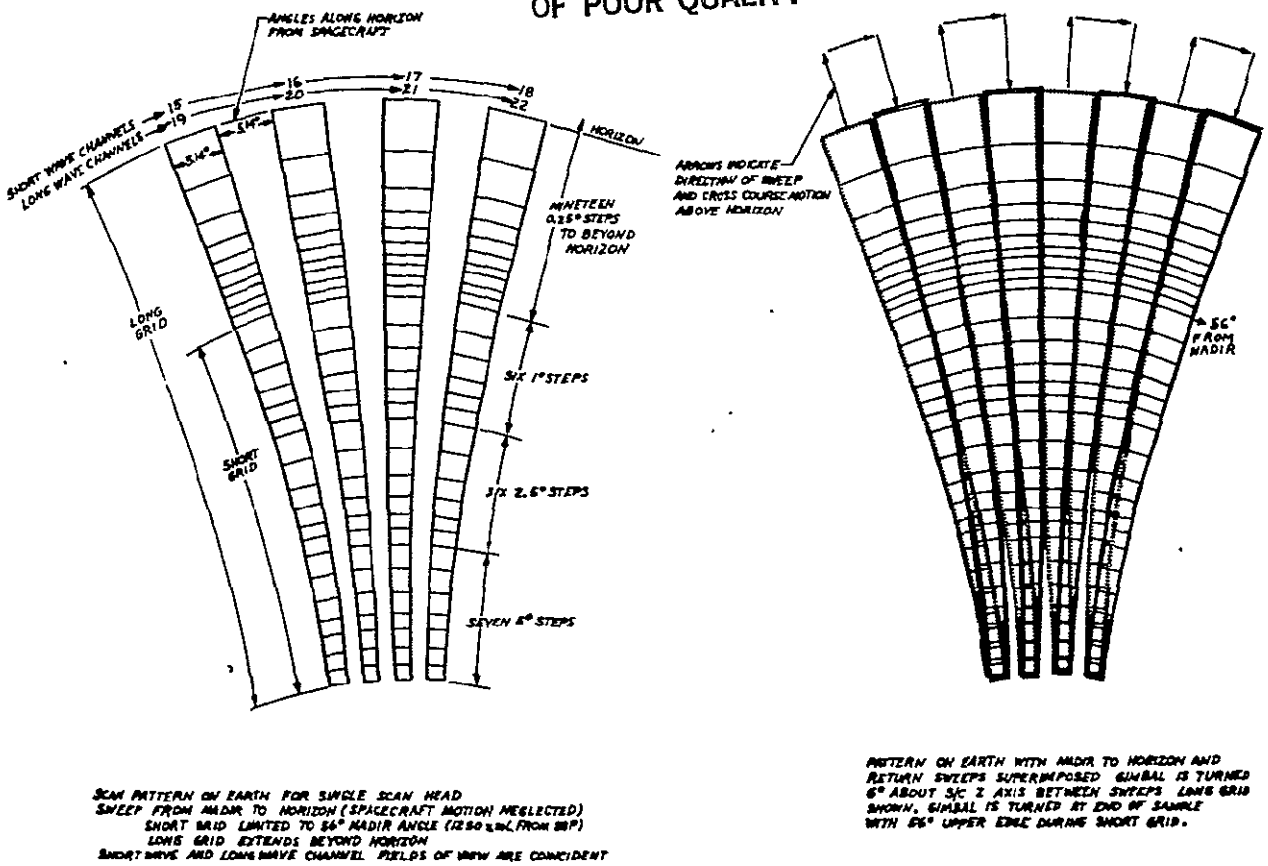

Fig. 6. ERB scan grid earth patterns.

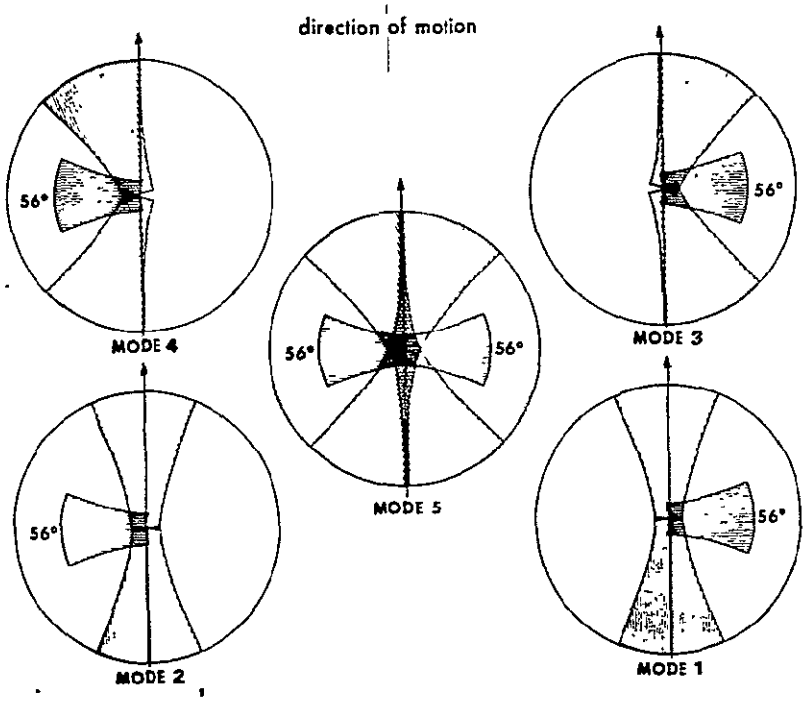

Fig. 7. ERB scan modes.

occur. Scan mode 5, which is the normal mode of operation yielding maximum earth coverage, is repeated every 224 seconds or every 1400 km along the subpoint track.

Figure 8 shows a complete scan pattern projected on an imaginary sphere coincident with the earth's surface and fixed with respect to the satellite. The solid line with the arrowheads indicates the motion of a point on the earth's surface relative to the imaginary sphere and scan pattern. The small target areas considered for illustration are located at 40°N latitude in Figure 8. The shaded portions of the scan pattern indicate which FOV's contain the target area. The area is first observed near the forward horizon (in the direction of satellite motion) at a view angle of 58.5 degrees. During succeeding scan patterns, as the satellite approaches the area, the area is viewed at angles of approximately 56, 51, 49, 15, and 0 degrees. As the satellite moves away from the area, radiance observations are made over the other half of the scanning plane at view angles of 15, 40, 51, 47, and 58.5 degrees. Consequently, a fairly complete picture of the angular distribution of radiation emerging from this geographical area in the scanning plane is obtained.

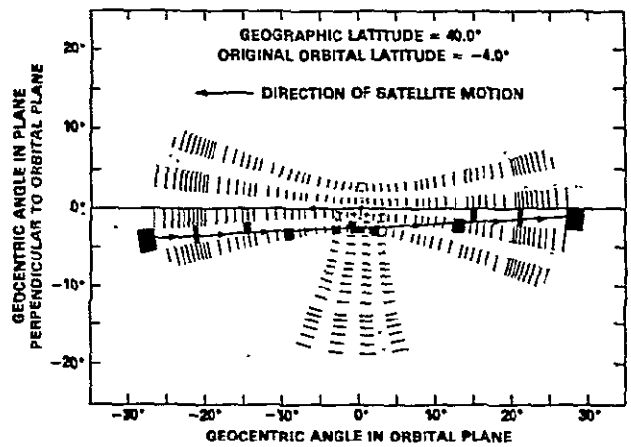

Fig. 8. Scanning channel views of a geographical area near the subpoint tracks.

4. PRE-LAUNCH CALIBRATION

ERB radiometric accuracy requirements made traceability to NBS standards desirable. However, time and equipment limitations made this approach difficult to achieve in a rigorous manner. Thus it was necessary to calibrate each set of sensors (i.e., solar, WFOV earth and scanning) in a somewhat different unique manner. Cross checking both the prelaunch and flight data resulted in a number of compromise coefficients which can not be directly related to NBS or other standards.

Preflight calibration of the solar channels consisted of a number of intercomparisons and transfer operations. The reference for the absolute calibrations was the new World Radiometric Reference (WRR) scale which is embodied in a number of self-calibrating cavity radiometers. Channel 10C of the Nimbus 7 ERB is itself such a device. This new scale can be referenced to previous scales such as the International Pyrheliometric Scale (IPS 1956). The four major solar channels (1,2,3 and 10c) have been directly intercompared with self calibrating cavity instruments.

For transfer operations a solar simulator was used as a source and a normal incidence pyrheliometer (NIP) was employed. Both of these are also traceable to the WRR. When calibrating the filtered channels (4,5,6,7,8 and 9) the NIP was fitted with a filter wheel containing filters matching the flight set. The incident irradiance is calculated using the measured irradiance and the appropriate filter factor for the particular filter.

The ERB reference sensor model (RSM), which is a duplicate of the flight instruments relative to the solar channels, has been employed as a transfer and checking device throughout the Nimbus 6 and Nimbus 7 calibration programs, (Hickey and Karoli, 1974). All vacuum calibrations of the Nimbus 6 and 7 ERB solar channels could be referenced through the RSM as well are many of the calibrations performed at atmospheric pressure.

The solar channels were not calibrated during thermal vacuum testing of the spacecraft. Their calibrations were checked during an ambient test after the thermal vacuum testing. Final calibration values for the solar channels were expressed in units of Counts/Watt/meter^2 (C/Wm^2) relating the on-sun signal output to the incident extraterrestrial solar irradiance in the pertinent spectral band of the channel.

There were longwave and shortwave calibrations of Channels 11 and 12. The longwave calibrations were performed during thermal vacuum testing with a special blackbody source named the total earth-flux channel blackbody (TECB). The source was a double cavity blackbody unit designed for calibrating Channels 11 and 12 after they were mounted on the ERB radiometer unit. It operated over a temperature range of 180K to 390K with an apparent emissivity under test conditions in vacuum of 0.995 or greater. Temperatures were measured and controlled to an accuracy of 0.1^{o}C during these calibrations. These calibrations were performed during both instrument and spacecraft testing. The entire FOV of the channels was filled by the TECB including the annular ring which normally views space in the angular element between the unencumbered and maximum FOV's. Channel 12 was also calibrated for the shortwave response by employing a solar simulator whose radiation was directed normal to the detector in vacuum. The reference NIP was employed as the transfer standard during this calibration.

Channels 13 and 14 were calibrated within their respective spectral bands only. These tests were performed in the same manner as the shortwave calibration of Channel 12. For Channel 14 the reference NIP was fitted with a matching RG695 filter (as for Channel 5) to yield the proper spectral band.

An angular response scan was performed on each wide FOV channel in order to relate the normal incidence calibrations described above to the overall angular response of the channels.

The shortwave scan channels were calibrated by viewing a diffuse target. Three methods were employed. These were: viewing a smoked magnesium oxide (or barium sulphate) plate which was irradiated by the solar simulator, exposure in a diffuse hemisphere illuminated internally by tungsten lamps, and viewing the inside

of a diffusing sphere. For methods 1 and 3 the reference instrument was a high sensitivity NIP calibrated in terms of radiance. The second method employed a pyranometer as reference instrument. The sensitivity values selected for use are an average of methods 1 and 3. Unfortunately these tests could only be performed at atmospheric pressure. The reason vacuum testing is desirable is because it has been found that atmospheric effects produce calibration values which are not the same as those measured in vacuum and vacuum operating corrections are required.

Another calibration of these channels was the in-flight check target. With the channels in the shortwave check position (viewing the scan target) the instrument was irradiated by the solar simulator beam. This test was performed at normal incidence when the instrument was in vacuum. The reference was one of the reference NIP's. In air, the instrument was similarly calibrated at a number of angles both in elevation and azimuth to obtain the angular characteristics necessary for the reduction of in-flight shortwave check operations.

The longwave scan channels were calibrated in vacuum at both the instrument and spacecraft level thermal vacuum tests. The sensors viewed a special blackbody source called the longwave scanning channel blackbody (LWSCB) which had a separate cavity source for each channel. A conventional procedure was used which covered the complete range of in-flight measurement possibilities.

5. IN-FLIGHT CALIBRATIONS AND RADIOMETRIC PERFORMANCE

In-flight calibration for the solar channels does not exist except for channel 10C whose cavity is heated by a precision resistance heater. Accurate monitoring of the voltage and current of the heater as well as the detector response yields the calibration sensitivity. This led to very precise determinations of the total solar irradiance (Hickey, et al., 1981). All thermopile channels (1-14) are equipped with the same heaters which are used during prelaunch activities to check whether the channels are functioning properly. The heaters are used as a rough check in the analysis of operational data. These channels are also equipped with an electrical calibration which inserts a precision voltage staircase at the input to the entire signal conditioning stream. While the electronic calibration cannot be used to infer changes in the sensor or optics characteristics, it insured prevention of misinterpretation of electronic measurements. Analysis of the electronic calibration data has yielded no abnormalities. Channels 1 through 3 can be directly compared with channel 10C to assess their in-flight calibration. In addition, the degradation of channel 2 is checked by the occasional exposure of its duplicate channel 1 which is normally shuttered.

The degradation with time of the solar channels 1 through 9 is depicted in Figure 9 for the first 8 months of flight. Particular attention should be given to channels 6 through 9 which contain the interference filters. Their curves show that a high rate of degradation occurred during the first two months followed by a short period of relative stability. After this the channels reversed the earlier trend and began to recover. After a little over four months in orbit three of the channels completely recovered while the remaining one (channel 7) almost recovered.

Shortly thereafter channels 7 and 8 began to degrade again with rates that were much slower than those encountered initially. A discussion of the possible cause of the degradation and the mechanism for the recovery can be found in the paper by Predmore, et al., (1982). In spite of these degradations and recoveries Hickey, et al., (1982) showed that solar variability in the near ultraviolet could still be derived from the data.

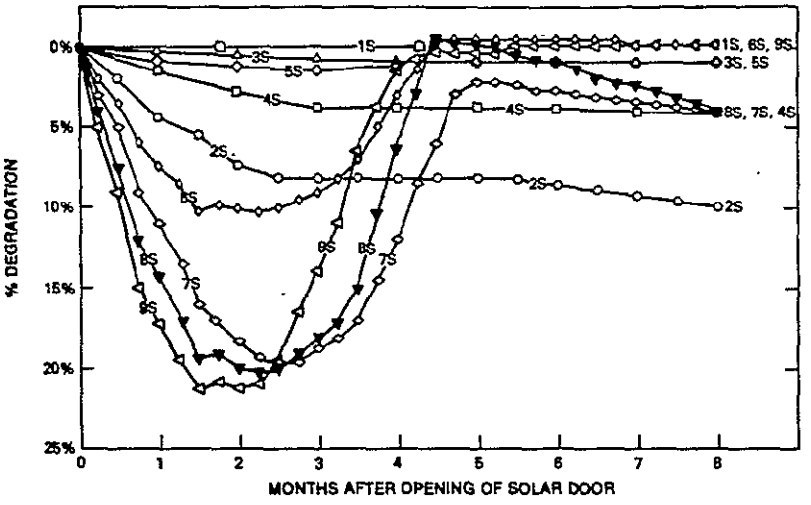

Fig 9 Percent degradation of the solar channels during the first eight months after launch.

Channel 12 calibration relies on the stability of the normally shuttered matching channel 11. Also, when both channels 1 and 11 are shuttered the effective blackbody temperature of each shutter measured radiometrically may be compared with their monitored temperatures. Channels 13 and 14 have no inherent in-flight calibration capability. They rely on occasional looks at the sun near spacecraft sunrise or sunset when the satellite is pitched to permit solar radiation to be incident on the channels.

Periodic in-flight checks of the shortwave scanning channels' (15-18) calibration were accomplished by viewing the solar-illuminated, diffusely reflecting plate described earlier. When the scan-head was commanded to turn to the "shortwave check" position, a door opened exposing the laboratory-calibrated flat plate to sunlight which it reflected into the shortwave channels. Analysis of this data indicated a slow steady degradation of the plate surface even though the plate was securely stored behind a door between measurements. The longwave scan channels (19-22) were calibrated periodically by pointing the radiometers at space and then at an internal blackbody whose temperature was accurately monitored. They share the only true in-flight calibration capability with channel 10C. Additional checks have been made by comparing the fluxes observed by the WFOV channels with those deduced from the NFOV channels.

The principal check on the calibration was made by intercomparing the observed wide-angle fluxes with those deduced from the narrow-angle radiances. In particular, the longwave scanning channels were used throughout because of the high confidence placed upon their measurements. As will be discussed in more detail later, the calibration of these channels (19-22) has remained stable to better than 1% throughout the lifetime of the scanners ($\approx$ 20 months) as checked by an onboard calibration blackbody and cold space. Channels 11 and 12 were compared with these channels by restricting the comparison to be performed only on the night side of the earth and for an approximate two week period.

Scanning channel radiances covering a complete scan cycle (112 seconds) were utilized to yield an estimate of the WFOV irradiance. These were compared with the actual WFOV irradiances averaged over the same time period. Under the assumption that the irradiances derived from the scanning channels were absolutely correct, regression analyses yielded corrected values of the WFOV gain sensitivities. Table 5 compares these new values with the prelaunch sensitivities.

TABLE 5. In-Flight Calibration Checks of NIMBUS 7 ERB Shortwave NFOV Channels

Channel	Prelaunch Value	From Diffuse Target	From Snow Target	From W/N Comparison
15	3.617	3.917	3.957	3.914
16	4.236	4.723	4.791	4.761
17	4.550	4.841	4.891	4.873
18	3.616	4.133	4.256	4.249

Sensitivity ($c/W\ m^{-2}\ Sr^{-1}$).

TABLE 6. INFLIGHT CALIBRATION CHECKS OF NIMBUS-7 ERB WFOV CHANNELS

Sensitivity (Cts/Wm^{-2}) at 25°C

Ch. No.	Wavelength Band (μm)	Prelaunch Value	From W/N Intercomp.
11	0.2 - 50	1.49166	1.492
12	0.2 - 50	1.72326	1.596
13	0.2 - 3.8	1.939	1.870
14	0.2 - 2.8	4.179	4.030

An estimate of the shortwave fluxes during the daytime could be made by subtracting the observed longwave fluxes based upon the scanning channels from the total fluxes (shortwave plus longwave) obtained from adjusted channel 12 values (i.e. using the calibration sensitivities derived on the night side of the earth). These shortwave estimates were compared with the shortwave fluxes deduced from the shortwave scanning channels (discussed later) as well as that measured by channel 13, again for an approximate two week period. The calibration sensitivity obtained is shown in Table 6. Since a direct intercomparison could not be obtained for channel 14, an adjusted sensitivity value was given on the basis that any proportional errors in the prelaunch sensitivity of channel 14 be the same as that for channel 13. The principal physical difference between the channels is the presence of an additional red dome filter in channel 14 between the same two suprasil-W domes which are also present in channel 13.

Since the sensitivity for channel 11 derived from the wide/narrow (W/N) intercomparison was nearly identical to the prelaunch value, the prelaunch value was accepted. Before deciding upon the value for channel 12, we considered one additional calibration that had been performed for channel 12. Employing a solar simulator whose direct beam illuminated the channel, a gain of 1.607 counts/watt m^{-2} was obtained, which differed only 0.7% from the value obtained in the W/N intercomparison. For this reason the solar simulator calibration was accepted.

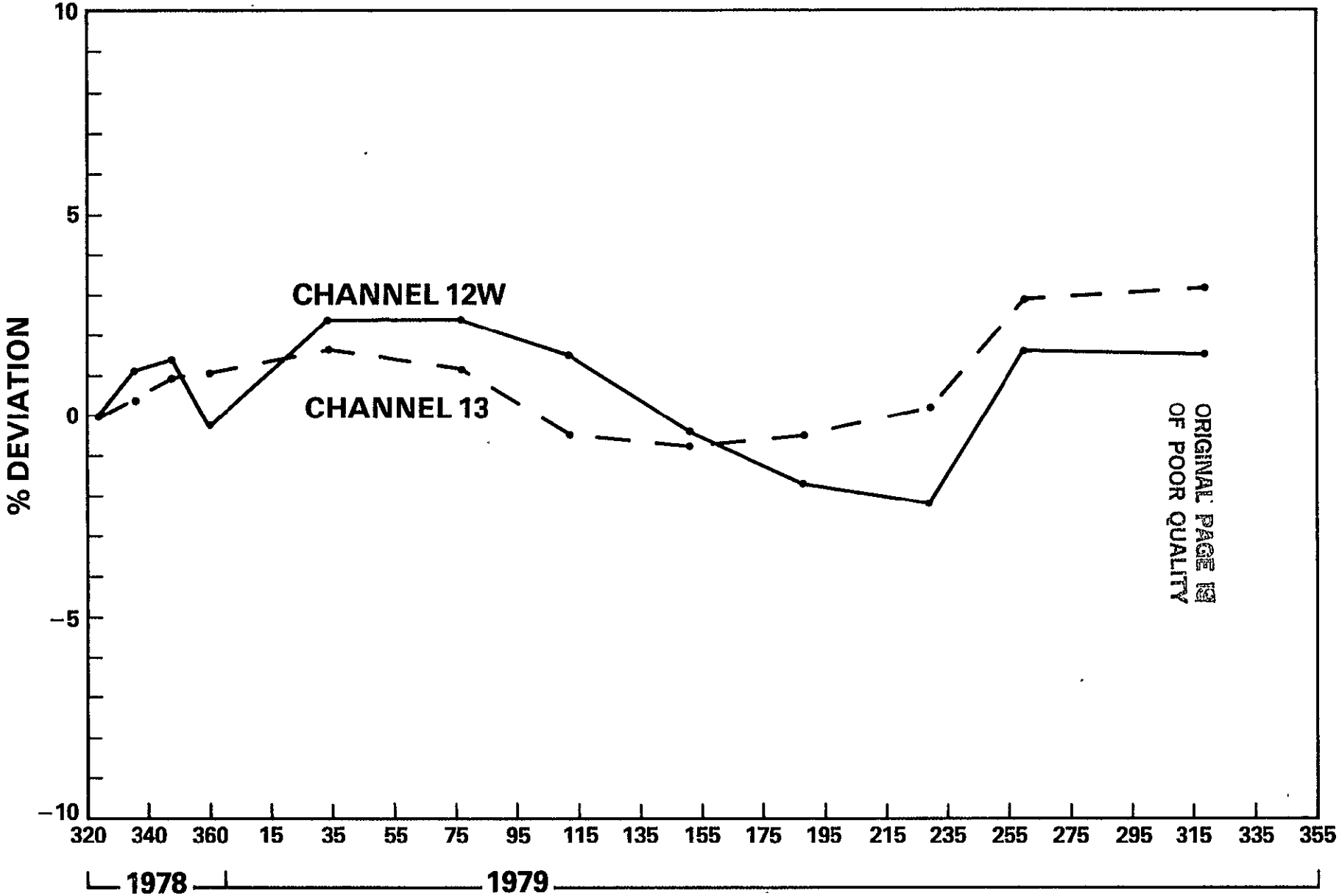

Fig. 10. WFOV/NFOV comparison results for NIMBUS 7 ERB WFOV channels.

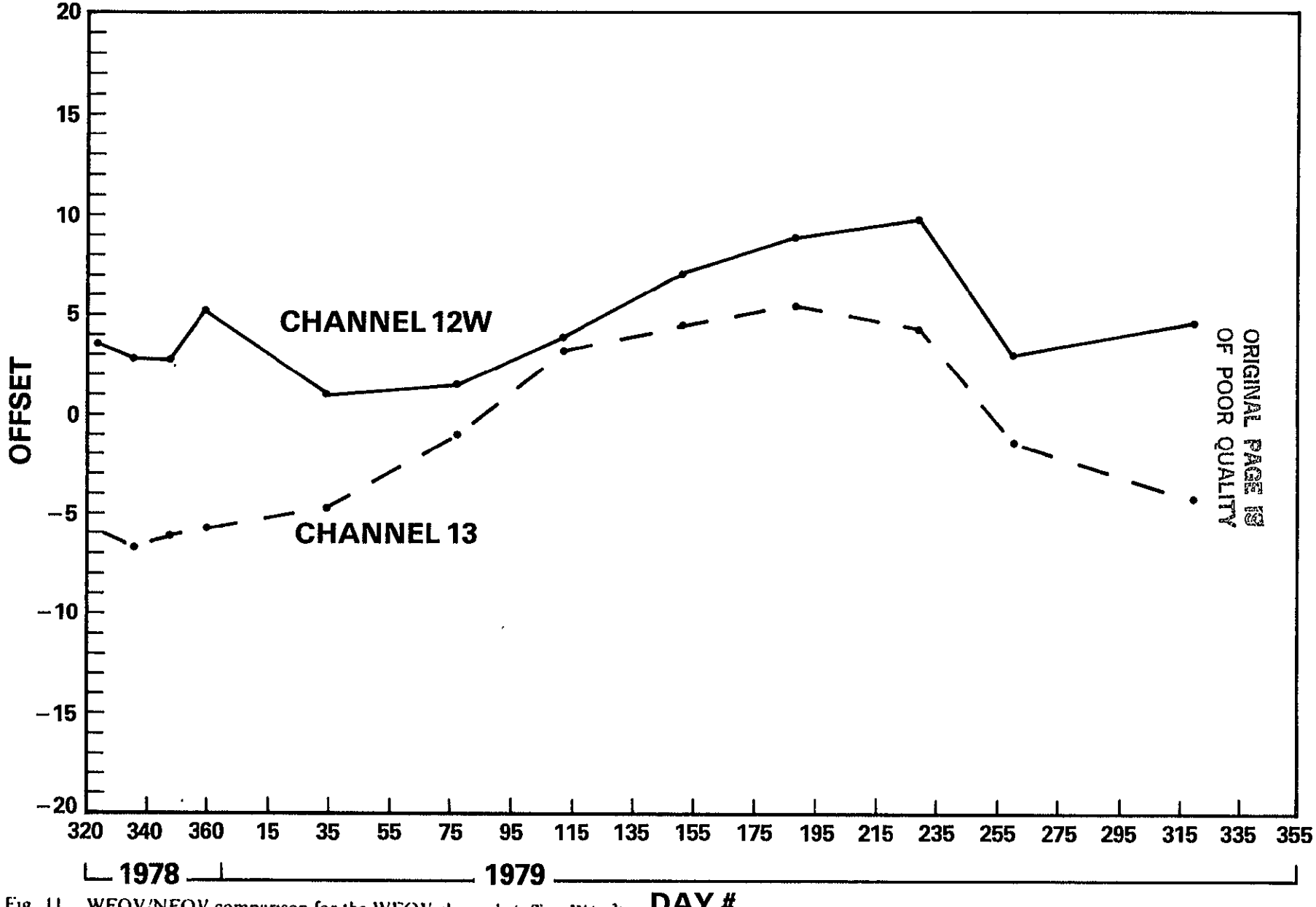

Fig. 11. WFOV/NFOV comparison for the WFOV channels (offset-W/m^2).

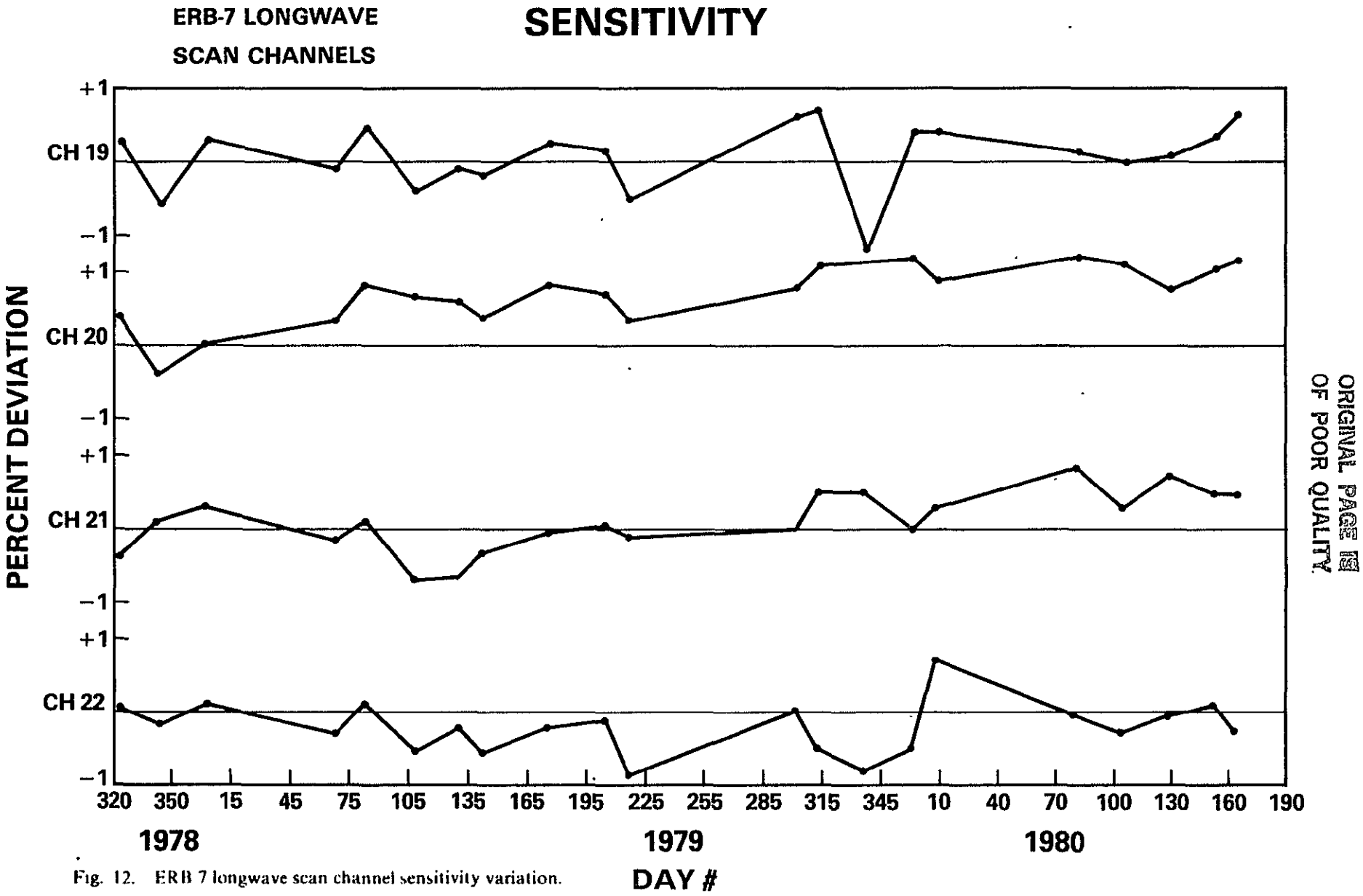

Fig. 12. ERB 7 longwave scan channel sensitivity variation.

In order to assess the stability of the channels with time, the regression analyses of the data from the W/N intercomparisons were performed for selected intervals throughout the first year in orbit. Figure 10 shows the percent deviation of the sensitivities from their initial values for channels 12W (W refers to wide as opposed to narrow when the field-of-view limiter was in place) and 13 as a function of the day of the year. Positive deviations are degradations. Channel 12W remained stable to within $\pm$2% while channel 13 appeared to have suffered a net degradation of a little over 3% by the end of the year. Figure 11 is a plot of the regression offsets (W/m^2) for the same time period. Channel 12W varied over the range of 1 to 10W/m^2 returning after 1 year to within 1 W/m^2 of the initial value. The offset for channel 13 varied from -7 to +6 W/m^2 returning at the end of the year to within 2 W/m^2 of its initial value. Channel 14 could only be properly analyzed by comparing data periods exactly one year apart.

As a result, calibration adjustments were applied to the channel 13 irradiances which not only attempted to correct for the channel sensitivity but it also was to correct for the degradation of the filter dome with time.

As analysis of year to year changes in the irradiances for channel 14 indicate that little or no degradation occurred. Therefore, a constant calibration adjustment was applied to correct only for the sensitivity.

The sensitivity (count/$Wm^{-2}Sr^{-1}$) and offset ($Wm^{-2}Sr^{-1}$) for the longwave scanning channels (19-22) were periodically checked during the nineteen months they operated by performing 2-point calibrations. This consisted of observations of an onboard calibration blackbody and cold space, both of which the scan head was commanded to view. It is important to note that the signal produced by these sensors represents the difference between the target and an internal blackbody reference. Shown in Figure 12 is the percent sensitivity deviation of each channel from their initial values plotted versus the day number of the year. The fact that the variations remain within $\pm$1% of their initial values is evidence of the inherent stability of this unique calibration system. The corresponding offset shown in Figure 13 remained within $\pm$1 Wm^{-2} Sr^{-1} of their initial values, which again indicates stability. This is the prime reason that they are used in the W/N intercomparison analysis.

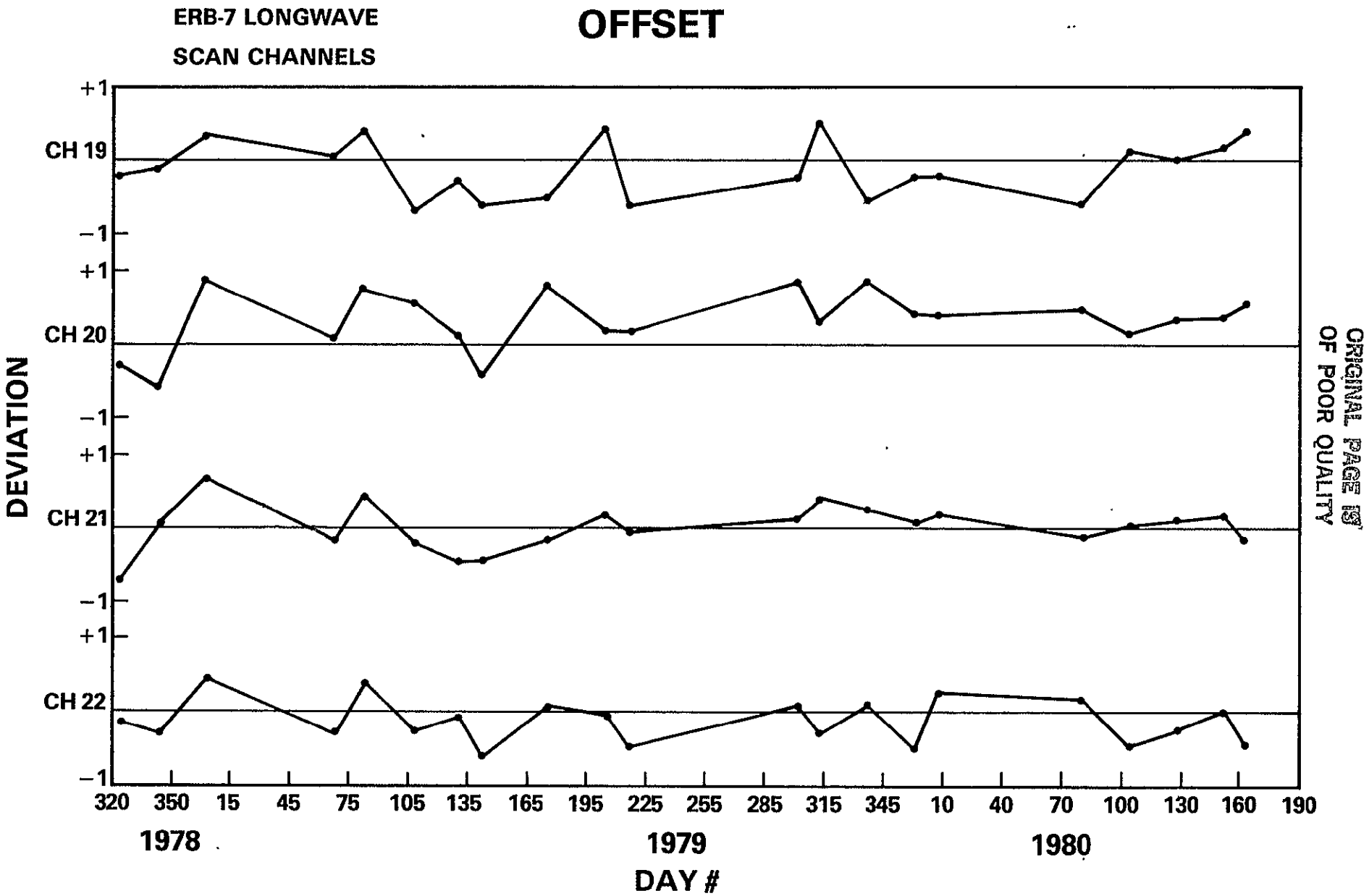

Fig. 13. Long wavelength scan channels offset deviations

The noise levels associated with these channels were obtained by computing the standard deviations of the observed signals when viewing space, the shortwave check target (SWCK), and the longwave blackbody target (LWCK). Normal distributions with standard deviations of 1 to 2 Wm^{-2} Sr^{-1} resulted from these static views. This data indicated that these channels had low noise levels.

The shortwave scan channels (15-18) were analyzed a number of different ways. First, the mean computed shortwave flux, obtained from channel 12 and the longwave scan channels for about a two week period was compared with the mean flux for the same period deduced from each scanning channel. Using the predicted flux as the absolute truth, as before, the scanning fluxes were assessed as being too high by 7 to 17.5% (Vemury et. al., this issue). This meant that the sensitivities should be adjusted up by this amount. Table 7 shows the adjusted sensitivity from the W/N intercomparison along with the prelaunch values.

TABLE 7. INFLIGHT CALIBRATION CHECKS OF NIMBUS 7 ERB SHORTWAVE NFOV CHANNELS

Sensitivity ($Cts/Wm^{-2}Sr^{-1}$)

Ch. No.	Prelaunch Value	From Diffuse Target	From Snow Target	From W/N Intercomp.
15	3.617	3.917	3.957	3.914
16	4.236	4.723	4.791	4.761
17	4.550	4.841	4.891	4.873
18	3.616	4.133	4.256	4.249

Another way that the calibration was checked was by commanding the telescopes to view the onboard diffuse target that was illuminated by the sun at the time of the satellite crossing of the southern terminator. During the prelaunch phase, a solar simulator was the source of illumination. The signal level of each channel in counts was divided by the solar signal in counts as measured by channel 2, corrected for channel degradation. This ratio of counts was further corrected to that for normally incident radiation. Comparison of the ratio determined in orbit with that before launch showed again that the channels in orbit appear to read higher by nearly the same percentages as that discussed above. Correction of the sensitivities based upon this test yielded the values also shown in Table 6.

An additional check was made by observing scenes consisting almost entirely of cloud free snow or ice surfaces and comparing them with published ground-based observations of such surfaces. By eliminating observations whose solar zenith angles were greater than 70^{o} and whose satellite zenith angles were greater than 45^{o}; the comparison reduced to noting the brightness levels of nearly isotropic surfaces. Again, similar results shown in Table 6 were noted. All of these results point to an apparent increase in sensitivity after launch. The variation in the ratio of the observed to the predicted flux using the prelaunch calibration values are shown in Figure 14 as a function of the day number of the year. Also, the results of the observations from the check target are plotted. Channels 15-17 exhibit great stability in the W/N intercomparison results while the check target results show that the ratios decrease as time increases. This indicates that the check target was degrading. Proof of this resulted from a comparison of the snow surface observations discussed above with similar observations one year later. Practically no difference occurred from one year to the next for channels 15-17. Computations of the standard deviation of observations of the shortwave target and blackbody again indicate the low noise level of the channels 15-17. The noise level of channel 18 increased dramatically by the end of 1978.

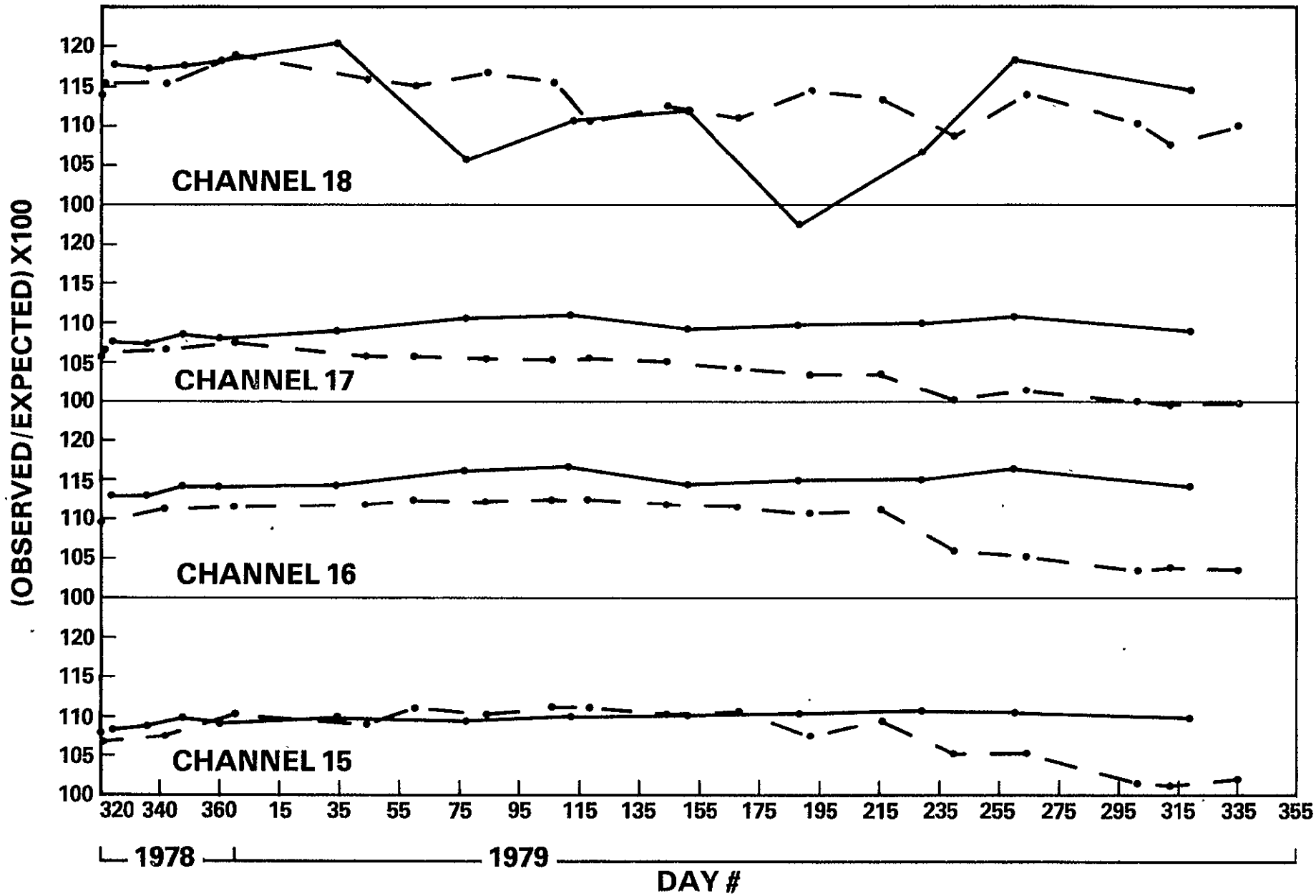

Fig. 14. WFOV/NFOV comparison for shortwave scan channels (calibration check target results—dashed line)

6. DATA PROCESSING AND PRODUCTS

The basic equations needed to convert from raw ERB data counts to radiometric values are given in Appendix A. Details regarding these equation and the coefficients used will be found in the calibration history, Soule, (1983b). The manner in which these radiometric measurements were converted into fluxes and albedoes is given in Appendix B.

The ERB processing system is shown schematically in Figure 15. Raw ERB telemetry data and satellite ephemeris which are stored on magnetic tape were input to a program which generated Master Archive Tapes (MAT). These tapes contain calibrated radiances and irradiances and raw digital data values for all channels plus values of all monitored temperatures, satellite ephemeris and attitude data. As Figure 15 shows, the MAT is the prime source for the generation of all of the products.

The Subtarget Radiance Tapes (STRT) are generated from narrow - angle scanning channel radiances and associated viewing angles which are sorted into one of 18,630 regions (subtarget areas) covering the earth. In each of these areas a classification of the predominant surface type was made. The classification was based upon a number of non-ERB data sources one of which is the Temperature Humidity Infrared Radiometer (THIR) also on the Nimbus-7 spacecraft. The amount of high, middle and low cloudiness present in the subtarget areas is determined by analysis of the equivalent blackbody temperature derived from THIR observations made in the 11 μm window region of the spectrum. The Air Force's 3-D nephanalysis program was the source utilized for estimating the fraction of land, water, snow or ice present in a subtarget area within 24 hours of the ERB observations. Climatological data describing the surface configurations (plains, mountains, deserts, etc.) and dominant vegetation (grassland, savanna, etc.) are included.

The data set contained on the STRT were then used to generate models of the angular distribution of the reflected solar and emitted terrestrial radiation for use in processing the narrow-angle data (Taylor and Stowe, 1984). Angular reflectance models were derived for four surface types (land, water, snow or ice and clouds) for ten ranges of solar zenith angle while only two models of the emitted radiation

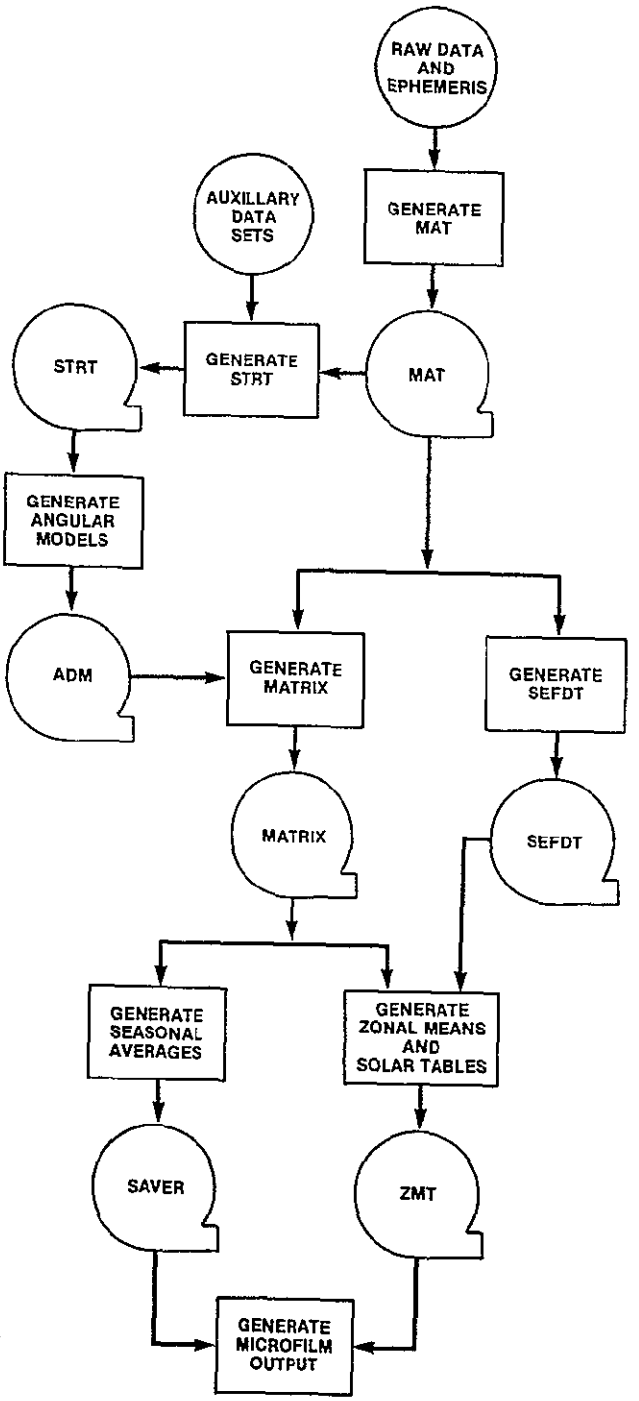

Fig 15 NIMBUS 7 ERB Processing system.

were derived (one for latitudes greater than 70° while the other was for latitudes less than 70°).

The narrow-angle data with the aid of the angular dependence models (ADM) along with the solar and wide-angle data on the MAT were further processed by the program that generates the so called MATRIX tape to yield daily, six day and monthly averaged values of various radiation budget products (see Table 8). The basic algorithms used in the MATRIX production program are reviewed in Appendix B. The products were stored on the MATRIX tape on an approximately equal area world grid (500 km by 500 km) as well as on mercator and polar stereographic map grids. The data on the mercator and polar grids are utilized in the generation of analyzed contour maps which were recorded on microfilm. An analysis of the data on the MATRIX tapes is given in the paper by Jacobowitz, et al. (1983).

In a manner similar to the MATRIX, socalled SAVER tapes were produced which contain seasonal averages (3 months) of all the products found on the MATRIX tape. The seasons are defined so that the winter season contains data from December through February, the spring season contains data from March through May, etc. Analyzed contour maps of these data are also output on microfilm.

The MAT is also the source for the production of the Solar and Earth Flux Data Tape (SEFDT) which contains one month of solar data (channel 1 through 10) and earth flux data (channels 11 through 14) stripped from the MAT.

As an aid to the analysis of the radiation budget data Zonal Mean Tapes (ZMT) were generated. The general manner in which the flux, albedo and net radiation were determined are given in Appendix B. The ZMT contains tabular listings of zonal averages of the solar insolation, earth emitted flux, albedo and net radiation. Also included are listings of the solar irradiances and selected latitude bands of the emitted flux, albedo and net radiation. The tables present on the ZMT were also placed onto microfilm.

All of the magnetic tapes and microfilm outputs described above and shown on Appendix C are archived at the NASA Space Science Data Center (NSSDC) in Greenbelt, Maryland. The single exception is the ADM tape which is expected to be archived in the future when it contains models for many more additional types of earth surface.

Table 8

Appendix C. ERB MAPPER Products

DATA POPULATION OF WFOV OBSERVATIONS - ASCENDING NODE*
DATA POPULATON OF WFOV OBSERVATIONS - DESCENDING NODE*
DATA POPULATION OF WFOV OBSERVATIONS - ASC + DESC NODE*
L.W. TERRESTRIAL FLUX FROM WFOV OBSERVATIONS - ASCENDING NODE
L.W. TERRESTRIAL FLUX FROM WFOV OBSERVATIONS - DESCENDING NODE
L.W. TERRESTRIAL FLUX FROM WFOV OBSERVATIONS - ASC+DESC NODE

EARTH ALBEDO FROM WFOV OBSERVATIONS (0.2-4.0 um)
EARTH ALBEDO FROM WFOV OBSERVATIONS (0.7-3.0 um)
EARTH ALBEDO FROM WFOV OBSERVATIONS (0.2-0.7 um)
NET RADIATION FROM WFOV OBSERVATIONS

DATA POPULATION OF NFOV OBSERVATIONS - ASCENDING NODE*
DATA POPULATION OF NFOV OBSERVATIONS - DESCENDING NODE*
DATA POPULATION OF NFOV OBSERVATIONS - ASC+DESC NODE*
L.W. TERRESTRIAL FLUX FROM NFOV OBSERVATIONS - ASCENDING NODE
L.W. TERRESTRIAL FLUX FROM NFOV OBSERVATIONS - DESCENDING NODE
L.W. TERRESTRIAL FLUX FROM NFOV OBSERVATIONS - ASC+DESC NODE

EARTH ALBEDO FROM NFOV OBSERVATIONS
MINIMUM EARTH ALBEDO FROM NFOV OBSERVATIONS
NET RADIATION FROM NFOV OBSERVATIONS

NORMALIZED DISPERSION OF L.W. TERRESTRIAL FLUX FROM WFOV OBSERVATIONS - ASCENDING AND DESCENDING NODE

NORMALIZED DISPERSION OF EARTH ALBEDO FROM WFOV OBSERVATIONS

STANDARD DEVIATION OF NET RADIATION FROM WFOV OBSERVATIONS

NORMALIZED DISPERSION OF L.W. TERRESTRIAL FLUX FROM WFOV OBSERVATIONS - ASCENDING AND DESCENDING NODE

NORMALIZED DISPERSION OF EARTH ALBEDO FROM NFOV OBSERVATIONS

STANDARD DEVIATION OF NET RADIATION FROM NFOV OBSERVATIONS

*NOT CONTOURED

7. FUTURE EARTH RADIATION BUDGET PLANS

Present plans call for the production of a ten-year or longer Nimbus ERB global earth radiation budget data set. Eight years of this data have already been recorded and are being processed at the Goddard Space Flight Center under the guidance of the Nimbus ERB Science Team. There are three years of Nimbus-6 ERB data, July 2, 1975 to October 1978 and five years of Nimbus-7 ERB data, November 16, 1978 to the present. In addition, intermittent Nimbus-6 ERB data exists through February 1981 which allows the two data sets to be accurately intercalibrated, (Ardanuy and Jacobowitz, 1984). Both the Nimbus-7 spacecraft and ERB instrument are in good health so that three or more additional years of data are expected. The chopper wheel on the scanner failed on June 22, 1980, hence slightly under 20 months of scanner are available from the Nimbus-7 ERB. Due to several problems only two months, July and August, 1975, of good quality Nimbus-6 scanner data were obtained. Thus, the principle components of the ERB archive will be the solar data and the wide field of view radiation budget data.

As described above the present WFOV flight data calibration algorithms are based on the inflight calibrated longwave scanner data. New WFOV data calibration algorithms are presently being developed to process the ERB data when no IR scanner data are available. These new algorithms, described in Kyle, et al (this issue) are based on the WFOV total channels 11 and 12 which have proved to be very stable. Recent laboratory studies of the behavior of the ERB (Engineering) Model under dynamic, as opposed to equilibrium, conditions combined with ongoing analysis of the flight data gives us confidence in the validity of the new algorithms. Following its final validation, the revised processing software started production the post scanner ERB climate products in the summer of 1983.

Although the major portion of the Nimbus-6 ERB data was recorded before the launch of the Nimbus-7 this data set suffered from a number of initial problems including only partial understanding of the inflight instrument environment and low data processing priorities. The Goddard Applications Directorate is proceeding to reprocess this data using modified Nimbus-7 ERB algorithms and software. Present plans call for the production of Nimbus-6 ERB climate products starting in 1984.

The diurnal variations in the components of the Earth Radiation Budget remains a principle source of uncertainty in estimating the actual Radiation Budget from the observations of a single sun synchronous satellite such as Nimbus-7. To obtain additional information on diurnal variability and to extend the data base the NASA Earth Radiation Budget Experiment (ERBE) plans to put identical Earth Radiation Budget instruments on three satellites: NOAA-F&G and the NASA ERBS- See Barkstrom and Hall (1982). The ERBS will be shuttle launched in August 1984 and placed in a non-sun-synchronous orbit inclined at 57° to the Earth's Equator and at an altitude of 610 km. Its orbit will precess 130° per month. The NOAA satellites are sun synchronous, polar orbiting operational satellites and are launched as required to replace existing weather satellites. It is presently planned to launch NOAA-F in August 1984 into an 850 km orbit with a 2:30 pm local time ascending node equatorial crossing. NOAA-G should be launched about March 1986 but its equatorial crossing time has not been established. Midmorning, noon and midafternoon times are all being considered. Continued operation of the Nimbus-7

ERB after the launch of the NOAA-F and the ERBS satellites will not only allow the Nimbus and ERBE data set to be firmly cross calibrated but will in addition enhance our knowledge of the diurnal variability of the Earth's radiation budget.

Thus present plans call for producing high quality remotely sensed, global earth radiation budget data covering more than one Solar Cycle, June 1975 to the late 1980's. This data will greatly enhance our understanding of Earth-Sun interactions which produce our weather and climate.

REFERENCES

Ardanuy, P. E. and H. Jacobowitz, (1984), A Calibration Technique Combining ERB Parameters from Different Remote Sensing Platforms into a Long-Term Dataset, Submitted to the J. Geophys. Res., 1983.

Ardanuy, P., and J. Rea, (1984), Degradation Asymmetries and Recovery of the Nimbus-7 Earth Radiation Budget Shortwave Radiometer, Submitted to J. Geophys. Res., 1983.

Arking, A., and S.K. Vemury, (1984), The Nimbus 7 ERB Data Set: A Critical Analysis, Submitted to the J. Geophys. Res.

Barkstrom, B.R. and J.B. Hall, (1982) Earth Radiation Budget Experiment (ERBE): An Overview, J. of Energy, 6, pp. 141-146.

Davis, P.A., E.R. Major, and H. Jacobowitz, (1984), An Assessment of Nimbus-7 ERB Shortwave Scanner Data by Correlative Analysis with Narrowband CZCS Data, Submitted to J. Geophys. Res.

Hickey, J. R. and A. R. Karoli, (1974), Radiometer Calibrations for the Earth Radiation Budget Experiment, Appl. Opt., 13. pp. 523-533.

Hickey, J. R., B. M. Alton, F. J. Griffin, H. Jacobowitz, P. Pellegrino and R. H. Maschhoff: (1981), Indications of solar variability in the near UV from the Nimbus 7 ERB experiment, Collection of Extended Abstracts, IAMAP Third Scientific Assembly, Hamburg, F. R. G., Aug. 17-28, 1981, Boulder, CO.

Jacobowitz, H., L. L. Stowe and J. R. Hickey, (1978), The Earth Radiation Budget (ERB) Experiment, The Nimbus-7 User's Guide, NASA Goddard Space Flight Center, Greenbelt, MD, pp. 33-69.

Jacobowitz, H., R. J. Tighe and the Nimbus-7 Experiment Team, (1984), The Earth Radiation Budget Derived from the Nimbus-7 ERB Experiment. (Submitted to JGR).

Kyle, H. L., F. B. House, P. E. Ardanuy, H. Jacobowitz, R. H. Maschhoff and J. R. Hickey, (1984), New inflight calibration adjustment of the Nimbus 6 and 7 Earth Radiation Budget wide-field-of-view radiometers, Submitted to J. Geophys Res.

Maschhoff, R., A. Jalink, J. Hickey and J. Swedberg, (1984), Nimbus Earth Radiation Budget Sensor Characterization for Improved Data Reduction Fidelity, Submitted to the J. Geophys. Res.

Predmore, R. E., Jacobowitz, H., Hickey, J. R., "Exospheric Cleaning of the Earth Radiation Budget Solar Radiometer During Solar Maximum," Spacecraft Contamination Environment, Proc. SPIE vol. 338, pp. 104-113.

Raschke, E., T. H. Vonder Haar, W. R. Bandeen and M. Pasternak. (1973), The Annual Radiation Balance of the Earth-Atmosphere System during 1969-1970 from Nimbus-3 Measurements, NASA TN-7249.

Smith, W. L., D. T. Hilleary, H. Jacobowitz, H. B. Howell, J. R. Hickey and A. J. Drummond, (1977), Nimbus-6 Earth Radiation Budget Experiment, Applied Optics 16, 306-318.

Soule H.V., (1984), Earth Radiation Budget (ERB) Calibration Algorithm History, Research and Data Systems Contractor Report CR 170515, November.

Soule, H. V., (1983), "Nimbus 6 and 7 Earth Radiation Budget (ERB) Sensor Details and Component Tests," NASA TM 83906.

Soumi, N. E., (1961), The Thermal Radiation Balances Experiment Onboard Explorer VII: NASA TN D-608, 11, pp. 273-305, 1961.

Taylor, V. R and L. L Stowe, (1984), Reflectance Characteristics of Uniform Earth and Cloud Surfaces Derived from Nimbus-7 ERB. Submitted to J. Geophy. Res.

Vemury, S.K., L. Stowe and H. Jacobowitz, (1984), "Sample Size and Scene Identification (CLOUD); Efect on Albedo", submitted to J. Geophys. Res.

Appendix A
BASIC RADIOMETRIC
CONVERSION ALGORITHMS

A-1 INTRODUCTION

Initial ERB-6 equations were developed primarily to determine the ERB sensor characteristics before extensive development and testing had been done on them. Using sensor test results these basic equations were modified and used in the ERB-6 data processing.

During early ERB-7 algorithm work the equations developed for ERB-6 were used with modified coefficients. These modifications were based on extensive laboratory testing of both the components and complete ERB-7 sensor configuration.

Post launch data analysis indicated a number of inter-earth channel inconsistencies. There also appeared to be differences between flight and laboratory results. As a result it was decided by the ERB Nimbus Experimental Team (NET) scientists to make a number of algorithm changes. These included:

- o Use of the long wavelength scanning channels (19-22) as a radiation reference and sensor drift correction for the other earth viewing channels.
- o Conversion of channels 19-22 blackbody based radiation data reduction to theoretical earth radiance data reduction using coefficients based on 106 atmospheric theoretical emissions (This conversion will be found in Section A-6).

The resultant basic algorithms are:

A-2 ERB-7 SOLAR CHANNELS (1-10)

For channels 1 to 9 the following is used:

$$H = (V - V_o)/(S_V \cdot f(T_B)) \qquad \text{A-1}$$

where $f(T_B) = 1.0 + 0.01A\,(T_B - 25.00^oC)$

H = Solar irradiance (watts/m^2)

V = Average on sun counts

V_o = Average off-sun counts

S_V = Channel sensitivity at 25°C (counts/watt m^{-2})

A = Temperature correction coefficient (% per °C deviation from 25°C)

T_B = Thermopile base temperature (°C)

For ERB-7 channel 10c a self-calibrating cavity thermopile the equations used to convert counts to irradiance for this channel are:

$$H_{10c} = E_m \, c_f / S_p(T) \qquad \text{A-2}$$

$$E_m = E_{os} - \frac{E(-13) + E(+13)}{2} \qquad \text{A-3}$$

$$S_p(T) = S_0 + S\,(T_H - 22°) \qquad \text{A-4}$$

where

H_{10c} = Channel 10c irradiance (watts/m^2)

c_f = Channel 10c correction factor for aperture area and non-equivalence (m^{-2})

E_{os} = Average channel 10c on sun counts

$E(\pm 13)$ = Average channel 10c counts at ± 13 minutes from on-sun time.

S_0 = Power sensitivity zero level (counts/watt)

S_p = Power sensitivity slope (counts/watt °C)

T_H = Channel 10c heat sink temperature (°C)

A-3 CHANNELS 11 and 12

For these two wide field-of-view sensors the same basic equation was used to convert ERB-6 and ERB-7 counts to blackbody equivalent temperature irradiances. This equation for the fixed earth flux channels 11 and 12 was:

$$H_T \cdot F_T = \left[\Delta W - \epsilon_S F_S \sigma T_S^4 + \epsilon_D F_D \sigma (T_D + k \cdot V)^4\right] \qquad \text{A-5}$$

where

H_T = Target irradiance (watts/m^2)

F_T = Configuration factor of the target

ΔW = Effective irradiance received by Thermopile (Watts/m^2)

ϵ_s = Emissivity of the FOV stop

F_s = Configuration factor of FOV stop

σ = The Stefan-Boltzman constant

T_s = Temperature of the FOV stop (K) (Thermister value)

ϵ_D = Emissivity of the thermopile

F_D = Configuration factor of the thermopile

H_T amount of energy per unit F.

H_T * F_T flux measured at satellite altitude

T_D = Temperature of the thermopile (K) (thermister value)

k = Correction factor for the temperature of the thermopile surface (^oK/count)

V = Thermopile output (counts)

The equation developed for ΔW for ERB-7 is:

$$\Delta W = \frac{V - [V_o + b(T - 25^oC)]}{s + a\,(T - 25^oC)} \qquad \text{A-6}$$

where

V_o = Zero offset in counts at 25^oC

b = Zero offset temperature coefficient (counts/^oC)

T = Module temperature (^oC)

s = Channel sensitivity at 25^oC (counts/Watts m^{-2})

a = Sensitivity temperature coefficient (counts/Watts $m^{-2}/^oC$)

A-4 CHANNELS 13-14

For the ERB-6/7 fixed earth flux channels 13 and 14 the same equations were used to convert from counts to irradiance:

$$H_T = (V - V_o)/s' \qquad \text{A-7}$$

$$s' = s\left[1.0 + (0.01)\,(A)\,(T_B - 25^oC)\right] \qquad \text{A-8}$$

where

H_T = Target irradiance (watts/m^2)

V = Channel output (counts)

V_o = Channel offset (counts determined at a 25°C sensor temperature)

s' = Corrected channel sensitivity (counts/watts m^{-2})

s = Channel sensitivity in vacuum at 25°C

A = Channel sensitivity correction factor (% per °C deviation from 25°C)

T_B = Channel thermopile base temperature (°C)

A-5 CHANNELS 15-18

For Scanning Earth Flux Channels 15 through 18 the ERB-6/7 equations for converting counts to radiances are the same as those given above for fixed earth flux channels 13 and 14, except that the units for s' are (counts/Watts m^{-2} sr^{-1}).

A-6 CHANNELS 19-22

For ERB-6/7 the equation developed at NOAA used to convert from counts to filtered radiance (N_T) was:

$$N_T = N_m + a_o + a_1 \cdot V \qquad \text{A-9}$$

where N_m = module computed filtered radiance ($wm^{-2}ster^{-1}$)

a_o = channel intercept ($w \cdot m^{-2}ster^{-1}$)

a_1 = channel slope ($w \cdot m^{-2}ster^{-1}$/count)

V = channel output (counts)

Coefficients a_0 and a_1 were determined from early inflight calibrations using as a guide preflight thermal-vacuum calibrations.

The module radiance is computed by the solution of:

$$N_m = \exp \left\{ A_0 + A_1 \ln(T) + A_2 \ln(T)^2 + A_3 \ln(T)^3 + A_4 \ln(T)^4 \right\} \quad \text{A-10}$$

Here the coefficients Ai, i=0, 1,....4 were determined prior to launch for the temperature ranges 50K-200K, 200K-298K and 298K-400K

If the filtered radiance reading from the channel is less than or equal to 30.0 W/m^2 sr the unfiltered radiance (R) is computed using the Stefan-Boltzmann law as follows:

$$R = \frac{\sigma T^4}{\pi} \quad \text{A-11}$$

$$\ln R = \ln \left(\frac{\sigma}{\pi}\right) + 4 \ln T = \ln \left(\frac{\sigma}{\pi}\right) + 4 \sum_{n=0}^{4} A_n (\ln R_f)^n \quad \text{A-12}$$

where

R_f = filtered radiance ($Wm^{-2}sr^{-1}$)(in MATGEN $R_f = N_T$)

R = unfiltered radiance ($Wm^{-2}sr^{-1}$)

T = equivalent blackbody temperature (K) (see Attachment B)

σ = Stefan-Boltzmann constant

A_n = regression coefficients determined as indicated in Soule (1984)

Thus, knowing the filtered radiance and the regression coefficients, the unfiltered radiance can be computed. Different sets of regression coefficients are used depending on the filtered radiance value. For telescope readings of the filtered earth irradiance (R_f) greater than 30.0 $Wm^{-2}sr^{-1}$ sr the unfiltered radiance is computed using the formula:

$$R = b_0 + b_1 R_f \quad \text{A-13}$$

where:

b_0 = 8.8584 W/m^2 sr

b_1 = 1.2291

In MATGEN $R_f = N_T$

If the filtered radiance is greater than 300.0 W/m^2 sr the unfiltered radiance value is set "out of range".

Appendix B

FLUX, ALBEDO, NET RADIATION

AND

MONTHLY AVERAGE COMPUTATIONS

B-1 INTRODUCTION

The following algorithms describe the scientific processing which converts input irradiances and radiances into fluxes. In the special cases of channels 5 and 10c, a constant value of the irradiance corresponding to a mean Sun-Earth distance was deduced. The irradiances for any given distance could then be computed by applying the inverse square law.

It should be pointed out here that the ERB parameters which have been designated fluxes are actually flux densities with units of watts per square meter.

For the WFOV, a calibration adjustment is applied to the measured irradiances which was based upon a statistical intercomparison of WFOV and NFOV data. MATRIX computations involving the WFOV shortwave (SW) flux parameters make use of these irradiances (fluxes) measured at the spacecraft. However, the WFOV longwave (LW) flux computation uses fluxes corrected to the top of the atmosphere by the following:

$$\text{LW Flux}_{WFOV} = \text{Irr}_{LW} \cdot R^2_{sat}/(R_{Earth}+15)^2$$

where R_{sat} is the distance from the Earth-center to the spacecraft, and R_{Earth} is the radius of the Earth (both in units of kilometers). R_{Earth} is computed as a function of latitude. The effective radiative surface (top of the atmosphere) is assumed to be located at 15 km altitude.

The computation of NFOV SW fluxes is significantly more complex than the WFOV processing. A procedure based on that developed by Raschke E., et al. (1973) was used to develop the following processing. First, the input radiances are corrected for anisotropy in reflectance dependent upon the surface type of the source target

area (SNOW/ICE, LAND, WATER, or CLOUD). This represents the application of the Angular Dependence Model (ADM). Next, the NFOV SW processing applies a correction for the directional reflectance characteristics of the source target area. In addition, this processing converts the instantaneous fluxes into mean daily NFOV SW fluxes. The complexity of these features means that a significant portion of MATRIX scientific processing is implemented in the NFOV flux computation. Averages over one-day, and monthly periods are computed for all the ERB scientific parameters. In addition, the net radiation is averaged over a six day period which is the approximate repeat cycle of the satellite suborbits.

Average of ERB parameters are written as world grids and as world maps to the MATRIX tape. Daily averaged ERB parameters are output to the MATRIX tape. If the day being processed is the end of a six-day cycle, ERB cyclic averages are output. For the last day of the month, monthly averaged parameters are output. The MATRIX tape is complete when the last six-day cycle started within the calendar month covered by this MATRIX is completed.

B-2 ALBEDO DERIVED FROM THE NFOV CHANNELS.

INPUT:

- N_S - shortwave radiance
- N_L - longwave radiance
- θ - satellite zenith angle
- ζ - solar zenith angle
- Ψ - relative azimuth angle
- ϕ - latitude of target area
- λ - longitude of target area
- S_o - solar constant
- t - day of the year

OUTPUT: $\bar{A}(\phi,\lambda,t)$, mean daily albedo

PROCESS:

1. Compute reflectances, $\pi\rho$ assuming surface reflects diffusely.

$$\pi\rho(\theta,\psi,\zeta,\lambda,t,\phi) = \frac{\pi N_s(\theta,\psi,\zeta,\gamma,\lambda,t)}{S_o L(t)\cos\zeta}$$

where $L(t) = \left(\frac{\bar{d}}{d(t)}\right)^2$; $d(t)$ is the Earth-Sun distances and $\bar{d}$ is the annual mean Earth-Sun distance.

2. Determine target scene type M(land, water, snow/ice, or cloud) from the values of $\pi\rho$ and N_L utilizing the scene selection algorithm diagramed schematically in Figure B-1.

3. Obtain the anisotropic factor $R(\Theta,\psi,\zeta,M)$* from the angular model corresponding to scene type M for the solar angle ζ and viewing angles Θ and ψ.

4. Compute the reflectances, r, corrected for anisotropy.

$$r(\zeta,\phi,\lambda,t,M) = \pi\rho(\theta,\psi,\zeta,\phi,\lambda,t)\ R(\theta,\psi,\zeta,M)$$

5. Compute the daily directional average reflected flux, W_R.

$$W_R(\phi,\lambda,t) = S_o.L(t).r(\zeta = 0,\lambda,t,M).\frac{1}{12}\int_{t_{SR}}^{t_n}\left(\frac{r(\zeta)}{r(0)}\right)_M \cos\zeta d\tau^*$$

where $r(\zeta = 0,\phi,\lambda,t,M) = \dfrac{r(\zeta,\phi,\lambda,t,M)}{\left(\frac{r(\zeta)}{r\ 0}\right)_M}$;

$(r(\zeta)/r(0))_M$ are normalized directional reflectance models and t_{SR} and t_n are respectively the times of the local sunrise and noon.

*Model derived from the Nimbus 7 ERB data

6. Compute the daily average reflected flux averaged over all observations, $\overline{W}_R$.

7. Compute the daily averaged insolation, $\overline{H}_s$

$$\overline{H}_s(\phi,\lambda,t) = S_o L(t) \cdot \frac{1}{12}\int_{t_{SR}}^{tn} \cos\zeta d\tau^*$$

8. Compute the mean daily albedo, $\overline{A}$

$$\overline{A}(\phi,\lambda,t) = \frac{\overline{W}_R(\phi,\lambda,t)}{\overline{H}_s(\phi,t,\lambda)}$$

B-3 OUTGOING LONGWAVE FLUX FOR THE NFOV CHANNELS

INPUT:

- N_L - longwave radiance
- Θ - satellite zenith angle
- ϕ - latitude of target area
- t - day of the year

OUTPUT: $\overline{W}_L(\phi,\lambda,t)$ - mean daily outgoing longwave flux.

PROCESS:

1. Determine whether the FOV was during the daytime, D, or nighttime, N.
2. Compute the emitted flux, W_L, corresponding to a given observation.

$$W_L^{(D,N)}(\phi,\lambda,t) = N_L^{(D,N)}(\theta=0,\phi,\lambda,t)2\pi \int_0^{\pi/2} \left(\frac{N_L(\theta,\phi)}{N_L(\theta=0,\phi)}\right)_M \cos\theta\sin\theta d\theta$$

where $N_L^{(D,N)}(\theta=0,\phi,\lambda,t) = \dfrac{N_L^{(D,N)}(\theta=0,\phi,\lambda,t)}{\left(\frac{N_L(\theta,\phi)}{N_L(0,\phi)}\right)_M}$

$\left(\frac{N_L(\theta,\phi)}{N_L(0,\phi)}\right)_M$ * is model of the limb-darkening.

*Model derived from Nimbus-7 ERB data

3. Compute the daytime and nighttime fluxes $\overline{W}_L{}^D$ and $\overline{W}_L{}^N$, averaged over all observations of the target areas.
4. Compute the daily averaged emitted flux, $\overline{W}_L$:

$$\overline{W}_L(\phi,\lambda,t) = \frac{T_D\overline{W}_L^D(\phi,\lambda,t)+T_N\overline{W}_L^N(\phi,\lambda,t)}{24}$$

where T_D and T_N are respectively the number of hours that the target is in daylight or is during the nighttime, respectively.

B-4 NET RADIATION DERIVED FROM THE NFOV CHANNELS

INPUT:

$\bar{A}$ - Daily averaged albedo
$\overline{W}_L$ - daily averaged longwave flux
$\overline{H}_S$ - daily averaged insolation
ϕ - latitude of the target area
λ - longtitude of the target area
t - day of the year

OUTPUT: $(\overline{N}(\phi,\lambda,t)$, mean daily net radiation

PROCESS: $\overline{N}(\phi,\lambda,t) = \left[1.0 - \overline{A}(\phi,\lambda,t)\right] \cdot \overline{H}_s(\phi,t) - \overline{W}_L(\phi,\lambda,t)$

B-5 ALBEDO DERIVED FROM THE WFOV CHANNELS

INPUT:

I_S - shortwave irradiance
a - calibration adjustment slope
b - calibration adjustment offset
t - day of the year
ϕ - latitude of subpoint target area
λ - longitude of subpoint target area
S_0 - solar constant

OUTPUT: $\overline{A}(\phi,\lambda,t)$, daily albedo

1. Compute the adjusted reflected flux, F
   $F = aI_S + b$
2. Compute the maximum reflected flux, F_M, that would be expected if the field-of-view was a perfectly reflecting diffuse surface.
3. Compute the values of F and F_M by averaging over all observations in a target area.
4. Compute the daily albedo, A
   $A(\phi,\lambda,t) = (\overline{F}(\phi,\lambda,t)/(\overline{F}_M(\phi,\lambda,t)$

B-6 OUTGOING LONGWAVE FLUX DERIVED FROM THE WFOV CHANNELS

INPUT:

I_T	- total irradiance	ϕ	- latitude subpoint target areas
I_S	- shortwave adjusted irradiances	λ	- longitude of subpoint target area
R_{sat}	- altitude of the satellite	t	- day of the year
		F_M	- ---

OUTPUT: $\overline{W}_L^{(D,N)}(\phi,\lambda,t)$ - mean outgoing flux for daytime or nighttime

PROCESS: 1. Compute the longwave irradiance, I_L from the observation of the total and shortwave irradiances for both daytime and nighttime.

$$I_L{}^D = I_T{}^D - I_S{}^D \qquad F_M > 0 \;\&\; I_s > 0$$

$$I_L{}^N = I_T{}^N \qquad F_M = 0 \text{ or } I_s < 0$$

2. Compute the longwave flux adjusted to the top of the atmosphere (15 km)

$$W_L{}^{(D,N)}(\phi,\lambda,t) = I_L{}^{(D,N)}(\phi,\lambda,t) \left(\frac{R_{sat}}{R_e + 15}\right)^2$$

R_e = mean radius of the earth

3. Compute the longwave fluxes, $\overline{W}_L^D$ and $\overline{W}_L^N$, averaged respectively over all observations of the target during the daytime and nighttime. No daily averaged longwave flux was computed for single days.

B-7 NET RADIATION DERIVED FROM THE WFOV CHANNELS

INPUT:
- $\overline{A}$ - daily albedo
- $\overline{W}_L^D$ - daytime averaged longwave flux
- $\overline{W}_L^N$ - nighttime average longwave flux
- $\overline{H}_S$ - daily averaged insolation
- ϕ - latitude of subpoint target
- λ - longitude of subpoint target
- t - day of the year
- k - see footnote *

OUTPUT: $\overline{N}(\phi,\lambda,t)$ - mean daily net radiation

PROCESS:
$$\overline{N}(\phi,\lambda,t) = \left[(1.0 - k\overline{A}(\phi,\lambda,t)\right] \overline{H}_S(\phi,t) - \frac{\overline{W}_L^D(\phi,\lambda,t) + \overline{W}_L^N(\phi,\lambda,t)}{2}$$

if $\overline{W}_L^D$ and $\overline{W}_L^D$ both exist;

$$\overline{N}(\phi,\lambda,t) = [1.0 - k\overline{A}(\phi,\lambda,t)] \cdot \overline{H}_S(\phi,t) - \overline{W}_L^D$$

if only W_L^D exists.

---

*k is a factor relating the albedo observed generally near noon to the mean daily albedo. k is computed only from directional reflectance models and does not take account of the changing scene other than solar zenith angles.

B-8 COMPUTATION OF THE MONTHLY MEAN VALUES

$\tilde{X}$ (...) is the monthly average of $\bar{X}$ (...,t) over all observation days of the month.

(1) Albedo (NFOV)

$$\tilde{A}(\phi,\lambda) = (\tilde{W}_R(\phi,\lambda)/\tilde{H}_s(\phi))$$

(2) Outgoing longwave flux (NFOV) - $\tilde{W}_L(\phi,\lambda)$

(3) Net radiation flux (NFOV) - $\tilde{N}(\phi,\lambda)$

(4) Albedo (WFOV)

$$\tilde{A}(\phi,\lambda) = \frac{\sum_{i=1}^{M} k_i \bar{F}(\phi,\lambda,t_i)}{\sum_{i=1}^{M} \bar{F}_M(\phi,\lambda,t_i)}$$

where k and t_i are the albedo correction factors and day of the year, respectively, for each of the observation days of the month.

(5) Outgoing longwaves flux (WFOV)

$$\tilde{W}_L(\phi,\lambda) = \frac{\tilde{W}_L^D(\phi,\lambda) + \tilde{W}_L^N(\phi,\lambda)}{2}$$

(6) Net radiation flux (WFOV)

$$\tilde{N}(\phi,\lambda) = [1.0 - \tilde{A}(\phi,\lambda)] \cdot \tilde{H}_s(\phi,\lambda) - \tilde{W}_L(\phi,\lambda)$$

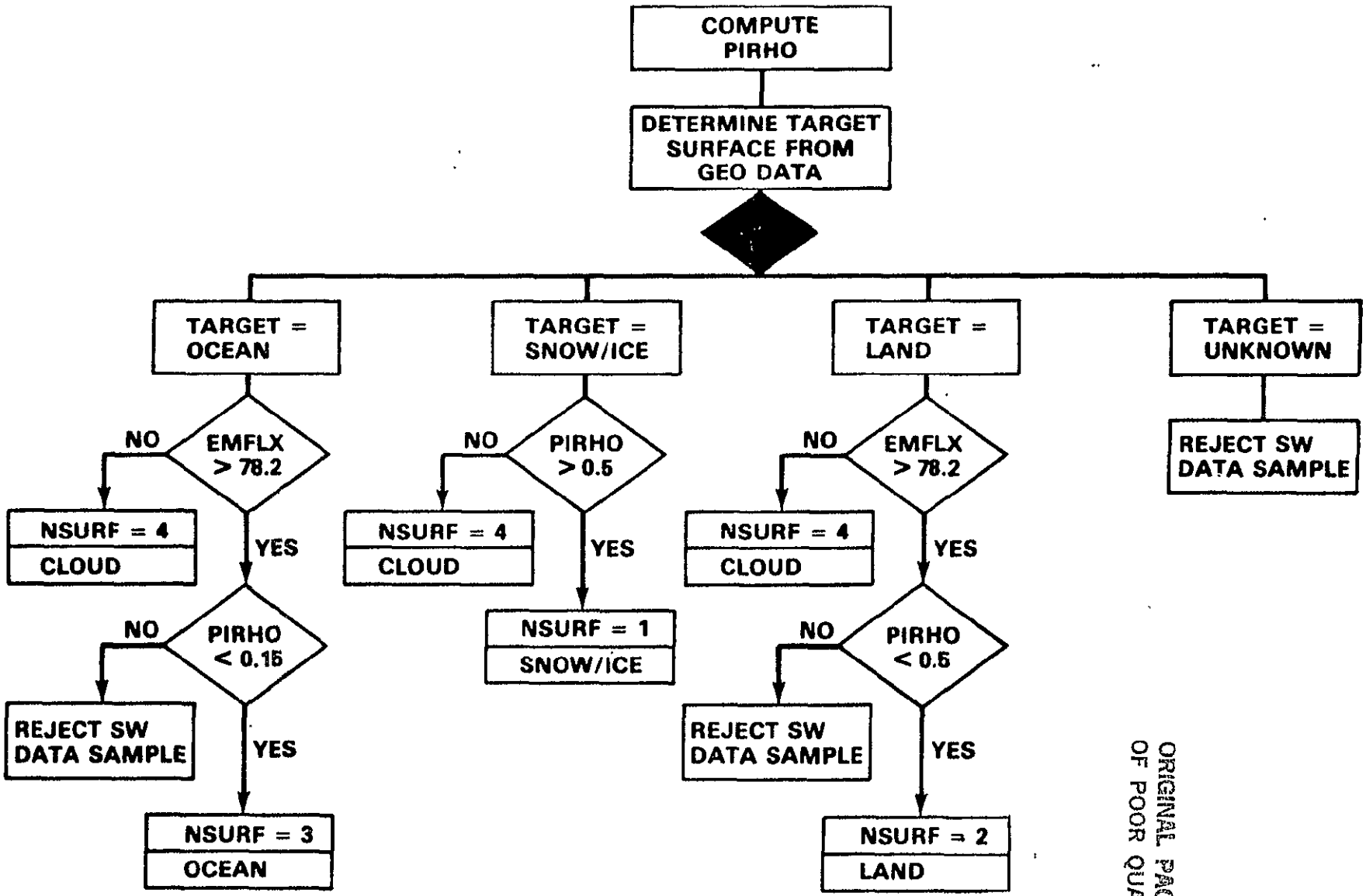

Fig. B1. Scene selection algorithm PIRHO, $\pi\rho$; EMFLX, emitted flux; NSURF, surface type 1-snow/ice, 2-land, 3-ocean, 4-cloud; SW, shortwave; GEO, geographic

SECTION 2. THE EARTH RADIATION BUDGET DERIVED FROM THE NIMBUS-7 ERB EXPERIMENT

THE EARTH RADIATION BUDGET DERIVED FROM THE NIMBUS-7 ERB EXPERIMENT

Accepted for Publication in Journal of Geophysical Research

March 1, 1983

by

Dr. Herbert Jacobowitz
NOAA/National Environmental Satellite Data and Information Service
Washington, D.C. 20233

Dr. Richard J. Tighe
Systems and Applied Sciences Corporation
5809 Annapolis Road, Suite 400
Hyattsville, Maryland 20784

and

The Nimbus-7 ERB Experiment Team*

*Team Members and affiliations listed after text.

ABSTRACT

The Earth Radiation Budget (ERB) as determined from the ERB experiment aboard the Nimbus-7 Polar-Orbiting Satellite is presented in the form of time-latitude cross-sections, hemispherically and globally averaged time-plots, and annual global averages for the time period spanning November 1978 through October 1979. Comparisons are made between results derived from the fixed Wide Field-of-View (WFOV) radiometers and those derived from the scanning Narrow Field-of-View (NFOV) radiometers. While there is excellent agreement in regard to the spatial and temporal variations, the absolute magnitudes differ. The NFOV yields outgoing longwave fluxes and albedos that are respectively about 4 W/m^2 and 2.5% greater than those derived from the WFOV sensors. Also, limited simultaneous comparisons are made between ERB results and those from the AVHRR on the NOAA-7 operational satellite.

TABLE OF CONTENTS

1. INTRODUCTION

The measurement of the spatial and temporal variations of the radiation budget of the earth is essential for our understanding of climatic change. Not only does the radiation budget influence the behavior of other climate variables, but changes in these variables cause changes in the radiation budget itself. The measurements obtained with the ERB instrument (Jacobowitz, 1978) onboard the Nimbus-7 satellite yield a unique data set that is a valuable source of knowledge of the radiation budget. The data set combines highly accurate and precise observations of the solar irradiance with very stable observations of the reflected and emitted outgoing terrestrial radiation. These terrestrial observations are made simultaneously with fixed WFOV and scanning NFOV radiometers. While the WFOV channels act as an integrator of the outgoing radiation over the entire earth's disc visible from the satellite, the NFOV channels permit variations within the visible earth's disc to be observed (mean resolution is around 150 km by 150 km). However, these NFOV channels are capable of only observing an earth scene from a limited number of directions. As a result, angular distribution models must be employed in order to interpret these directional observations in terms of an angularly integrated outgoing flux. To this end, the NFOV channels, themselves, have been an excellent source of data for constructing the required angular distribution models (Taylor and Stowe, 1983).

2. THE DATA SET

Beginning on November 16, 1978 the ERB instrument has been operating routinely on a 3-day ON and a 1-day OFF cycle with perhaps only a few minor interruptions of this schedule. Not too long after the start of ERB operations it became apparent that when in scan mode the ERB NFOV channels were causing perturbations in the spacecraft attitude that were above the tolerance levels of the Limb Infrared Monitor of the Stratosphere (LIMS), also onboard the spacecraft. Since the LIMS experiment was expected to have a short lifetime (around six months) the ERB experiment had to make some compromises. Beginning on December 10, 1978 and lasting through May 22, 1979 the scanning time period of the ERB channels was cut down from the three out of four days cyle to only two out of four days; two days of scanning followed by two days of no scanning. While the NFOV channels were still electronically turned on during one of the non-scan days and they were pointed in the nadir direction, the data were not processed into mean fluxes or albedoes because of the rather limited coverage that they offered. Also, during a very special observation period for the LIMS experiment, the NFOV channels were commanded to a non-scan mode every time the satellite was over the latitudes from 80^{o}N to 27^{o}S on the descending (mostly nighttime) portion of each orbit. This was in effect from January 4, 1979 to February 6, 1979. As a result, very few outgoing longwave measurements were made of the northern hemisphere at night during this time interval. During all these compromises, all other channels continued to operate on a normal schedule.

The data set that will be analyzed here comes from the time period of November 16, 1978 through the end of October 1979 which nearly constitutes the first year of data.

The raw data to be processed were first sorted into a number of geographic target areas (2070) which are roughly of equal area and which span the entire globe. The albedo, outgoing longwave flux and net radiation flux were then computed for each target on a daily, monthly, and seasonally averaged basis for both the WFOV and NFOV channels. The monthly and seasonally averaged values were then plotted and analyzed on both mercator and polar stereographic map bases. Monthly and seasonally mean values were also averaged over 4.5^{o} latitude bands. The monthly latitude band averages were then utilized to generate time-latitude cross-sections in order to study the spatial and temporal variability of the zonal average radiation budget. In addition, the time variation of the global and hemispherical monthly means were also analyzed.

3. ANALYZED MAPS

Analyzed maps of the radiation budget parameters are extremely useful in depicting the spatial variations in the parameters. Month-to-month comparisons as well as satellite-to-satellite comparisons can be made for any given time period.

Figures 1(a), 1(b), and 1(c) display three mercator maps of the albedo for March 1979 derived from three independent sensors. Figures 1(a) and 1(b) were derived from the WFOV and NFOV channels of ERB, respectively, while Figure 1(c) was derived from the Advanced Very High Resolution Radiometer (AVHRR) on the TIROS-N satellite which has a resolution of about 1 km by 4 km at nadir. It should be pointed out that the orbits of TIROS-N cross the equator around 2:30 a.m. and p.m., while those for Nimbus-7 cross the equator at 12:00 p.m. and midnight.

Note the degree of similarity in the patterns for the ERB NFOV and AVHRR maps, particularly in the regions of north Africa, the northern part of South America, and the Pacific Ocean. Although the magnitudes do not appear to differ very much, some idea of the actual differences can be obtained by studying the displacement in corresponding contours in going from one map to the other. For example, the east-west 30 percent contour south of Australia on the AVHRR map runs through parts of southern Australia on the ERB NFOV map indicating that the ERB values are higher in magnitude. A 40 percent contour is present in South Africa on the ERB map which is absent on the AVHRR map. Overall, the albedos derived from the ERB NFOV instrument are higher than those derived from the AVHRR. The differences could be due to a number of causes. First, the AVHRR made measurements in the narrow spectral interval of 0.55 to 0.90 m while the ERB made measurements in the broad spectral band from 0.2 to 4 m. Second, the AVHRR processing utilized an isotropic angular model while the ERB employed models dependent upon viewing angle, solar zenith angle, and surface type. An important additional difference was that the ERB used directional models (reflectance versus solar zenith angle) to estimate the mean daily albedo from the albedo determined for the single observation time. This mean daily albedo is what is mapped in Figure 1. The albedo determined for the time of the TIROS-N orbits is what was plotted for the AVHRR. However, estimates of corrections to be made to the AVHRR albedo to yield the mean daily albedo are close to unity. The map from the ERB WFOV instrument has the same general features as those for the other two maps but, because of its lower resolution, detailed variations present in the other maps are lost. Comparison of magnitudes again show that the ERB NFOV albedos are on the high side.

A comparison of the corresponding daytime longwave radiation flux for the three sensors is shown in Figure 2. Fairly good agreement in the patterns is observed in the maps of the ERB NFOV and AVHRR although the magnitudes of the fluxes obtained from the

AVHRR are somewhat higher than those from the ERB. While the agreement is excellent for Australia, the AVHRR values are higher to the north and east of Australia. Considering the approximately two and a half hours differences in the observation times of the two satellites, the monthly averages show no strong diurnal variability. Perhaps those regions for which there is good agreement, like the deserts, there is little diurnal change during the two and a half hours. Those regions which exhibit larger differences may have a stronger diurnal variation. It should be noted that the AVHRR observations are made in the 10-11 μm window region and are converted to a broad band flux using a regression relationship (Gruber, 1976; Gruber and Winston, 1978). A comparison of the ERB WFOV maps with the other two maps show that the predominant features are still present in the WFOV map although many smaller features can no longer be distinguished. The magnitudes of the WFOV fluxes are lower than those of the NFOV and AVHRR.

4. TIME-LATITUDE CROSS-SECTIONS AND HEMISPHERICAL AND GLOBAL TIME SERIES

Another very useful way of displaying the spatial and temporal variations of the radiation budget is by means of the time-latitude cross-section. This is formed from the zonally averaged monthly means for all of the availble months with latitude on the vertical axis and month on the horizontal axis. Contours of equal values of the zonal averages are drawn on this grid similar to that found on the monthly maps. However, in these cross-sections we have time as one of the variables.

In addition to these time-latitude cross-sections, one can derive hemispherical and global means for each month by appropriately averaging the zonal means over each hemisphere as well as over the entire globe. Plots of these averages versus time (month in our case) are extremely useful for understanding the nature of the annual variations.

Figures 3(a) and 3(b) show the time-latitude cross-sections for the albedo derived from the WFOV and NFOV channels, respectively, for the period of time spanning November 1978 through October 1979 and Figure 3(c) shows their difference.

Notice the tendency toward larger albedos at the higher latitudes which may be caused by a number of contributing factors. One of these is the general increase of reflectivity with increase in the solar zenith angle. Solar radiation entering the atmosphere is incident at zenith angles which are greater at higher latitudes, hence the higher albedos there. This same factor can be observed at a given latitude in the annual cycle. For example, consider the latitudes between 30^{o} and 60^{o}S. The lowest albedos occur around December and January when the solar zenith angles are the lowest while the largest albedos occur in June when the solar zenith angles are the highest. This is also observed in the corresponding northern latitudes with the largest albedos occurring in December and the lowest occurring around June, the months corresponding to the largest and lowest solar zenith angles, respectively, for this hemisphere.

Another factor that will tend to cause the albedo to increase with latitude is the increase in the snow and ice cover. The very extensive Southern Antarctic continent with its snow and ice cover yield zonally averaged albedos at the very high latitudes that are greater than those of the high northern latitudes. A third contributing factor is the occurrence of a greater amount of cloudiness at the higher latitudes.

The seasonal variations of the albedo discussed above do not apply to the tropical regions. In fact, there is a tendency toward higher albedos in the summer. This may be caused by the presence of a greater amount of cloudiness during the summer months compared to that for winter which may be associated with

movements of the Intertropical Convergence Zone (ITCZ).

The consequences of all of the variations discussed above on the hemispherical and global means can be seen in Figures 4(a) and 4(b). In the northern hemisphere (hereafter referred to as N.H.) we observe two packs. One of these occurs around October and November while an even larger peak occurs around May, in spite of the fact that the larger albedos in the middle and higher latitudes occurs around December. This can be explained on the basis that the greatest contributors to the hemispherical means come from the tropical latitudes. Not only is half the area of the earth confined below 30° of latitude, but the solar insolation is much greater in these latitudes. Therefore, the albedos for the tropics are more highly weighted in the hemispherical or global means than the middle or higher latitudes. The influence of the middle and higher latitudes is still present and is the cause of the secondary peak.

In the southern hemisphere (S.H.) the variation of the albedo in the tropics with season is much less pronounced than that observed in the N.H. The variation of the hemispherical mean is therefore driven by the variations in the middle and higher latitudes. The dip in the albedo towards June is directly related to the decreasing influence of the Antarctic continent whose insolation in June is nerly zero.

The combined effect of the two hemispheres can be seen in the global means varition where the prominent peaks and valleys of the curve for one hemisphere are nearly offset by the peaks and valleys of the other hemisphere. However, since the peaks of one hemisphere do not occur at exactly the same time as the valley of the other hemisphere there is some residual variation. Results derived for the first two years (July 1975 through June 1977) from the Nimbus-6 ERB WFOV (Jacobowitz, et. al. 1979) are also included on the global mean plots for comparison. Corresponding months for the two years were simply averaged together and plotted. The degree to which the curves for the two WFOV instruments agree should be noted.

An examination of the difference contour plots (Figure 3(c)) shows that NFOV albedo is higher than that derived from the WFOV data. In the S.H. the greatest difference occurs around May through September in the mid-latitudes while in mid-latitudes of the N.H. the greatest differences are from August to February. In the tropics the greatest differences are confined to the period from March to November. The hemispherical and global mean plots clearly show these differences. In the mean there is the tendency for the difference to increase with time. While the NFOV albedo does show a small downward trend over the year, the trend is stronger in the WFOV values.

Figures 5(a), 5(b), and 5(c) show the time-latitude cross-sections for the outgoing longwave flux derived from the WFOV and NFOV observations and their difference and Figures 6(a) and 6(b) show the corresponding hemispherical and global averages. The flux is computed from both the ascending (mostly daytime) and

descending (mostly nighttime) portions of each orbit). The prominent features to be noted are the strong seasonal effects in the N.H. with the greatest flux occurring in the summer months. In the S.H., the trend is similar but weaker due mainly to the moderating effect of the oceans which are much more plentiful in the S.H. (Note the lower value of the flux near the south pole in winter compared to that near the north pole during its winter). In the N.H. time plot there is a strong maximum in the summer and a corresponding strong minimum in winter. The S.H. plot shows a small maximum in November and a shallow minimum around May. Globally the variations in time are driven by the variations in the N.H. with its greater land mass.

A comparison of the WFOV and NFOV values depicted in Figure 5(c) shows that the fluxes derived from the NFOV data are generally greater than those derived from the WFOV data with the greatest difference occurring around January and February in the regions of the lower latitudes. The reason for these large differences in January and February can be traced to the operational requirement discussed earlier, whereby the scan channels (NFOV) were placed in a non-scan mode for the portion of each descending orbit from 80^{o}N to 27^{o}S for the time period of January 4 to February 6, 1979. This was done to provide the LIMS experiment, on the same satellite, an opportunity to make some important observations without the perturbing influence of the ERB when scanning occurred.

As a result, the N.H. and a portion of the S.H. were inadequately sampled at night. Therefore, the average longwave flux is weighted strongly toward the daytime observations for this period. Since the higher latitudes in this period have nighttime fluxes that are not too different from their daytime values, the sampling bias is not noticeable. However, this is not the case for the lower latitudes where strong diurnal variations are present. As a result, the daily averaged longwave fluxes are too high. Figure 6(a) shows this clearly for the N.H. while the influence of the limited scan on the S.H. averages is much less. The global plot of Figure 6(b) shows the mean bias to be around 4 W/m^2 for the entire year and over 5 W/m^2 in January and February. Included in the figure is the longwave flux derived from the Nimbus-6 ERB WFOV. Although the variations are similar to those we observed from the Nimbus-7 sensors, the magnitude is quite high. No explanation is available for the dip in the Nimbus-6 curve in January except that the value for January 1977 was quite low.

Figures 7(a), 7(b), and 7(c) show the time-latitude cross-sections for net radiation flux for the WFOV and NFOV observations and their difference and Figures 8(a) and 8(b) show the the hemispherical and global mean time plots. One thing that is immediately evident from the time-latitude cross-sections is the way that most of the contours follow the declination curve. This suggests that the variation in the net radiation flux is strongly tied to the variation of the solar declination. This is not too surprising since the solar insolation at any latitude is

dependent upon the solar declination. The curves of the net radiation for the N.H. and S.H. show clearly the influence of the declination. The maximum in the N.H. and the minimum in the S.H. occur in June while the minimum in the N.H. and the maximum in the S.H. occur in December, the months of the solstices. Also, the maximum in the S.H. exceeds that in the N.H. This can be seen on the time-latitude cross-sections. This again is due to the variation in the solar insolation but this time it is caused by the variation in the sun-earth distance which is a minimum in January and a maximum in July. While the solar declination would have little effect on the "globally averaged" net radiation, the variation in the sun-earth distance is the dominant feature. The deviation of the globally averaged insolation from its annual mean value is given in Figure 8(b). Both the WFOV and NFOV curves of the net radiation are in phase with it. The net radiation derived from the Nimbus-6 WFOV is included for comparison. Notice how its curve lies between those for the Nimbus-7 WFOV and NFOV.

The difference between the WFOV and NFOV estimates of the net radiation are a result of the differences in the albedo and outgoing longwave flux previously discussed. Averaged over the entire year, the net radiation deduced from the WFOV channels is about 14 W/m^2 greater than that deduced from the NFOV channels.

5. SUMMARY AND CONCLUSIONS

Table 1 summarizes the annual averages of the hemispherical and global means derived from both the WFOV and NFOV channels. Both the WFOV and NFOV albedos are higher in the N.H. than in the S.H. which can be explained by the fact that there is a greater land mass in the N.H. On the average, land surfaces reflect more solar energy than the oceans. We also observe that the mean longwave flux is slightly greater in the N.H. However, the difference is close to the level of precision for either instrument so that the result may not be significant. For the purpose of comparing these results with those derived from other observations, the global results from the Nimbus-7 ERB are tabulated (Table 2) along with those derived from the Nimbus-6 ERB WFOV, the series of NOAA Scanning Radiometers (Gruber, 1978; Ohring and Gruber, 1983) denoted by SR, the satellite composite derived by Ellis and Vonder Haar (1976) denoted by EV, and finally that derived from the Nimbus-6 ERB NFOV data by Campbell and Vonder Haar (1980) denoted by CV. With the exception of the albedo derived from the Nimbus-7 NFOV, all the results are fairly consistent. The longwave flux estimates from the scanning radiometers are biased on the high side. However, the results given have been repeated onboard three separate satellites, all of which agreed to within 1 W/m^2. Since the estimates were based upon the observations in a narrow band around the 11 m window region, one must suspect the algorithm which estimates the broad band flux from the narrow band measurements as being the cause of the high estimates. A new algorithm has been developed which reduces the bias.

The high value of the albedo derived from the Nimbus-7 ERB NFOV channels is of concern since it is inconsistent with the other estimates although the latitudinal and month-to-month variations are quite similar to those derived from the WFOV channels. Some recent studies (Stowe, et. al. 1983) have revealed that estimates of the albedo were generally higher when the scanning channels viewed the earth at large nadir angles (above 56°) compared to those made at lower angles. Since the number of observations made with this instrument tended to increase with an increase in the nadir angle, a sizeable bias in the results could have been generated. An algorithm which would eliminate these biases from the data is currently under investigation. Also under development are some refinements to the processing of the WFOV channels (Kyle, et. al. 1983) which are aimed at removing some biases in the data introduced by the satellite on-off cycle (three days on, followed by one day off) as well as removing other biases caused by the influence of the shortwave and longwave terrestrial and solar radiation on the filter domes and detector modules.

The results presented in this article are not expected to be changed substantially by the modifications discussed above.

TABLE 1.

Annual Avergaes of Global and
Hemispheric Means of the Radiation Budget
Derived from the Nimbus-7 ERB

		Albedo (%)	Longwave Flux (W/m^2)	Net Flux (W/m^2)
WFOV	N.H.	30.9	229.4	8.1
	S.H.	30.2	228.1	13.7
	Global	30.6	228.8	10.9
NFOV	N.H.	33.6	233.1	- 5.1
	S.H.	32.7	232.3	- 1.8
	Global	33.1	232.7	- 3.4

TABLE 2.

Comparison of Nimbus-7 ERB Results with Those from Other Observations

	ALBEDO* (%)	LONGWAVE FLUX* (W/m^2)
N-7 WFOV	31	229
N-7 NFOV	33	233
N-6 WFOV	31	235
SR	31	244
EV	30	236
CV	31	230

*All results have been rounded off to the nearest integer.

Removal of the biases in the NFOV albedo should yield values that are much closer to those derived from the WFOV data. The modifications to the WFOV are expected to decrease the downward trend in the albedo bringing the variation more in line with the trend observed for the NFOV albedo.

Overall, the Nimbus-7 ERB has yielded an excellent data set to study the spatial and temporal variations on both the planetary and synoptic scales. As results from additional months become available, we will be able to analyze the interannual differences essential to most studies of climatic change.

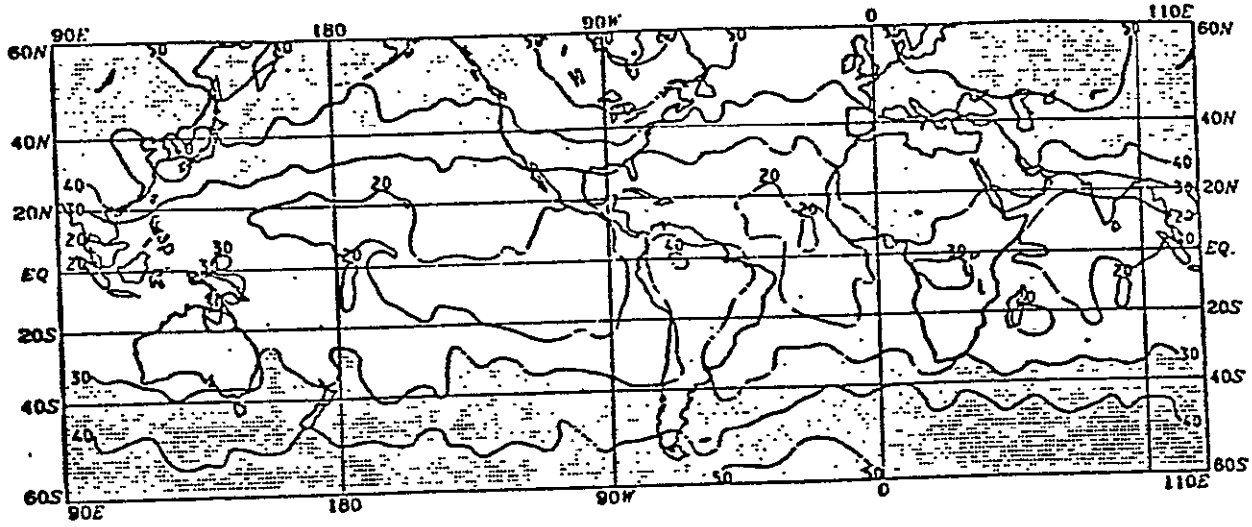

(a) ERB - WFOV

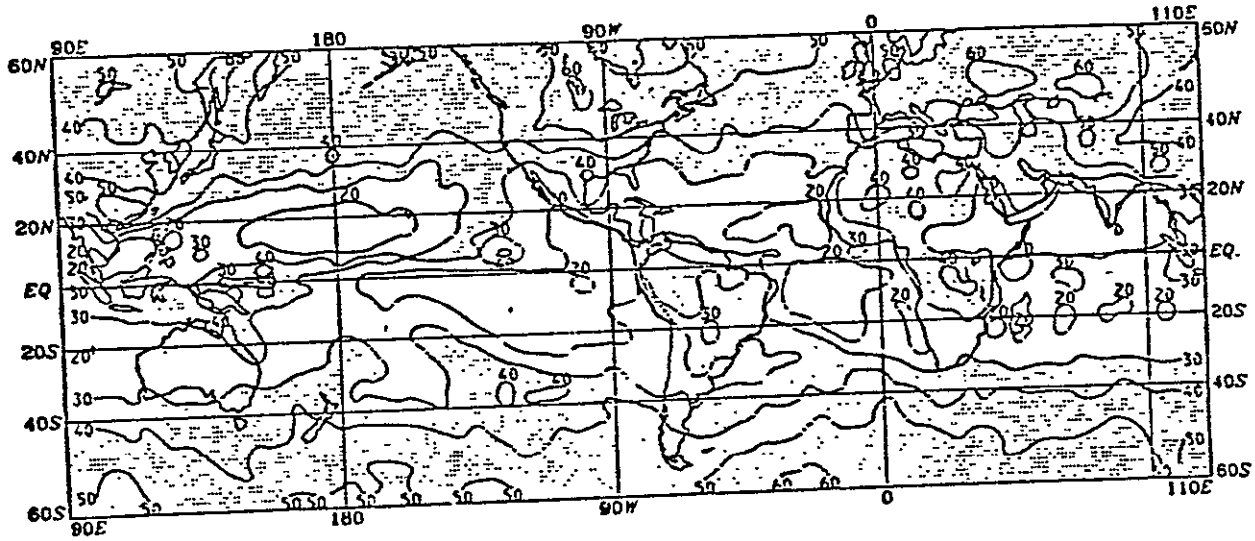

(b) ERB - NFOV

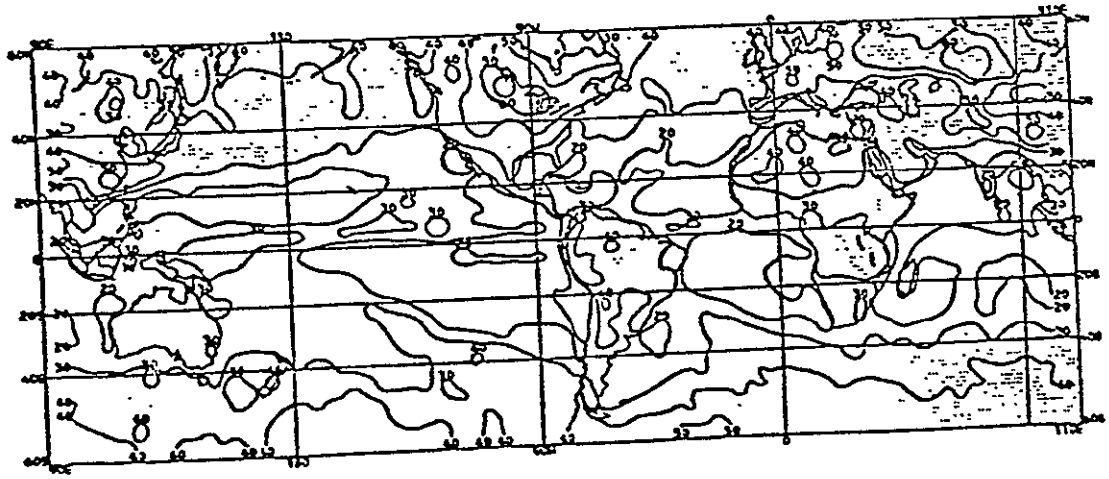

(c) AVHRR

FIGURE 1: Analyzed Maps of Albedo for March 1979. The a, b, and c are derived from the ERB WFOV, ERB NFOV, and AVHRR instruments, respectively. Values greater than 30% are shaded.

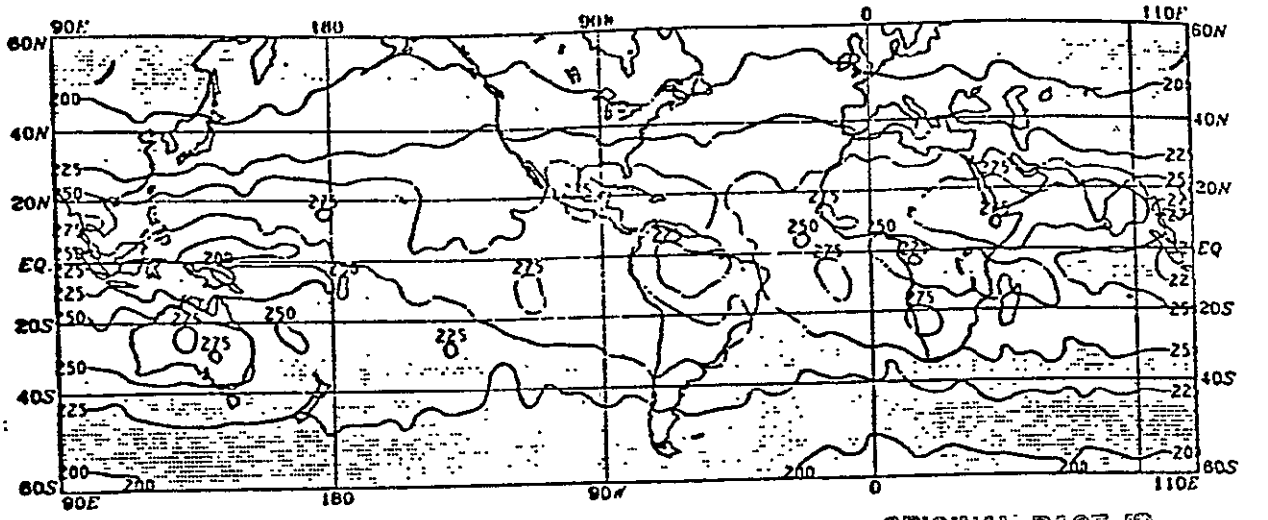

(a) ERB - WFOV

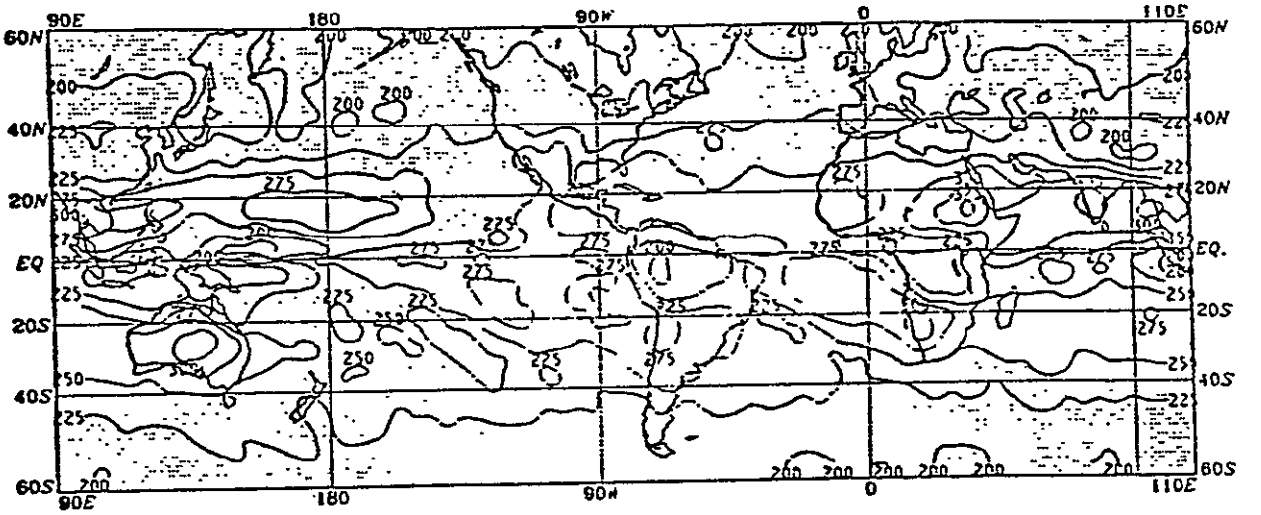

(b) ERB - NFOV

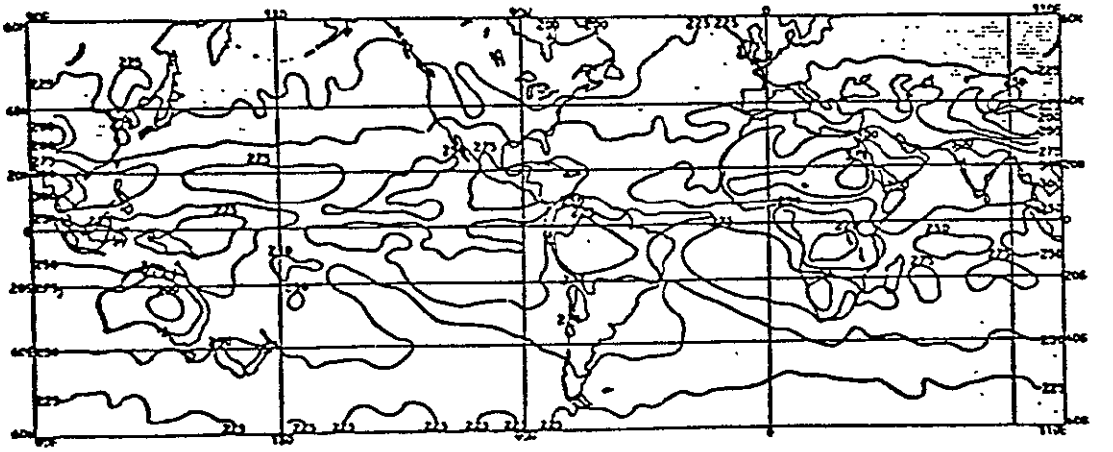

(c) AVHRR

FIGURE 2: Analyzed maps of daytime outgoing Longwave Flux for March 1979. The a, b, and c are derived from the ERB WFOV, ERB NFOV, and AVHRR instruments, respectively. Values less than 250 W/m^{-2} are shaded.

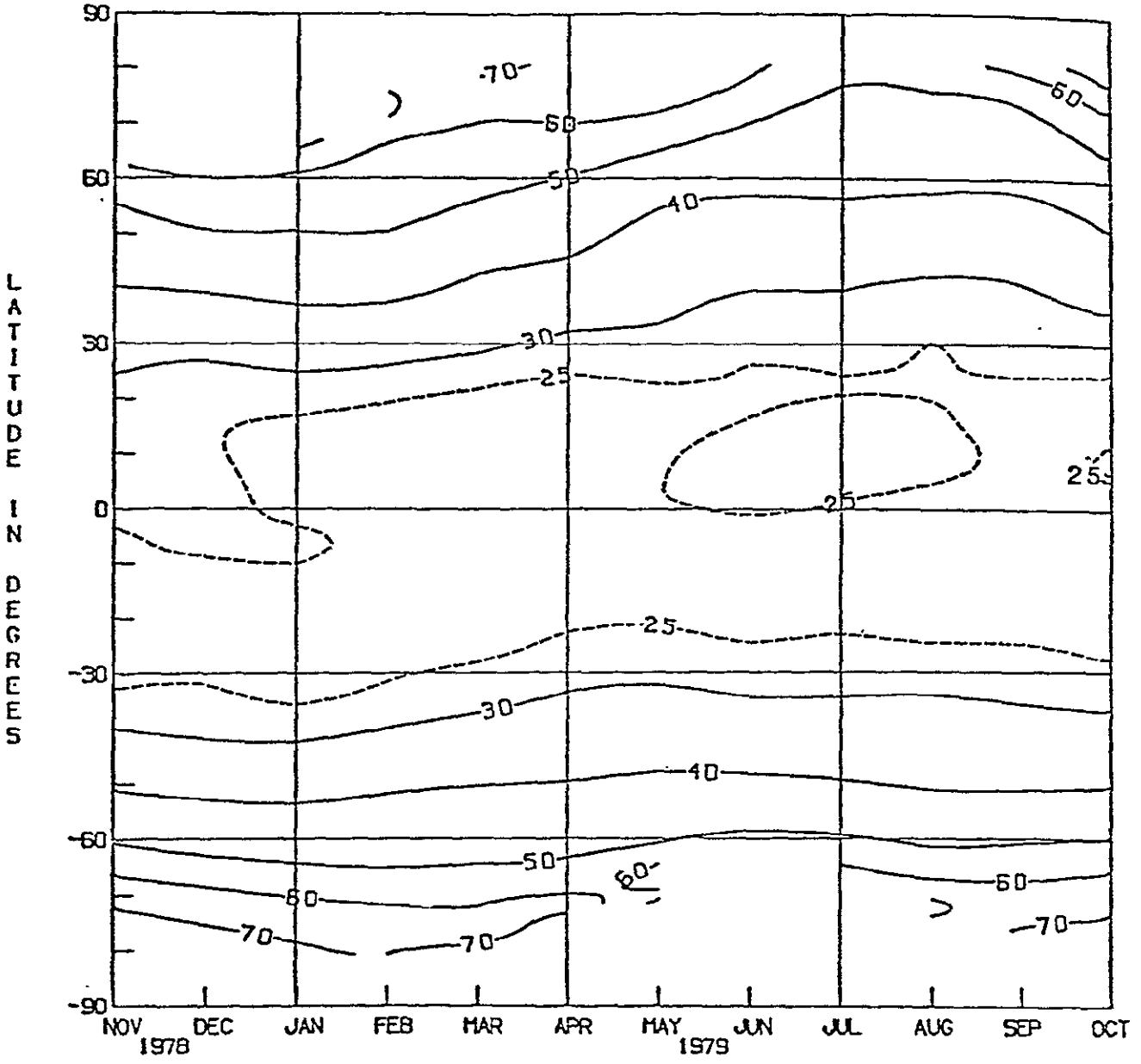

FIGURE 3(a): Time-latitude cross-section for the Albedo derived from the ERB WFOV instrument.

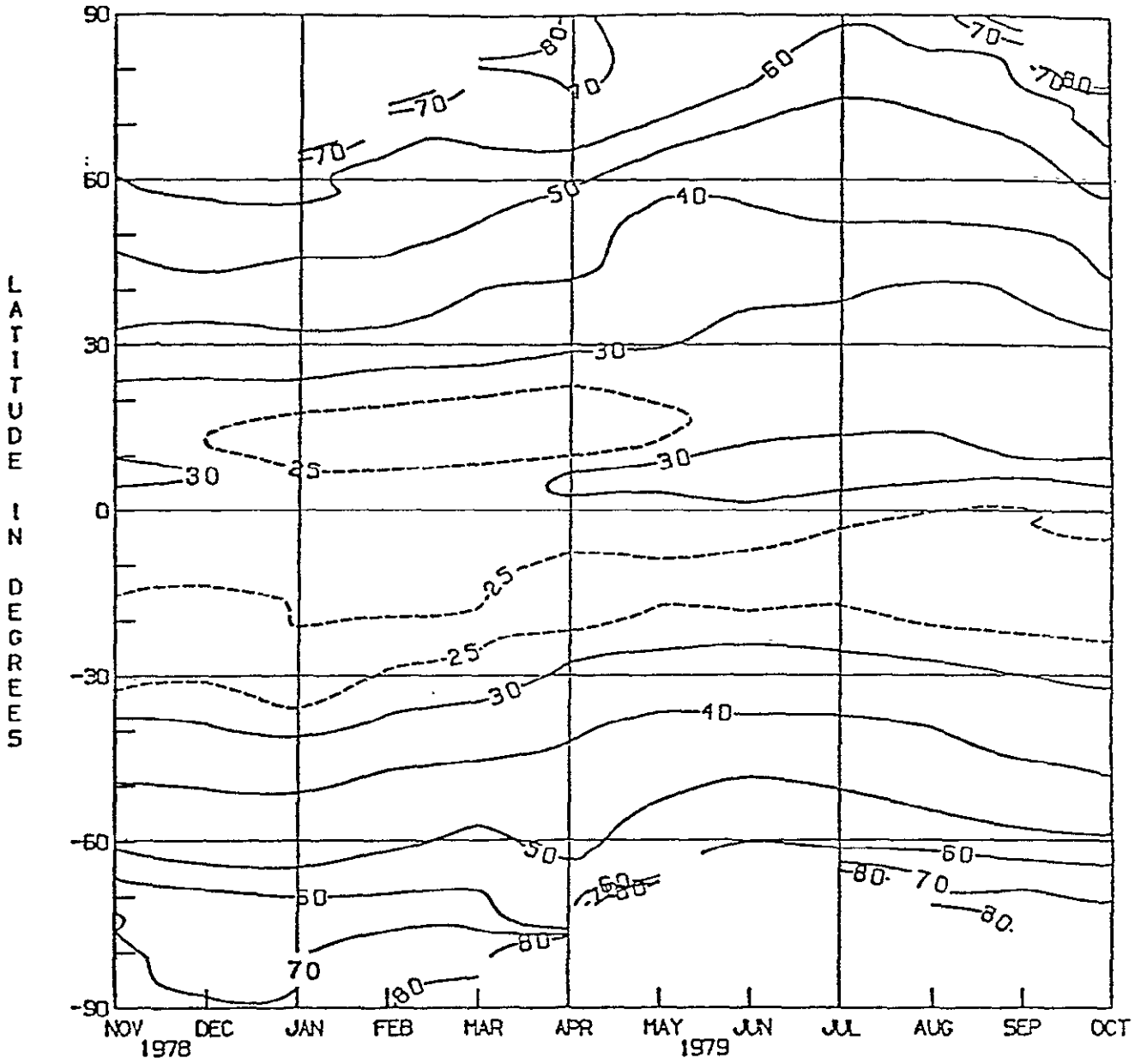

FIGURE 3(b): Time-latitude cross-section for the Albedo derived from the ERB NFOV instrument.

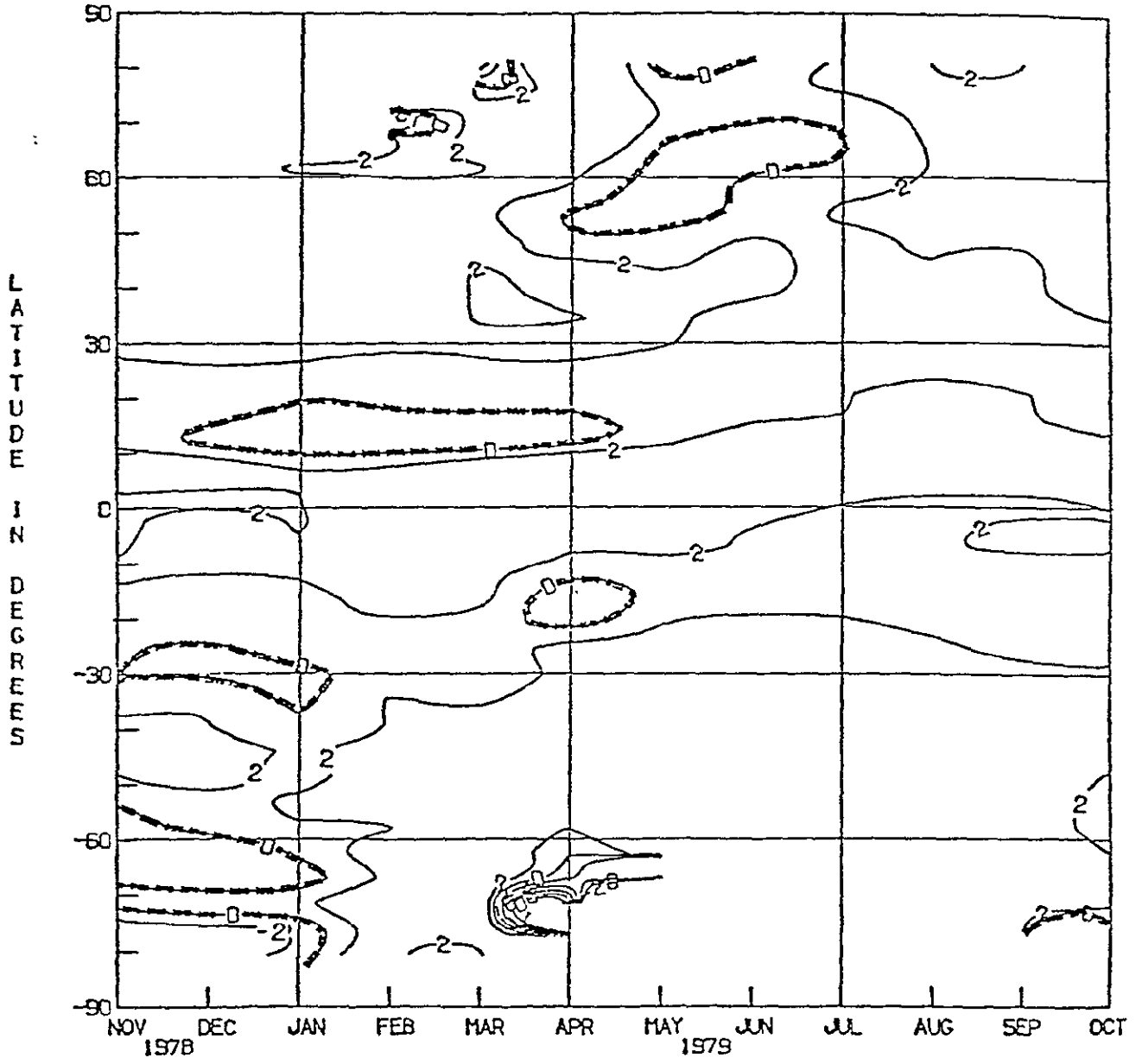

FIGURE 3(c): Time-latitude cross-section for the Albedo differences (NFOV-WFOV).

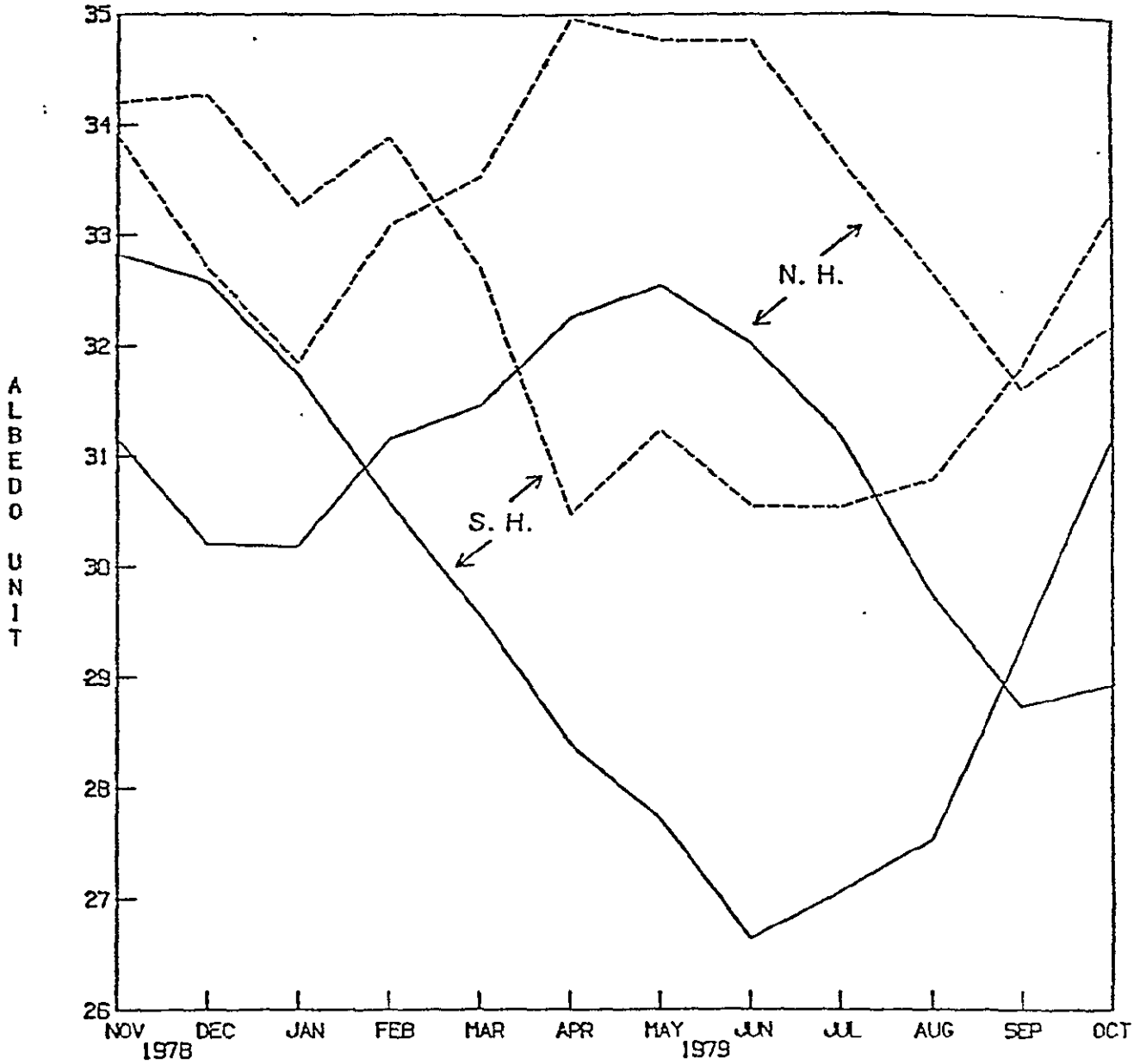

FIGURE 4(a): Northern and Southern hemispherical averages of the monthly mean albedo versus time. Solid curves are for WFOV and dashed curves are for NFOV.

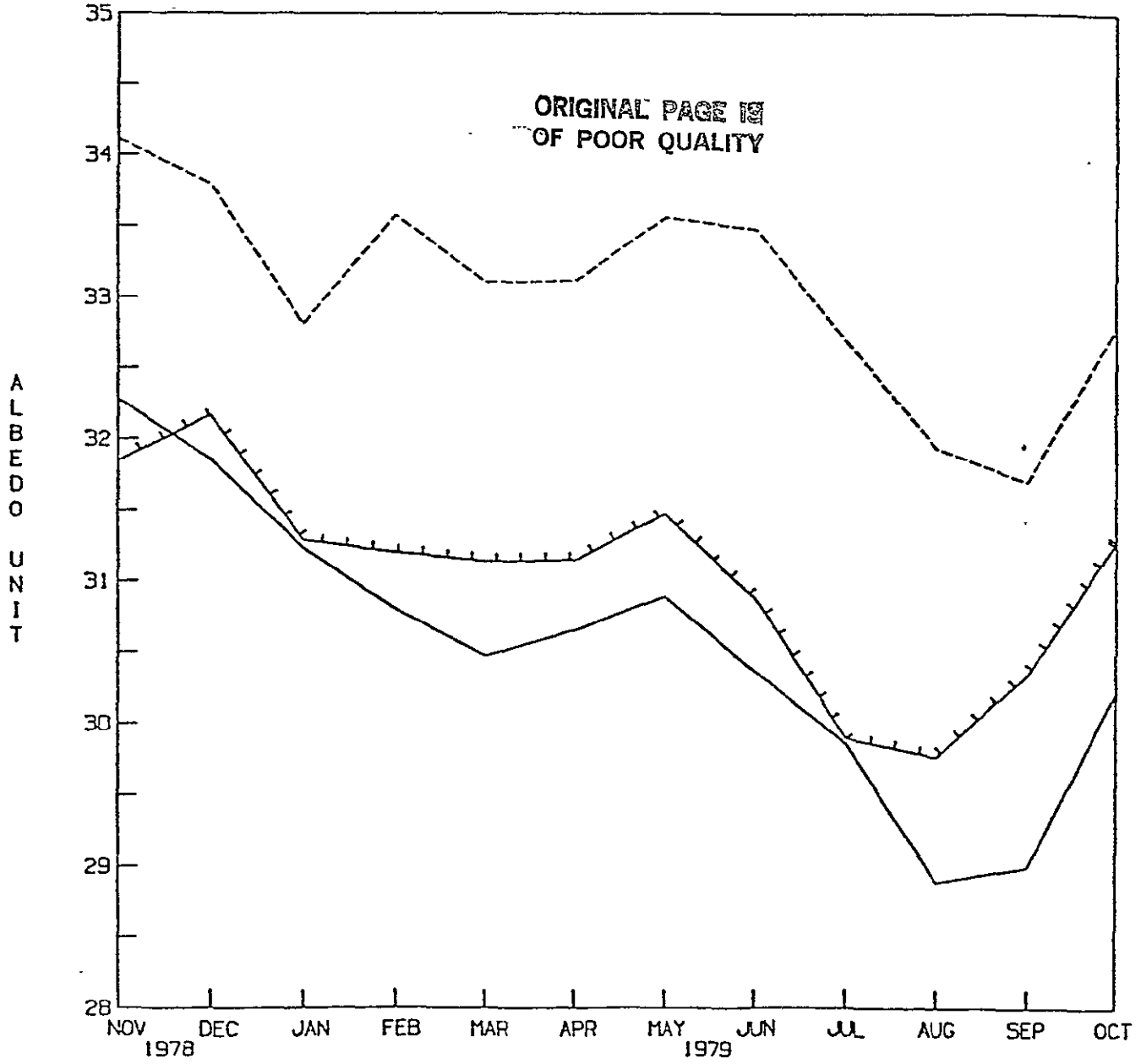

FIGURE 4(b): Global averages of the monthly mean albedos versus time. Solid curve is WFOV, dashed curve is NFOV, and ticked curve is the average from first two years of Nimbus-6 ERB WFOV.

C-2

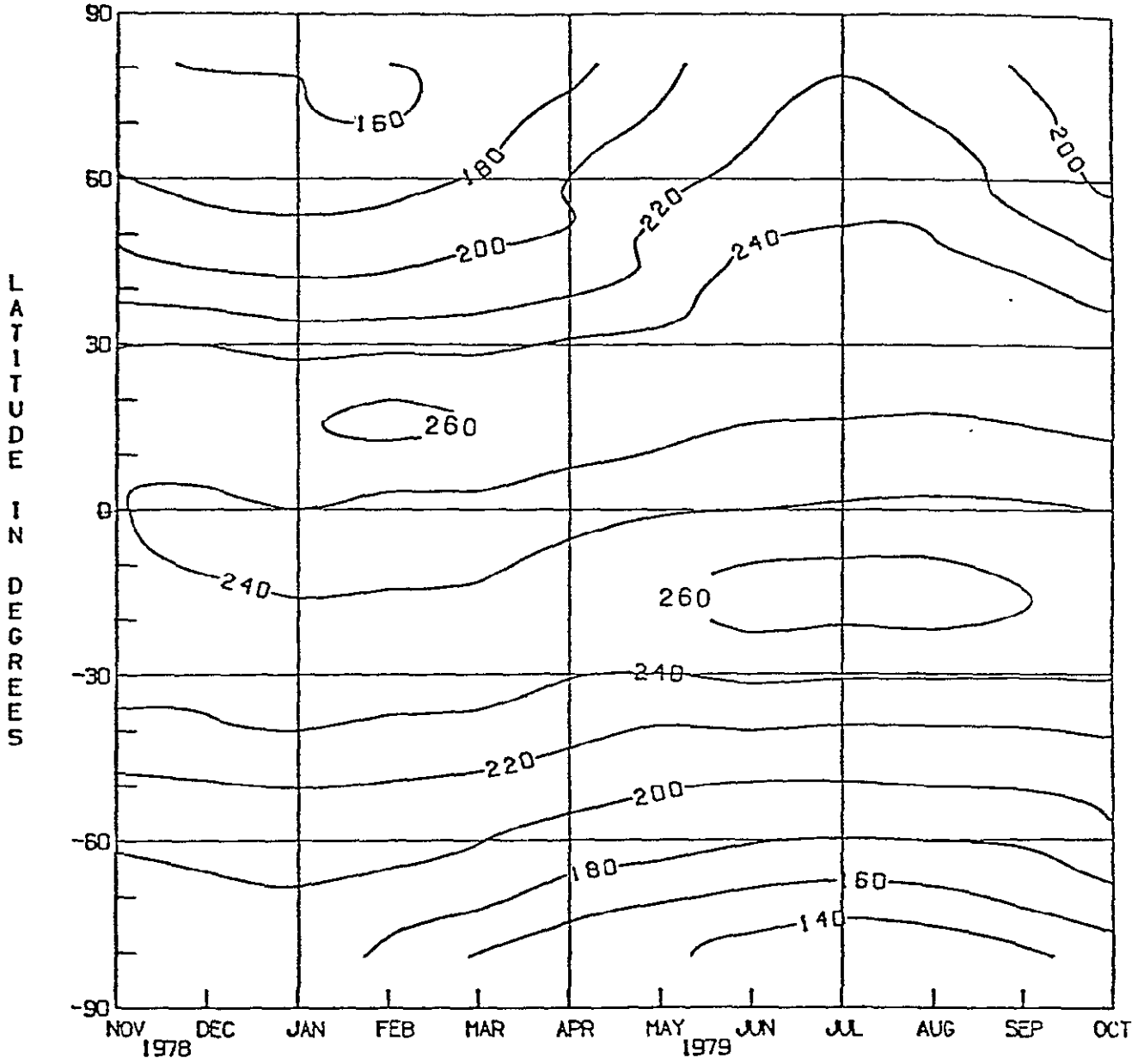

FIGURE 5(a): Time-latitude cross-section for the outgoing Average Longwave Flux derived from the ERB WFOV instrument.

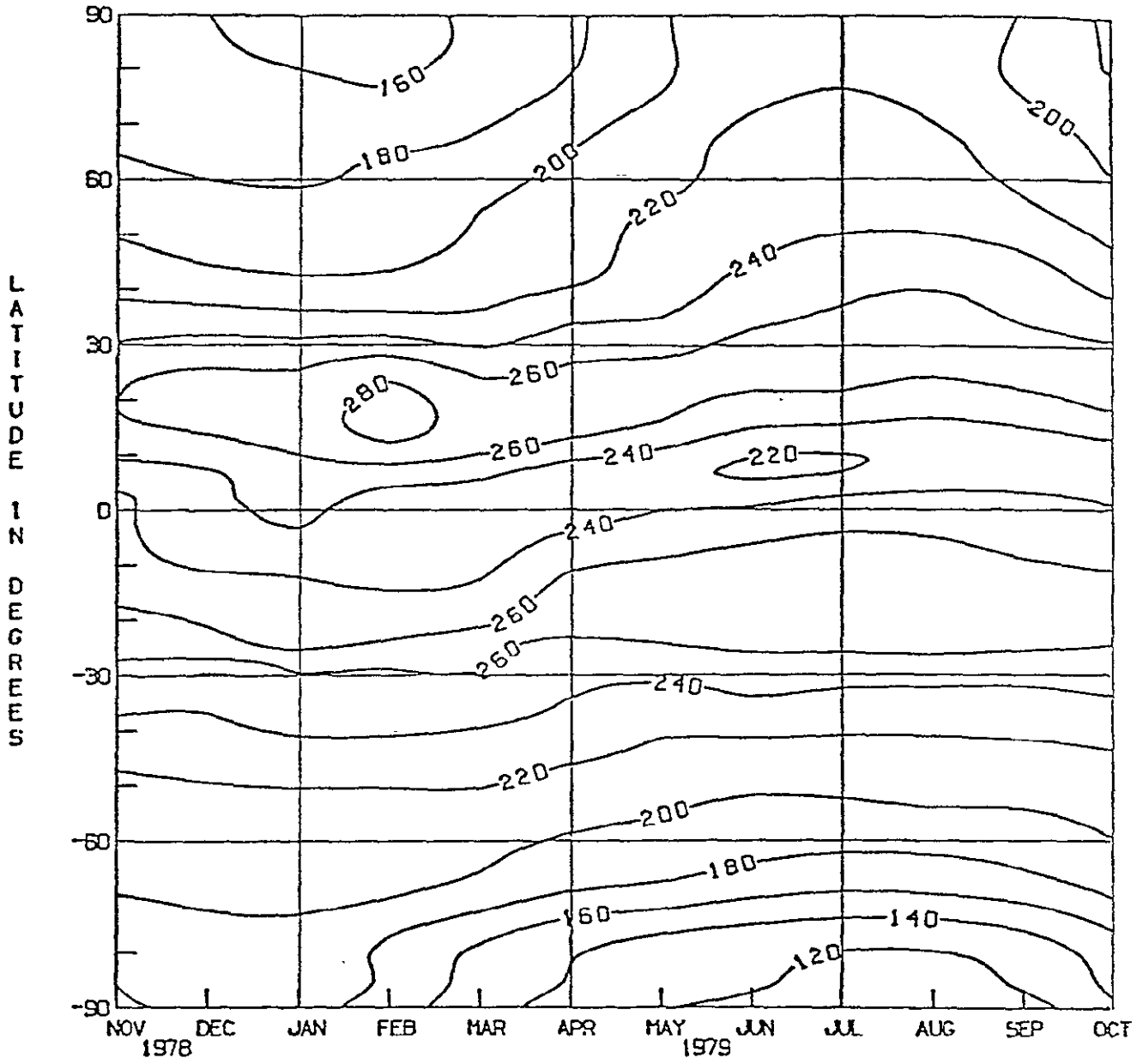

FIGURE 5(b): Time-latitude cross-section for the outgoing Average Longwave Flux derived from the ERB NFOV instrument.

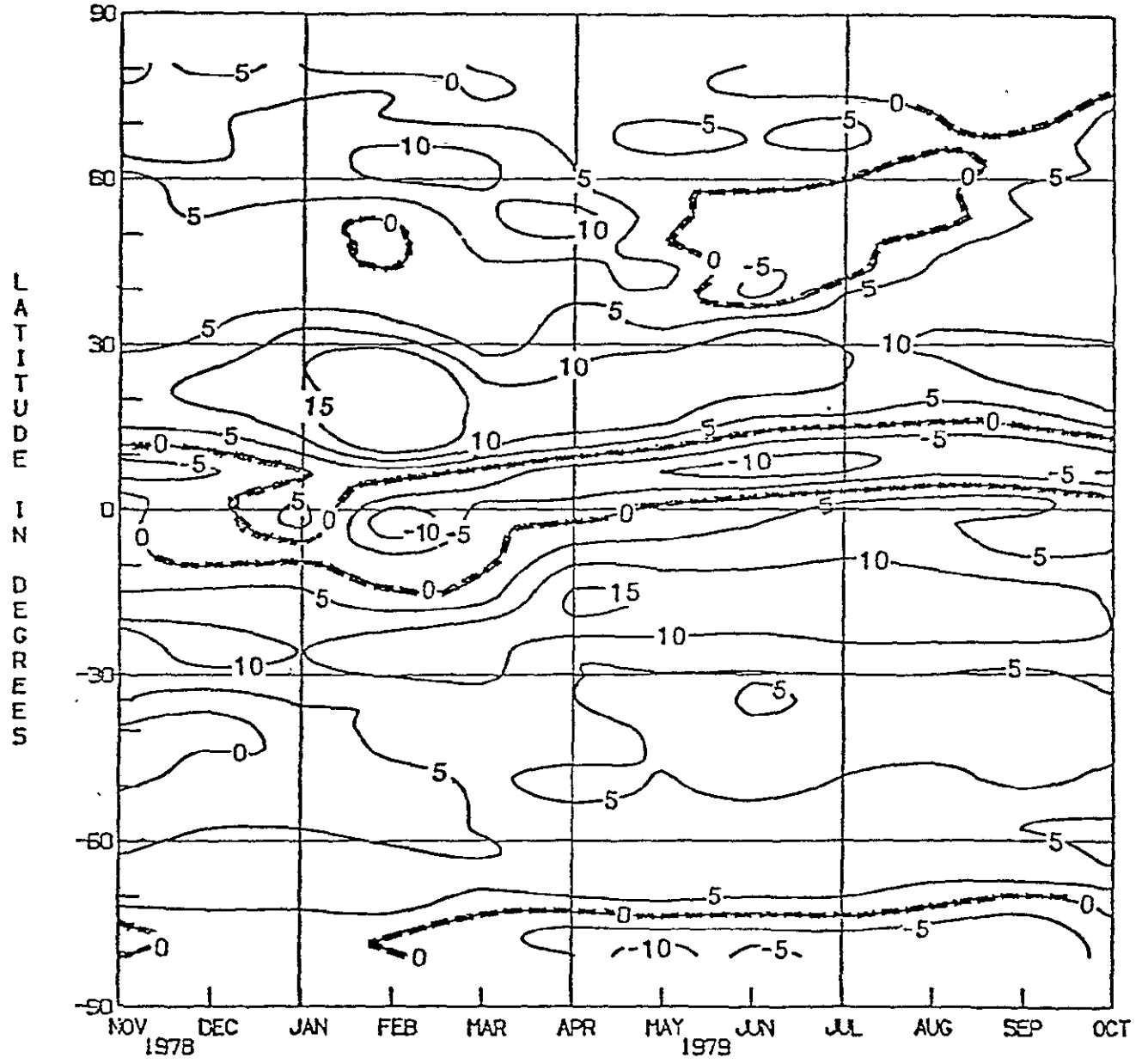

FIGURE 5(c): Time-latitude cross-section for the outgoing Longwave Flux differences (NFOV-WFOV).

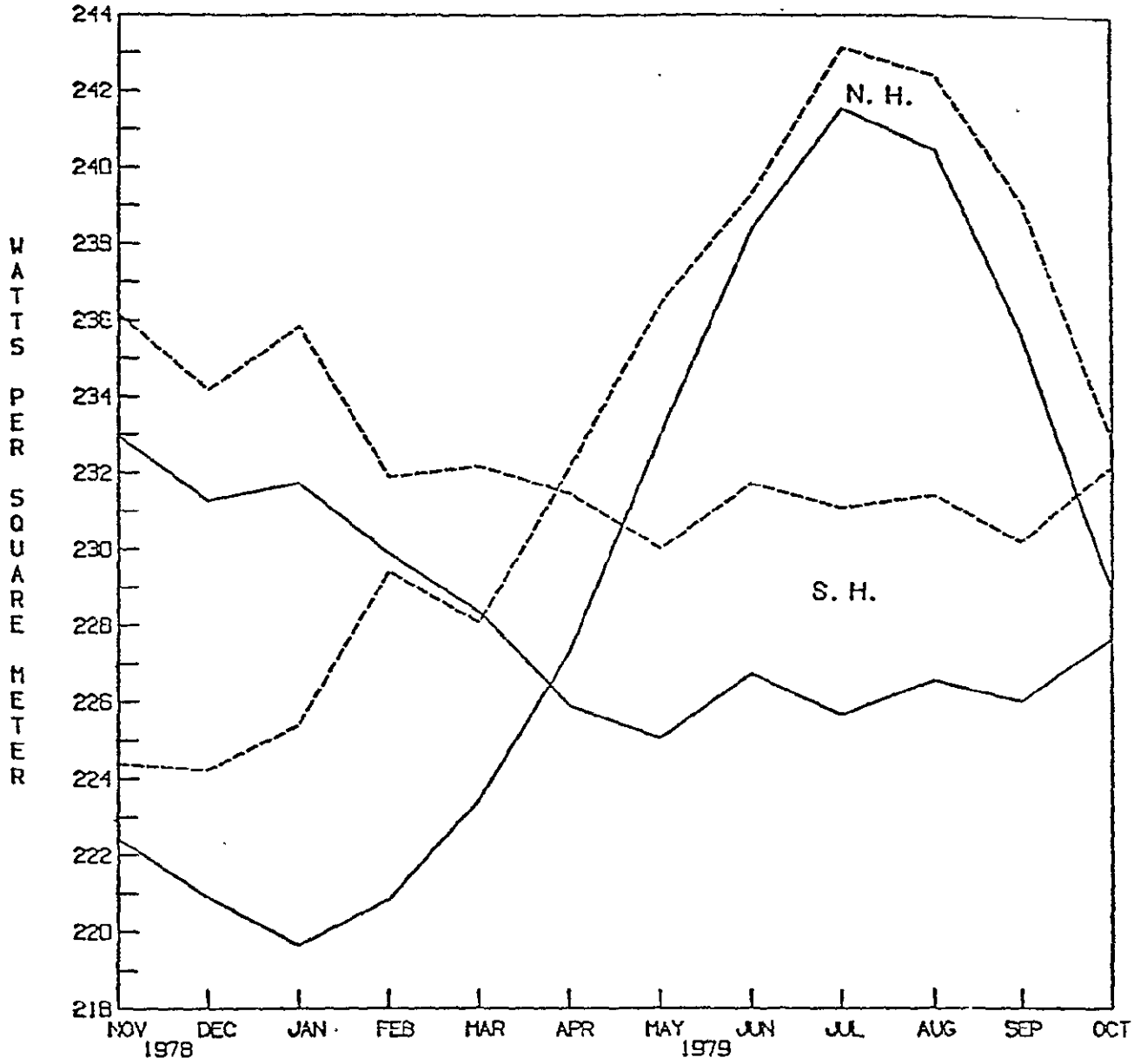

FIGURE 6(a): Northern and Southern hemispherical averages of the monthly mean outgoing flux. Solid curves are for WFOV and dashed curves are for NFOV.

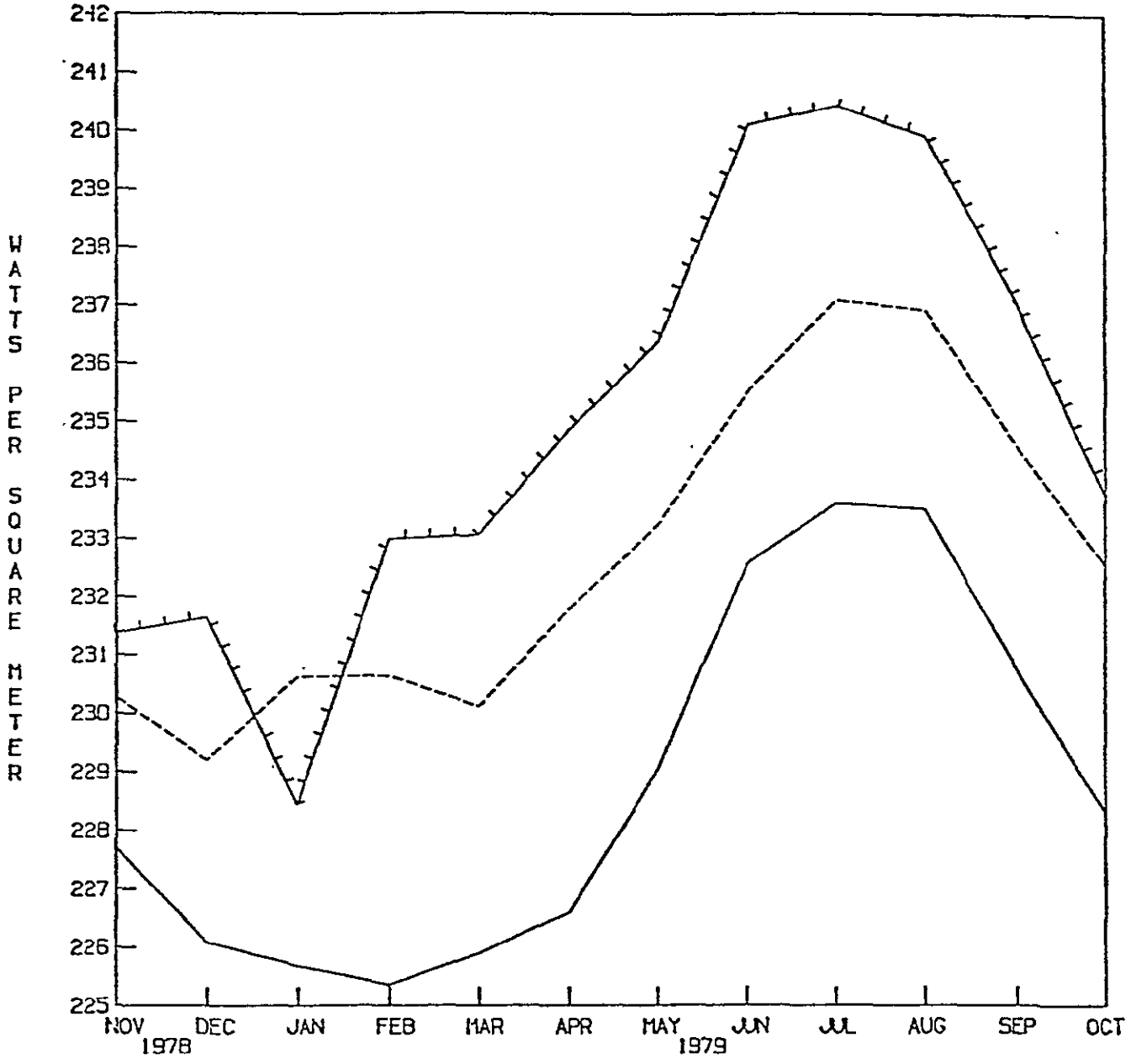

FIGURE 6(b): Global averages of the monthly mean outgoing Longwave Flux. Solid curve is WFOV, dashed curve is NFOV, and ticked curve is the average for first two years of Nimbus-6 ERB WFOV.

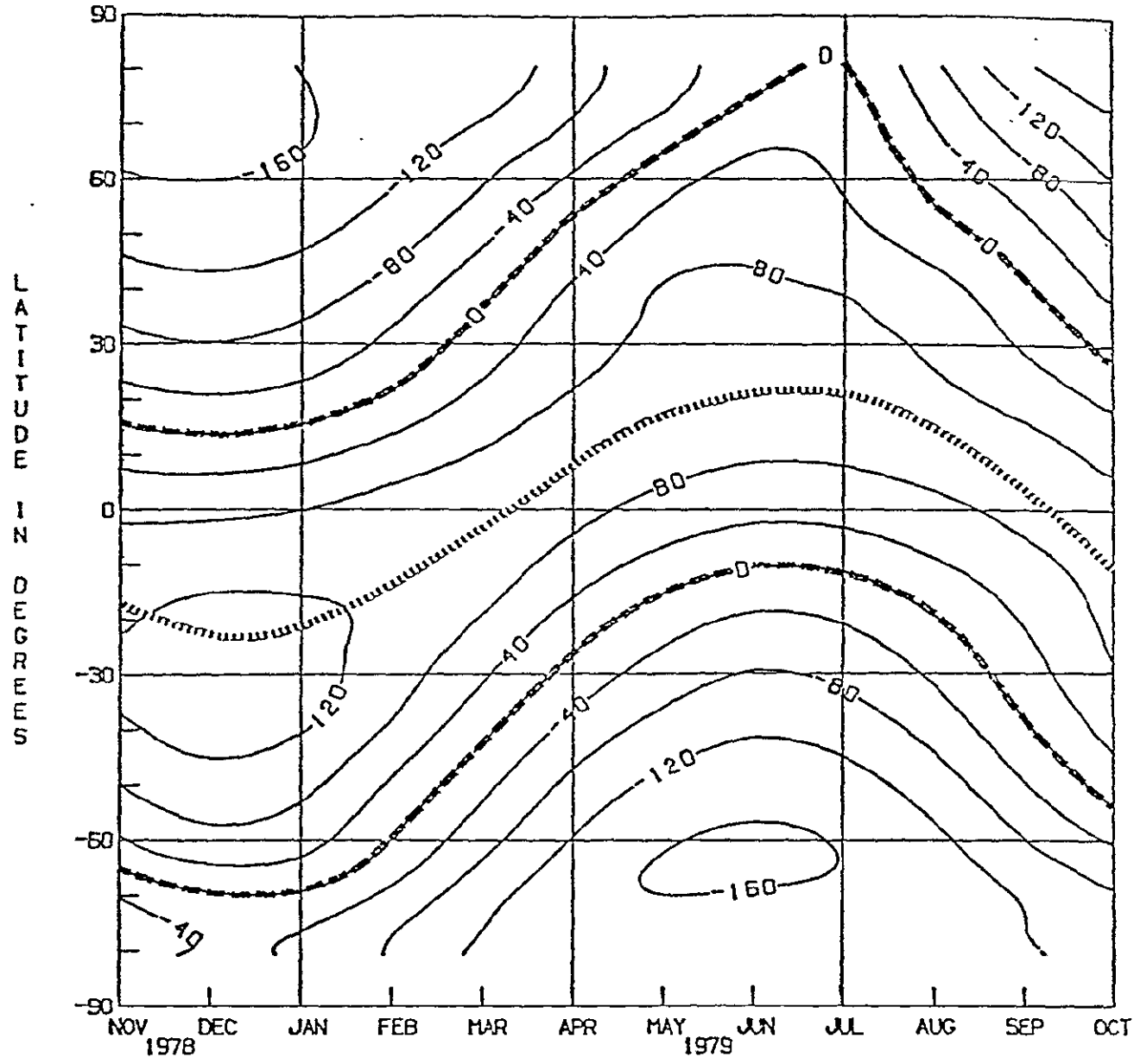

FIGURE 7(a): Time-latitude cross-section for the Net Radiation Flux derived from the ERB WFOV instrument. Light dashed curve is the solar declination.

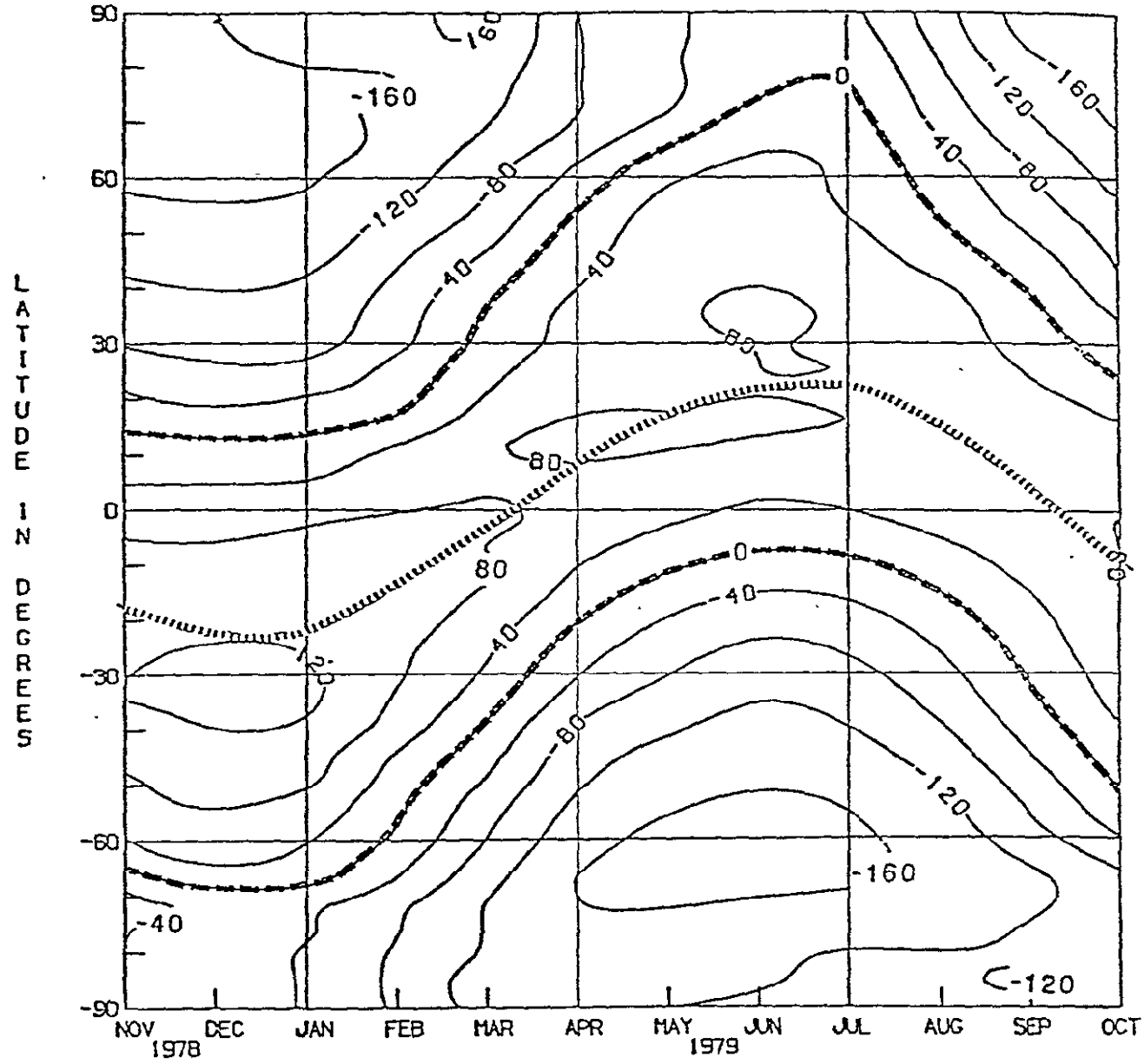

FIGURE 7(b): Time-latitude cross-section for the Net Radiation Flux derived from the ERB NFOV instrument. Light dashed curve is the solar declination.

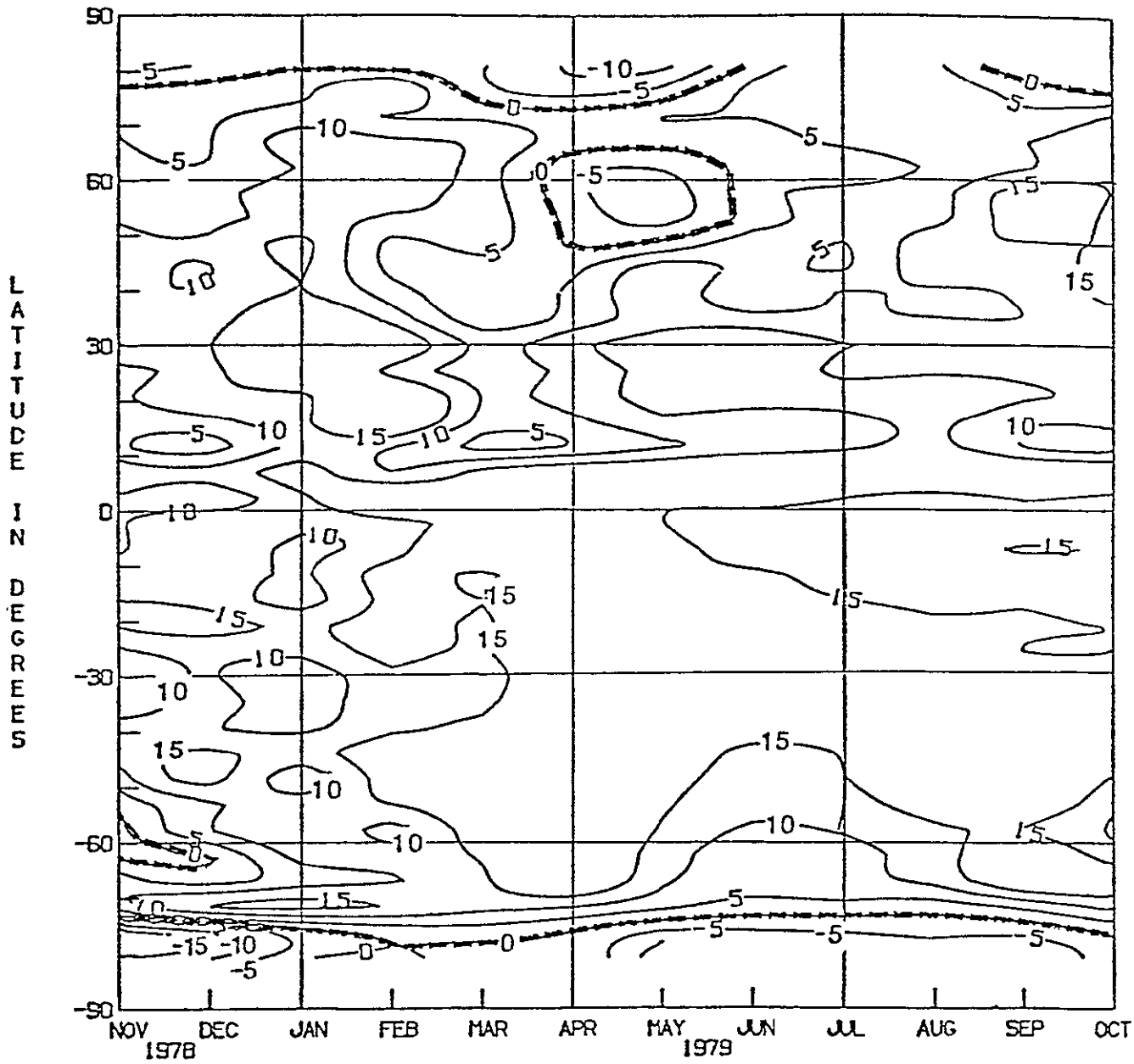

FIGURE 7(c): Time-latitude cross-section for the Net Radiation Flux differences WFOV-NFOV.

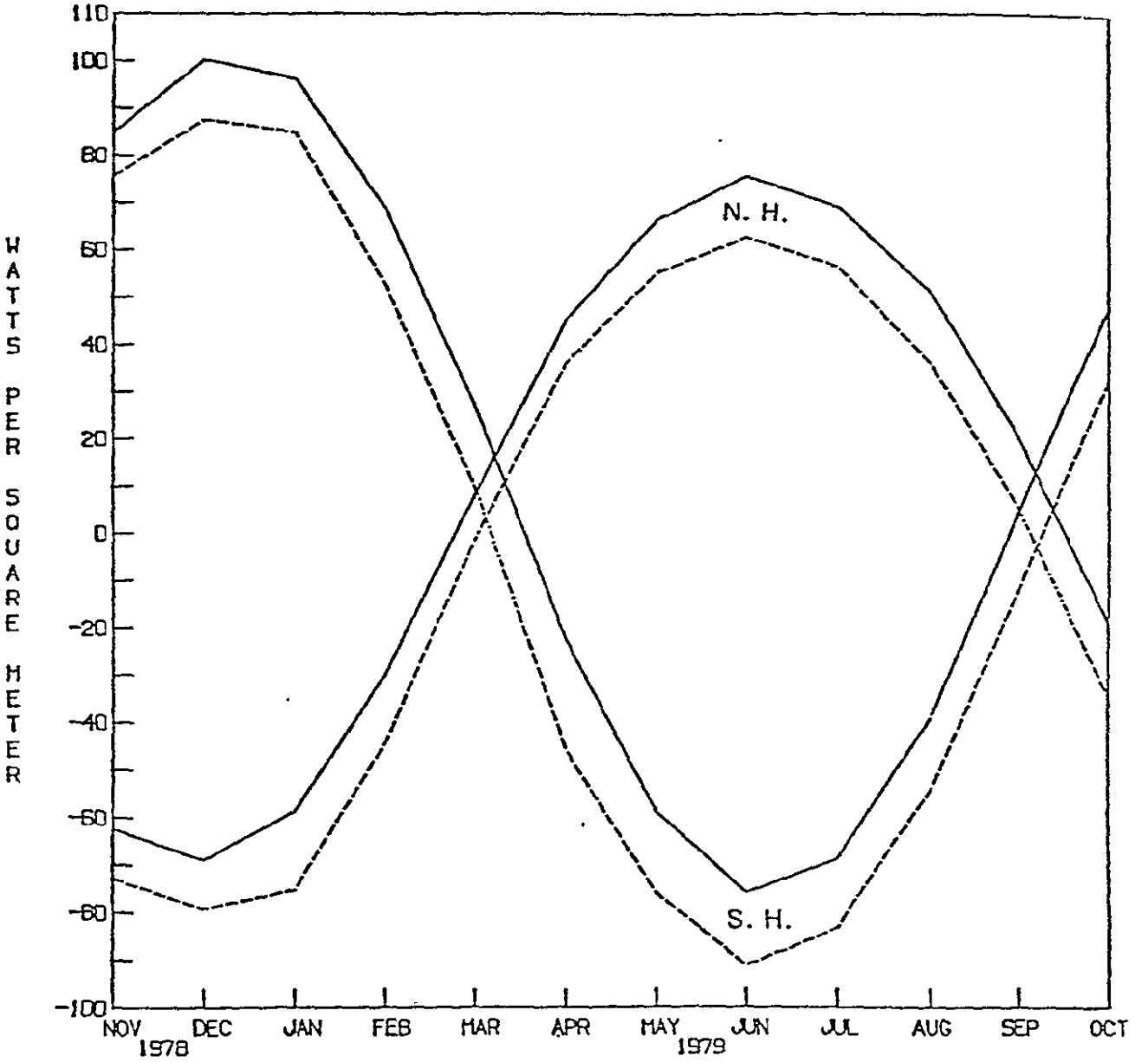

FIGURE 8(a): Northern and Southern hemispherical average of the monthly mean Net Radiation Flux. Solid curves are for WFOV and dashed curves are for NFOV.

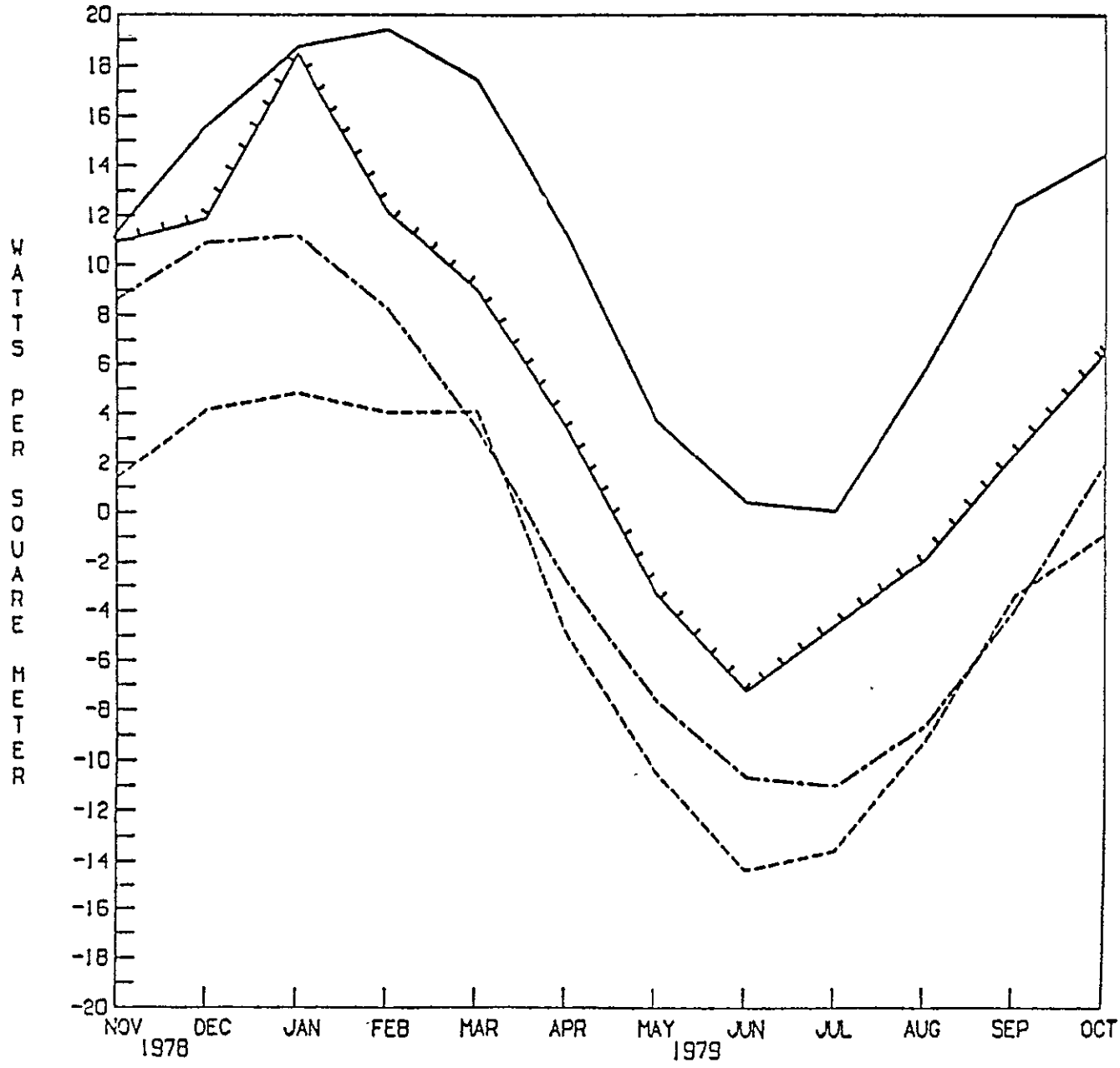

FIGURE 8(b): Global average of the monthly mean Net Radiation Flux. Solid curve is WFOV, dashed curve is NFOV, and ticked curve is the average from first two years of Nimbus-6 ERB WFOV. Deviation of the global average of the solar insolation from its annual mean is shown as the curve with long and short dashes.

ACKNOWLEDGEMENTS

The authors wish to acknowledge Maria Y.H. Shen from Systems and Applied Sciences Corporation for developing the time dependent plots, Regina L. Woodard and Carroll Maunder from the Atmospheric Sciences Branch of the National Environmental Satellite Data and Information Service for typing the manuscript.

REFERENCES

Campbell, G.G. and T.H. Vonder Haar: An Analysis of Two Years of Nimbus-6 Radiation Budget Measurements, Atmospheric Science Paper No. 320, Colorado State University, Ft. Collins, CO, 1980

Ellis, J. and T.H. Vonder Haar: Zonal Average Earth Radiation Budget Measurements from Satellites for Climate Studies, Atmospheric Science Paper No. 240, Colorado State University, Ft. Collins, CO, 1976

Gruber, A. and J.S. Winston: Earth-Atmosphere Radiative Heating Based on NOAA Scanning Radiometer Measurements, Bull. Amer. Meteor. Soc., vol. 59, pp. 1570-1573, 1978

Jacobowitz, H., L.L. Stowe and J.R. Hickey: The Nimbus-7 User's Guide, NASA/Goddard Space Flight Center, Greenbelt, MD, pp. 33-69, 1978

Jacobowitz, H., W.L. Smith, H.B. Howell, F.W. Nagle and J.R. Hickey: The First 18 Months of Planetary Radiation Budget Measurements from the Nimbus-6 ERB Experiment, J. Atmos. Sci., vol. 36, pp. 501-507, 1979

Kyle, H.L., R.H. Maschhoff, F.B. House, P.E. Ardanuy, J.R. Hickey and H. Jacobowitz: Proposed New In-Flight Calibration Adjustment of the Nimbus-6 and -7 Earth Radiation Budget Wide Field-of-View Radiometer (submitted to J.G.R. for special Nimbus-7 issue), 1983

Ohring, G. and A. Gruber: Satellite Radiation Observations and Climate Theory, Advances in Geophysics, vol. 25, pp. 237-301, 1983

Stowe, L.L., S. Vermury and H. Jacobowitz: Sample Size and Scene Identification (Cloud) Effect on Albedo (submitted to J.G.R. for special Nimbus-7 issue), 1983

Taylor, V.R. and L.L. Stowe: Reflectance Characteristics of Uniform Earth and Cloud Surface Derived from Nimbus-7 ERB (submitted to J.G.R. for special Nimbus-7 issue), 1983

ERB EXPERIMENT TEAM MEMBERS

Dr. Albert Arking
NASA/Goddard Space Flight Center
Code
Greenbelt, MD 20771

Dr. Garrett Campbell
Department of Atmospheric Science
Colorado State University
Fort Collins, Colorado 80523

Mr. John R. Hickey
EPPLEY Laboratory, Inc.
12 Sheffield Avenue
Newport, RI 02840

Dr. Frederick B. House
Department of Physics and Atmospheric Science
Drexel University
32nd and Chestnut Streets
Philadelphia, PA 19104

Dr. Andrew Ingersoll
Division of Geological and Planetary Sciences
California Institute of Technology
Pasadena, CA 91125

Dr. Herbert Jacobowitz (Team Leader)
NOAA/National Environmental Satellite Data
and Information Service
Washington, D.C. 20233

Mr. Robert Maschhoff
Gulton Data Systems Division
Albuquerque, NM 87190

Dr. G. Louis Smith
NASA/Langley Research Center
Mail Stop
Hampton, VA 23665

Dr. Larry R. Stowe
NOAA/National Environmental Satellite Data
and Information Service
Washington, D.C. 20233

Dr. Thomas H. Vonder Haar
Department of Atmospheric Science
Colorado State University
Fort Collins, CO 80523

SECTION 3. SCIENCE QUALITY CONTROL REPORT

3.1 OBJECTIVE OF SCIENCE QUALITY CONTROL

Before the Nimbus-7 ERB climate product data sets were archived for use by the scientific community, two levels of validation were performed by the Nimbus Experiment Team (NET). First, the NET validated the scientific processing algorithms employed to produce the data sets. This step was completed early in 1982. Once the algorithms were validated, the data were scientifically validated to assure that it is physically reasonable and useful for scientific research. This second validation step was the objective of the Science Quality Control task.

The approach employed in the Science Quality Control task was to establish criteria by which the climate product data sets could be tested for reasonableness and scientific validity. These criteria were then used in the analysis of each monthly MATRIX tape. An important function of Science Quality Control is the identification, definition, and categorization of the exceptions to these criteria. This document will provide that function. All known problems in the MATRIX data set will be discussed here. Known problems in the MAT Level I data (used as input data to the MATRIX processing) are briefly described in the next subsection. Discussions of the problems found in the Science QC Analysis of the MATRIX follow in the other sections of this document.

3.2 SUMMARY OF KNOWN PROBLEMS FROM THE MAT

In this subsection, several problems inherent in the Level I MAT data set are discussed. These problems were not screened from MATRIX processing. Users of the MATRIX data set must consider these problems for their possible influence on the scientific use of the data.

For a more detailed discussion of the scientific quality of MAT data, see Reference 1, the MAT Data User's Guide.

3.2.1 Degradation of Channel 13 and Channel 14

The Wide Field of View (WFOV) Channels 13 and 14 have been shown to degrade with time. Channel 13 has the more significant degradation with a rate of about 5% over the first year. Degradation of Channel 14 has been shown to be less than 1% (see Reference 1). Among the reasons given for this degradation are: (1) thin film deposition on the ERB instrument optical surfaces, and (2) radiation damage (aging) of the instrument optics.

TABLE 3-1.

ERB World Grid Latitude Bands

Initial data processing in the ERB MATRIX program involves sorting the ERB measurements as a function of geographical areas. To accomplish this, the earth has been divided into 2070 target areas, each about 500 Km square. The target area range and latitude limits are given below:

		LATITUDE LIMITS	
BAND	TARGET AREA RANGE	LOWER LIMIT	UPPER LIMIT
1	1 - 3	-90.0°	-85.5°
2	4 - 12	-85.5	-81.0
3	13 - 28	-81.0	-76.5
4	29 - 48	-76.5	-72.0
5	49 - 78	-72.0	-67.5
6	79 - 114	-67.5	-63.0
7	115 - 154	-63.0	-58.5
8	155 - 199	-58.5	-54.0
9	200 - 247	-54.0	-49.5
10	248 - 307	-49.5	-45.0
11	308 - 367	-45.0	-40.5
12	368 - 427	-40.5	-36.0
13	428 - 499	-36.0	-31.5
14	500 - 571	-31.5	-27.0
15	572 - 643	-27.0	-22.5
16	644 - 715	-22.5	-18.0
17	716 - 795	-18.0	-13.5
18	796 - 875	-13.5	- 9.0
19	876 - 955	- 9.0	- 4.5
20	956 - 1035	- 4.5	0.0
21	1036 - 1115	0.0	4.5
22	1116 - 1195	4.5	9.0
23	1196 - 1275	9.0	13.5
24	1276 - 1355	13.5	18.0
25	1356 - 1427	18.0	22.5
26	1428 - 1499	22.5	27.0
27	1500 - 1571	27.0	31.5
28	1572 - 1643	31.5	36.0
29	1644 - 1703	36.0	40.5
30	1704 - 1763	40.5	45.0
31	1764 - 1823	45.0	49.5
32	1824 - 1871	49.5	54.0
33	1872 - 1916	54.0	58.5
34	1917 - 1956	58.5	63.0
35	1957 - 1992	63.0	67.5
36	1993 - 2022	67.5	72.0
37	2023 - 2042	72.0	76.5
38	2043 - 2058	76.5	81.0
39	2059 - 2067	81.0	85.5
40	2068 - 2070	85.5	90.0

TABLE 3-2.

ERB Parameters

Parameter Number	Description
1	Number of WFOV observations for which center of Channel Sub FOV falls within a particular target area during AN.
2	Number of WFOV observations for which center of Channel Sub FOV falls within a particular target area during DN.
3	LW Flux WFOV-AN is (CH12 - CH13) if Ch13 > 0 and Max. Ref. Energy(P5) > 0, otherwise is Ch12 during AN. Computed on a daily and monthly basis.
4	LW Flux WFOV-DN is (CH12 - CH13) if Ch13 > 0 and Max. Ref. Energy(P5) > 0, otherwise is CH12 during DN. Computed on a daily and monthly basis.
5	Maximum Reflected Energy (.2-4 μm) for WFOV-AN is computed daily and monthly for world grids. If FOV is in AN, compute irradiance CH10C x scaling factor.
6	Maximum Reflected Energy (.2-4 μm) for WFOV-DN is computed daily and monthly for world grids if FOV is in DN. Similar to Parameter 5.
7	Maximum Reflected Energy (.7-3 μm) for WFOV-AN is computed daily. If FOV is in AN, compute irradiance CH5 x scaling factor.
8	Maximum Reflected Energy (.7-3 μm) for WFOV-DN is computed daily. If FOV is in AN, compute irradiance CH5 x scaling factor. Similar to Parameter 7.

TABLE 3-2.

ERB Parameters

(Continued)

Parameter Number	Description
9	Reflected Energy (.2-4 μm) from WFOV observations - AN. If FOV is in AN for the TA identified, CH13 irradiance accumulated and divided by number of observations gives daily Reflected Energy. Sum of daily values divided by number of days gives monthly Reflected Energy.
10	Reflected Energy (.2-4 μm) from WFOV observations - DN. Same as in Parameter 9, except FOV is in DN.
11	Reflected Energy (.7-3 μm) from WFOV observations - AN. Same as in Parameter 9, except processes CH14 irradiance.
12	Reflected Energy (.7-3 μm) from WFOV observations - DN. Same as in Parameter 11, except FOV is in DN.
13	Earth Albedo (.2-4 μm) from WFOV observations. Daily Albedo = Daily Parameter 9/Daily Parameter 5. $\text{Monthly Albedo} = \frac{\Sigma(\text{Daily Parm 36} \times \text{Daily Parm 13} \times F)}{\Sigma\text{Daily Parm 36}}$ SZA correction F is to correct instantaneous Albedo to mean daily Albedo. This is not calculated if Parameter 1 = 0 or Parameter 5 = 0 or Parameter 36 < 4 W/m^2.

TABLE 3-2.

ERB Parameters

(Continued)

Parameter Number	Description
14	Earth Albedo (.2-.7 μm) from WFOV observations. Daily Albedo = $\frac{\text{Daily Parameter 9 - Daily Parameter 11}}{\text{Daily Parameter 5 - Daily Parameter 7}}$ Monthly Albedo = $\frac{\Sigma\ (\text{Daily Parm 36 x Daily Parm 14 x F}}{\Sigma\ \text{Daily Parm 36}}$
15	Earth Albedo (.7-3 μm) from WFOV observations. Daily Albedo = Daily Parameter 11/Daily Parameter 7 Monthly Albedo = $\frac{\Sigma\ (\text{Daily Parm 36 x Daily Parm 15 x F})}{\Sigma\ \text{Daily Parm 36}}$
16	Net Radiation (N) from WFOV observations is computed on daily, cyclic, and monthly basis. Daily: N = (1 - A x F)AVINS - LWF; where A = P13, AVINS = P36, LWF = (P3 + P4)/2 when both P3 and P4 are present. If P3 is a filled value LWF = P4 and if P4 is a filled value LWF = P3. Cyclic: Cyclic N = Σ Daily P16/Cyclic P26. Monthly: Monthly N = Monthly P36 (1 - Monthly P13) - Monthly P28.

TABLE 3-2.

ERB Parameters

(Continued)

Parameter Number	Description
17	SW Data Population of NFOV observations - AN. For daily value it is the number of observations which pass all specified screening tests. For monthly value it is the number of observation days.
18	SW Data Population of NFOV observations - DN. Same as in Parameter 17, except FOV is in DN.
19	LW Flux from NFOV observations - AN. $\text{Daily Flux} = \frac{\Sigma \text{ day } \phi 19 + \phi 20 + \phi 21 + \phi 22}{\text{Total Number of Observations}}$ where 19 - 22 are radiances from CH19 thru 22, ϕ is LW Angular Dependence Model function $\text{Monthly Flux} = \frac{\Sigma \text{ Daily Parm 19}}{\text{No. of Days}}$
20	LW Flux from NFOV observations - DN. Same as in Parameter 19, except the FOV is in DN.

TABLE 3-2.

ERB Parameters

(Continued)

Parameter Number	Description
21	LW Terrestrial Flux (F_{WA}) NFOV Weighted average of AN and DN data.

$$\text{Daily } F_{WA} = \frac{P19 \times D_{AN} + P20 \times D_{DN}}{D_{AN} + D_{DN}}$$

where D is daylight hours based on latitude.

Monthly F_{WA} = Σ Daily P21/No. of Days.

22 Earth Albedo from NFOV Observations:

Daily: i) Daily Reflected Energy (DRE) from Channels 15 -18 radiances is computed according to:

$$DRE = \frac{\Sigma day\ \Psi 15 + \Psi 16 + \Psi 17 + \Psi 18}{\text{Number of Observations}}$$

ii) Calculate Albedo (A) using the equation:

$$A = \frac{DRE}{AVINS\ (P36)}$$

Monthly: ΣDaily DRE/ ΣDaily P36

TABLE 3-2.

ERB Parameters

(Continued)

Parameter Number	Description
23	Net Radiation (N) from NFOV observations. Daily: $N = AVINS(1 - Albedo) - LW\ Flux$ $= P36(1 - P22) - P21$ Cyclic: $N = \Sigma$ Daily P23/Cyclic P27 Monthly: $N = \frac{\Sigma \text{ Daily P23}}{\text{No. of Days}}$
24	LW Data Population of NFOV observations - AN. Daily: Number of Observations for each target area. Monthly: Number of observation days.
25	LW Data Population of NFOV observations - DN. Same as in Parameter 24, exept spacecraft is in DN.
26	Data Population of Averaged WFOV LW Flux (Parameter 28). Cyclic: Increment by one if daily P16 is a non filled value. Monthly: Increase counter by one if daily P1 and/or daily P2 is a non-zero value.

TABLE 3-2.

ERB Parameters

(Continued)

Parameter Number	Description
27	Data Population of Averaged NFOV LW Flux (Parameter 21). Cyclic: Increment by one if daily P23 is not a filled value. Monthly: Increment by one when both P24 and P25 have non-zero value.
28	Averaged LW Terrestrial Flux from WFOV observations. The monthly average is computed according to the following equation: $Av = \frac{\text{Monthly P3 + Monthly P4}}{2}$ If either monthly P3 or monthly P4 is zero, then the Av = the other.
29	Normalized Dispersion of LW Flux from WFOV observations Calculate: $x = \frac{\text{daily P3 + daily P4}}{\text{mean value of x}}$ $ND = \frac{\text{standard deviation of x}}{\text{mean value of x}}$

TABLE 3-2.

ERB Parameters

(Continued)

Parameter Number	Description
	Alternatively:
	x_1 = ND(P3) = σ (P3)/mean P3
	x_2 = ND(P4) = σ (P4)/mean P4
	$ND = \left[1/2(x_1^2 + x_2^2)\right]^{1/2}$
	where σ is the standard deviation.
30	Normalized Dispersion of Earth Albedo (.2 - 4 μm) from WFOV observations. This is a monthly parameter calculated according to the equation:
	$ND = \frac{\text{Std. Dev. of (daily P13)}}{\text{Mean of (daily P13)}}$
31	Standard deviation of Net Radiaiton from WFOV observations.
32	Normalized Dispersion (ND) of Averaged LW Terrestrial Flux from NFOV observations. This is calculated on a monthly basis using the equation:
	ND = Standard deviation of (daily 21)/Mean of (daily 21)

TABLE 3-2.

ERB Parameters

(Continued)

Parameter Number	Description
33	Normalized dispersion (ND) of Earth Albedo from NFOV observations. This is calculated on a monthly basis using the relation: $ND = \frac{\text{Std. dev. of daily P22}}{\text{Mean of daily P22}}$
34	Standard deviation of Net Radiation from NFOV observations. Calculated for month using daily Parameter 23.
35	Minimum Earth Albedo from NFOV observations from daily Parameter 22.
36	Average Solar Insolation is computed as daily and monthly Parameter. Daily: $AVINS = SOLINS(1,IL) + \frac{180 - LON}{360} \{SOLINS(2,IL) - SOLINS(1, IL)\}$ Monthly: ΣDaily AVINS/No. of days where: AVINS = Ava. Solar Insolation; SOLINS = Solar Insolation; LON = Longitude
37	Earth Albedo (.2 - 4 μm) from WFOV observations <u>without</u> Solar Zenith Angle correction.

TABLE 3-3.

Daily, Cyclic, and Monthly ERB Parameters that are Output

This Table indicates as to which of the ERB Parameters is output for Daily World Grid, cyclic (WG and MAP) and monthly (WG and MAP).

PARAMETER	DAILY WG	CYCLIC WG	CYCLIC MAP	MONTHLY WG	MONTHLY MAP
1	X	-	-	X	X
2	X	-	-	X	X
3	X	-	-	X	X
4	X	-	-	X	X
5	X	-	-	X	-
6	X	-	-	X	-
7	X	-	-	X	-
8	X	-	-	X	-
9	X	-	-	X	-
10	X	-	-	X	-
11	X	-	-	X	-
12	X	-	-	X	-
13	X	-	-	X	X
14	X	-	-	X	X
15	X	-	-	X	X
37	-	-	-	X	X
16	X	X	X	X	X
17	X	-	-	X	X
18	X	-	-	X	-
19	X	-	-	X	X
20	X	-	-	X	X
21	X	-	-	X	X
22	X	-	-	X	X
23	X	X	-	X	X
24	X	-	-	X	X
25	X	-	-	X	X
26	-	X	-	X	X
27	-	X	-	X	X
28	-	-	-	X	X
29	-	-	-	X	X
30	-	-	-	X	X
31	-	-	-	X	X
32	-	-	-	X	X
33	-	-	-	X	X
34	-	-	-	X	X
35	-	-	-	X	X
36	X	-	-	X	-

X = YES
- = NOT OUTPUT

A recalibration of the Channel 13 irradiances was performed by the application of the Channel 13 Calibration Adjustment Table (CAT). The major goal of the CAT was to correct this degradation. However, analysis of the MATRIX albedo parameters for Year-1 indicates that a degradation persists in the Year-1 Channel 13 irradiances after application of the CAT. Degradation effects on the Channel 13 irradiances are further complicated by the fact that the leading and trailing halves of the Channel 13 filter dome apparently degrade at different rates (see References 2 and 3).

3.2.2 Scanner Duty Cycle

The Narrow Field of View (NFOV) scanning telescope was occasionally operated in a mode which differed from the ERB instrument duty cycle. An example of this is a case where the scanner was in SCAN mode for one day, then in NADIR mode for one day, and so forth. Another example is the so-called "LIMS Compromise" where the scanner was set to NADIR mode on the Descending Node portion of each orbit from 80 degrees North Latitude to 27 degrees South Latitude. The "LIMS Compromise" limited the ERB Scanner operations from January 4, 1979 through mid April,1979 (see Appendix A). The effect of these different scanner duty cycles was to cause loss of whole orbits or portions of orbits. This will cause data sampling problems to be induced into the MATRIX data. Daily latitude band averages are severely impacted by loss of orbits. This sampling problem shows up as large fluctuations in the data populations of the affected latitude zones (this will be discussed further in a later section). ERB parameters are averaged on a daily basis for each target area. The monthly average of an ERB parameter is then computed by averaging the target area averages for each data day in the month. When a target area is poorly sampled for a particular day, there is a possibility that the poor sampling will produce a bias in the monthly average. This is a major problem in the Year-1 data set for NFOV LW flux in the months of January and February. In those months, the "LIMS Compromise" was in effect. The Descending Node NFOV LW flux was poorly sampled in target areas in the Northern Hemisphere for most days. Normal levels of sampling in these target areas (on the Descending Node) occurred only for one or two days each month. This resulted in unreliable monthly values of NFOV LW flux for target areas in the Northern Hemisphere (both for Descending Node and for Total LW flux).

3.2.3 ERB Instrument Duty Cycle - Thermal Effects

During Nimbus Year-1, the ERB instrument was operated in a one-day-off, three-day-on duty cycle. This duty cycle was imposed on ERB by considerations of limited spacecraft power. Sometimes the duty cycle was different but the important thing is that periodically the ERB instrument was powered off. When the instrument was turned on, a warmup period followed where the electronics approached an operating temperature. Data taken

during this warmup period is rejected by MATRIX processing (see Reference 4). This rejection is needed because the laboratory calibration of the ERB sensors was performed under steady state (constant temperature) conditions. The calibration equations used to produce the MAT are thus invalid during these warmup periods.

It has been pointed out (ERB Working Group Meeting #43; May 21, 1982; Phillip Ardanuy, Research and Data Systems) that the temperature does not remain stabilized after this warmup period. During periods of changing instrument temperature, the ERB irradiances are also impacted by this error in the calibration equations. Channel 13 is the most strongly affected channel. The indication of error in this case is an apparent drift in the offset of the sensors. The effect is that the measured irradiances show a cyclic behavior that follows the ERB duty cycle. A method has been suggested for removing this effect from the Channel 13 and 14 irradiances. This approach would add a variable offset to these irradiances which forces their value at satellite midnight to be identically zero. This amounts to a recalibration of the sensor for zero input.

3.2.4 Dome Heating Effects on Channel 13 and Channel 14

It has been shown (References 5 and 6) that the Channel 13 and Channel 14 filter domes are radiatively heated and subsequently reradiate onto the sensors. The effect of this reradiation is a variable offset which contaminates the measured irradiances. The laboratory study described in Reference 6 was performed on an ERB prototype instrument set. LW radiaton from the Sun and the scene being viewed were found to produce transient forcing, causing a time-lagged thermal response (offset) in the two sensors. The study reported in References 6 and 7 also found that the two channels showed a transient thermal response to SW heating by the Sun. The SW response is thought to be due to a thermal gradient (thermal wave) due to absorption of energy by the ERB instrument module.

The subject of LW heating can be handled but SW heating though understood qualitatively is quantitatively difficult to remove. SW heating is a problem which needs consideration and revision.

These effects despite their complexities, lend themselves to statistical analysis and accurate modeling based on the results of the studies mentioned above. An approach for recalibrating the MAT irradiances which will remove the effects of these transient thermal offsets has been developed. The approach will use the form of the corrections developed in Reference 4.

A calibration tape (DELMAT) is produced from the MAT irradiances and used in MATRIX processing to recalibrate the Channel 13 and 14 irradiances prior to scientific processing. This calibration approach has been applied in MATRIX production following the data month of May, 1980 (after the NFOV scanner failed).

3.2.5 Channel 18 Failure

A sharp increase in the noise level output by Channel 18 occurred on Day 360 of 1978 (ERB Working Group Meeting #35; March 26, 1982; Michael Fromm, Research and Data Systems). Negative values for Channel 18 radiances occurred both at night and during daytime orbital segments. The NET decided that all Channel 18 data after Orbit 880 (on Day 360) should not be processed by the MATRIX software. There is an indication that this noise problem in Channel 18 may have been due to interference from the stepper drive motor used to drive the NFOV scan head.

3.3 PROBLEMS OBSERVED IN THE MATRIX DATASET

Problems which were observed in the MATRIX data set are listed here and briefly described.

3.3.1 The LIMS Compromise

This problem has been discussed earlier (Subsection 3.2.2). The effect of the LIMS Compromise was to cause poor sampling of the NFOV Descending Node LW flux over the Northern Hemisphere. This means that monthly averages of this parameter for January through March, 1979 have many target areas where only one or two days have contributed to the average. This would tend to make the NFOV LW flux and net radiation parameters invalid for scientific use (over the Northern Hemisphere) for these months.

3.3.2 NFOV Monthly Parameter Inconsistencies

During periods of scanty data the NFOV monthly average LW flux, albedo and net radiation (P21, P22, and P23) do not always form a consistent set which obey the net radiation equation. On a daily basis they do form a consistent set, however the monthly averages are formed separately for each parameter from the daily values. Both LW flux and albedo must be present for a given target area for the daily net radiation to be calculated, however if only the albedo or the LW flux is observed on a particular day it alone will be present. Thus, for data poor months the net radiation for many target areas may have been calculated for only a few days. But albedo and/or LW flux can be present on several additional days.

3.3.3 Calibration-Induced Discontinuity In WFOV Descending Node LW Flux

The application of the Channel 13 Calibration Adjustment Table (CH13CAT) forces agreement between daytime WFOV and NFOV LW fluxes. Calibration slopes and offsets are computed for solar zenith angles (SZA) ranging from -100° to $+100^{\circ}$ degrees. For SZA greater than $+100^{\circ}$, the calibration coefficients for SZA = $+100^{\circ}$ are used. For SZA less than -100°, the calibration

coefficients for SZA = -100° are used. However, at the point where the contribution due to Channel 13 vanishes (FOV completely dark), there is a discontinuity (See Figure 3-1) in WFOV LW fluxes. This is due to the fact that calibration corrections are applied only to Channel 13 and do not correct for inherent differences between the Channel 13 and Channel 12 sensors.

3.3.4 NFOV Albedo Computation

Several potential problems exist in the computation of NFOV albedo. The directional reflectance models used in production of the MATRIX data set were a composite of previously derived models. It is indicated in the ERB Working Group Meeting #59 report (September 24, 1982; Sastri Vemury, Research and Data Systems) that when models derived from the Nimbus-7 data are used, there are significant differences in the resulting NFOV albedos. The scene selection algorithm employed in MATRIX to select the angular model to be used for a specific surface type has been questioned (see Reference 6 for a description of the scene selection algorithm). Scene selection appears to be very sensitive to a threshold radiance value employed in the algorithm. Cloud models seem to be selected more often than is appropriate at high satellite view angles. Statistical biases appear to be induced due to higher sampling rates at large satellite view angle. These problems are discussed in the ERB Working Group Meeting #56 report (September 3, 1982; Sastri Vemury, Research and Data Systems). A final problem which should be mentioned is there are often large NFOV albedos near the terminator. These problems occur when the instrument picks up a spuriously large input signal in a region where the insolation is very low. The problems described here were under study at the time of this writing. Future developments will be covered in an update to this document.

3.3.5 WFOV/NFOV Parameters Comparison

As part of the analysis of the MATRIX data set, the daily latitude band averages of various ERB parameters were studied. The basic assumption was that day-to-day changes in these parameters should be small. Also, any significant changes in the WFOV parameters should be accompanied by similar changes in the NFOV parameters. Many exceptions to these criteria were noted. Fluctuations in the populations of the latitude bands from day-to-day were found to be the source of the exceptions. These fluctuations are due to missing orbits or missing segments of orbits. This can be due to:

(1) Data Gaps

(2) Spacecraft Operational Mode

(3) MATRIX Data Rejection

The fluctuations in population result in day-to-day fluctuations in the latitude band averages of the daily MATRIX parameters. This casts doubt on the usefulness of daily latitude band

FIGURE 3-1.

Calibration-Induced Discontinuity in the *WFOV DN LW Flux*

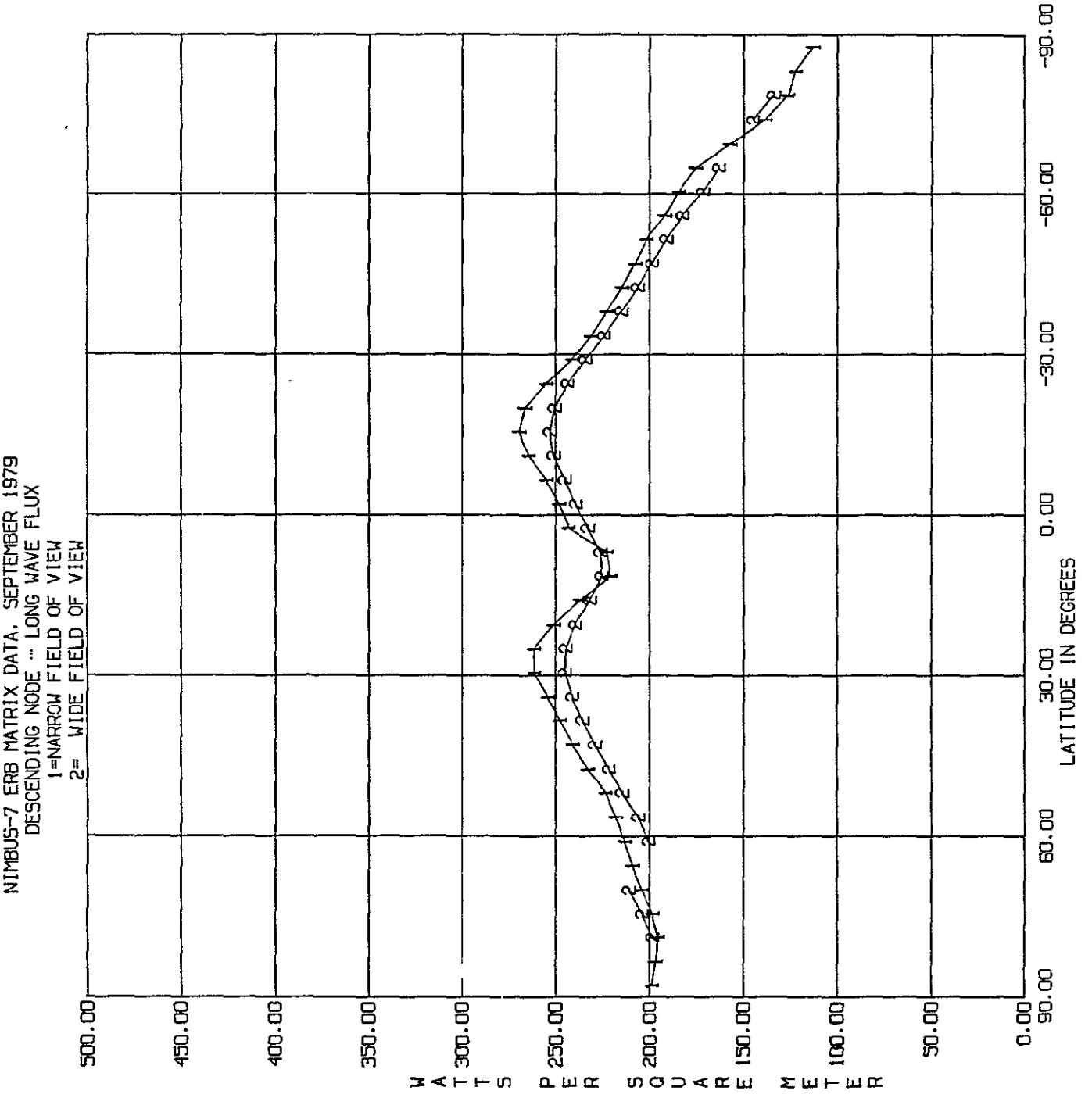

averages in scientific investigations. Monthly latitude band averages are not vulnerable to this problem. Also, individual target area averages are not affected. If a target area is covered results usually seem reliable. However, many gaps in daily spacial coverage make daily global maps unreliable.

The effect of the fluctuations discussed above is that under some conditions, the target areas contributing to a latitude zonal average may not be representative of that particular zone. On a target area basis, however, the data is still reliable.

3.3.6 Channel 13 Degradation

A calibration adjustment was applied to the Channel 13 irradiances before these were employed in the scientific calculations. A major goal of this adjustment was to correct for long-term degradation of the Channel 13 filter domes. However, in spite of this calibration adjustment there is a residual degradation which becomes apparent when the plot of monthly global averaged WFOV albedo for Year-1 is examined. A general downward trend can be observed (see Appendix E). An estimate of the residual degradation can be obtained by comparing the December, 1978 and December, 1979 globally averaged WFOV albedo.

December, 1978 - 31.9

December, 1979 - 31.3

The residual degradation over Year-1 (after calibration adjustment) was approximately 1.9%.

3.3.7 Earth Radius Error

This error existed for the first 18 months and was corrected after April 1980.

In the computation of maximum reflected energy used in computing WFOV albedo, the Earth radius was set to 6171 km instead of the correct value of 6371 km. The error induced in the maximum reflected energy is less than one percent except near the terminator. Near the terminator, the error is about one percent in the maximum reflected energy, but the reflected energy is so small that the albedo is not affected.

3.3.8 Negative Albedos

Due to data anomalies not well understood, a small number of target areas had negative values for daily averaged NFOV albedo. This occurred only five times in Year-1. Screening limits on NFOV SW radiance allow -10,000 to 350 as valid data. Occasionally a large negative noise spike will be allowed into the computation. These values represent random errors in the monthly averaged albedo parameters. Possible causes are noise in the instrument and poor data quality that was not properly flagged on the MAT.

3.3.9 Sunblip-Induced Problems

The MATRIX program rejects all WFOV irradiance data taken when the sun is in the instrument field of view (FOV). This sunblip rejection causes two types of problems in the MATRIX data products. The first type of problem consists of statistical biases in the MATRIX space and time averages. The second type of problem consists of errors introduced into the scientific parameters due to the way MATRIX algorithms handle the sunblip. These problems are briefly discussed below.

Statistical biases in the MATRIX averages are a direct result of poor sampling of the ERB world grid target areas due to sunblip. Since sunblip rejection is keyed to the solar zenith angle (see Reference 4 for details on sunblip rejection), the sunblip rejection zone moves slightly each day, following the solar declination. We have a picture like the following:

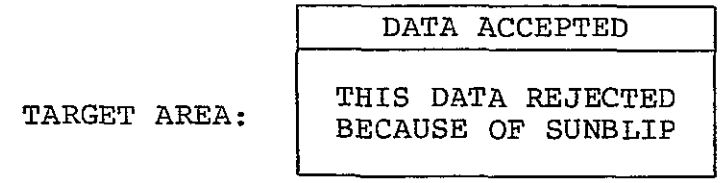

Even though the sunblip rejection heavily impacts the target area, a small amount of data is still accepted along the northern edge of the target area. A bias is introduced into the spatial average here for two reasons. First, the irradiance data accepted is binned and averaged as if it fell at the center of the target area when, in reality, it is more characteristic of the target area immediately to the north. Second, the sparse sampling in this target area leads to a larger variance about the target area mean irradiance. The motion of the sunblip rejection zone in time also introduces biases in monthly averages. The reason for this is that some target areas are sampled only during days at the beginning of a month then fall in the sunblip extinction zone for the remaining days of the month. In this case, the monthly average for the indicated target area will be representative only of the first of the month and not truly representative of the month. Similarly, biases may be introduced when target areas are sampled only at the end of the month due to motion (in time) of the sunblip rejection band.

The second type of sunblip-induced problem results from the MATRIX algorithm used to compute WFOV Total LW flux. The MATRIX algorithm computes an average of the ascending and descending LW fluxes to provide this parameter. However, if one of these is not available due to sunblip rejection, the other is the value assigned to the Total LW flux. In the sunblip zone, it is typically the DN value which is unavailable. The algorithm for Total LW flux is:

$$LW(\text{Total}) = \frac{AN + DN}{2}$$

where AN and DN are the ascending and descending LW fluxes. If sunblip rejection removes the DN LW flux from the target area being considered, the algorithm is:

$$LW(Total) = AN$$

Consider the following. Let

$$DN = AN - \Delta$$

where is the difference between AN and DN LW flux. If we substitute in the previous equation,

$$LW(Total) = AN - \frac{\Delta}{2}$$

in the sunblip zone the algorithm only provides a value of AN for LW Total flux. This is equivalent to setting Δ to zero. This causes monthly averaged LW Total flux in the sunblip zone to be overestimated by $\Delta/2$. This same error propagates to the monthly averaged Net Radiation. In the sunblip zones, the monthly averaged Net Radiation is underestimated by $\Delta/2$. The problem of sunblip bias in the MATRIX data set is currently under study by the ERB Processing Team and additional details will be reported in later volumes of this document.

SECTION 4. SUMMARY OF ITEMS CHECKED BY THE MATRIX SCIENCE QC PROGRAM

A brief description of the items checked by the MATRIX SQC program are presented here.

4.1 TAPE FORMATTING AND READABILITY CHECKS

4.1.1 Logical and Physical Record Checks

Logical and physical records are checked to assure that they have proper record lengths and legal record IDs, and that their record numbers advance properly.

4.1.2 Data Presence Checking

The MATRIX tape data files are checked to assure that all files are present and in correct sequence. The cyclic and monthly files are checked to assure that the World Maps are present and in correct sequence.

4.1.3 Trailing Documentation File (TDF) Checks

The TDF is dumped to give a record of the tapes used in production of the MATRIX tape.

4.2 LIMIT CHECKS

The MATRIX parameters are checked for data values exceeding specified tolerance limits. Counts are maintained on a daily and monthly basis of target area values which violate these limits. An additional set of tolerance limits are used to test for out-of-tolerance counts falling within 10% of the normal upper and lower bounds.

4.3 CONSISTENCY CHECKS

Consistency checks are made to assure that interrelated MATRIX parameters are internally consistent. Examples of this internal consitency are as follows: Whenever the LW population parameter is non-zero, there must be a corresponding LW flux measurement for the indicated target area; whenever albedo is computed for a target area, there should be a corresponding net radiation for the given target area.

4.4 REASONABLENESS CHECKS

4.4.1 Reasonableness Checks on Albedo and Net Radiation

Several criteria were established to assure that albedo and net radiation exhibit the proper geographic behavior. Albedo parameters should have values less than 35% in the tropics and should have values greater than 35% in polar regions. Net radiation parameters should have positive values in the tropics and should have negative values in the polar regions.

4.4.2 Latitude Band Averages

Latitude band averages were computed for all MATRIX parameters employing the 4.5-degree ERB latitude zones. This provides a quick check to assure that the MATRIX parameters show appropriate behavior across latitude.

4.4.3 Regional Averages

Six geographical regions consisting of four target areas each were selected to test the monthly averaged MATRIX parameters to assure that they showed the proper time (seasonal) behavior for their geographical locations. These areas included: Sahara, Central Pacific, South Pacific, North Pole, South Pole, and the Continental US.

4.4.4 Global Averages

Global averages were computed for all of the MATRIX parameters. These results give a quick indication of whether the MATRIX parameters show the proper seasonal behavior (across the year).

SECTION 5. SCIENCE QC DATA ANALYSIS REPORT

5.1 FORMAT CHECKS

No problems in tape format were found. However, two notes to the user are in order here. First, the tape file format changes from tape to tape. This is due to the requirement that cyclic files be included on the monthly tape for the month in which the cycle started. A further complication is that the number of files may be different for each monthly tape due to a variable number of days and/or cycles in the months. Second, users may find physical records missing on the tapes received from the archives. Occasionally the copying process, which produces user tape copies for shipping, will drop physical records. When a user encounters this problem, he should request a new tape from the archive.

5.2 LIMIT CHECKS

5.2.1 Limit Checking on Albedo Parameters

Results of limit checking on the MATRIX albedo parameters indicate that a number of target areas have albedos greater than 100% (and also greater than 110%). As discussed in Subsection 1.3.3, these high albedos occur in the region near the terminator. WFOV and NFOV albedos seem to show some correlation (in time) in this behavior. That is, in time periods where the NFOV albedo has large values, there are also large values of WFOV albedo.

Another significant result from albedo limit checking is the discovery of negative values for daily averaged NFOV albedo. The daily averaged NFOV albedo was negative in the following target areas:

DAY	TA NUMBER
350	916
21	1043
21	1123
261	1227

In each case, the data population for the target area was 2 or less. This would indicate that the problem is due to a combination of poor sampling and possible instrument noise. Negative short wave (reflected) radiances are not screened from NFOV MATRIX processing (see Reference 4).

5.2.2 Limit Checking on Net Radiation Parameters

On a daily basis, there are target area values of net radiation falling below the lower limit (-220 Watts/meter^2). However, on the monthly averages, there are no values below this limit. When maps of net radiation are generated, no values less than -200 Watts/meter^2 are contoured.

At the upper limit, there are so many values of net radiation which exceed 150 Watts/meter^2 that the limit of 165 Watts/meter^2 appears to be a better indication of the upper bound for net radiation (on a target area basis).

5.2.3 Limit Checking on Population Parameters

Two important results were obtained from the analysis of limit checking of the MATRIX population parameters. First, by counting (on a daily basis) the number of target areas which were not sampled, an assessment can be made regarding which days were impacted by data sampling problems. These results are summarized in the tables of Appendix A. These tables will give the user an indication of which days in Year-1 may be unusable due to data sampling problems. The second result concerns the monthly population parameters. In Table 5-1, results are tabulated for the percentage of monthly world grid target areas which had fewer than 3 samples. This gives the percentage of target areas for which the monthly averaged MATRIX parameters were computed with less than 3 days contributing.

One might have 3 days contributing DN data for a given TA. Then the AN data might be well sampled for 10 days but on one of the 3 days when DN was available, AN is poorly sampled. This accounts for a 0 under P24. It also accounts for the apparent discrepancy between P25 and P27. Since the DN population for many TA's during this month was 2 or 3, a less of AN data could cause significant differences between the columns for P25 and P27.

The significance of Table 5-1 is that for Parameter 27, the Total LW flux Population Counter for NFOV, the months of January and February stand out. Almost half of the world grid TA's had less than 3 counts for these months. This is consistent with the LIMS Compromise impact discussed in Subsections 3.2.2 and 3.3.1. Monthly averaged LW fluxes and net radiations are probably invalid over the Northern Hemisphere in these months.

5.3 CONSISTENCY CHECKS

There were no inconsistencies found in the MATRIX parameters. All parameters were found to be internally consistent.

TABLE 5-1.

Sparse Sampling in the ERB MATRIX Monthly Population Parameters

	WFOV AN PARM 1	WFOV DN PARM 2	SW NFOV AN PARM17	SW NFOV DN PARM18	LW NFOV AN PARM24	LW NFOV DN PARM25	LW WFOV AVG PARM26	LW WFOV AVG PARM27
NOV	41.50	56.23	3.77	90.05	0.0	0.0	11.06	0.63
DEC	9.42	21.11	3.77	90.63	0.0	0.0	1.79	0.0
JAN	4.83	19.71	3.62	91.79	0.0	0.0	1.40	47.68
FEB	10.82	25.99	1.35	92.71	0.0	37.87	1.35	49.18
MAR	1.79	10.63	0.0	87.39	0.0	46.43	1.16	0.0
APR	4.25	17.58	1.35	89.42	0.0	0.0	1.16	0.0
MAY	5.89	19.03	2.32	87.87	0.0	0.0	1.26	0.0
JUN	4.25	17.87	3.77	91.88	0.0	0.0	1.64	0.0
JUL	3.91	16.23	3.77	88.45	0.0	0.0	1.50	0.0
AUG	3.09	14.64	1.16	85.70	0.0	0.0	1.16	0.0
SEP	4.40	13.43	0.0	85.12	0.0	0.0	1.16	0.0
OCT	5.17	17.78	0.58	85.27	0.0	0.0	1.16	0.0

ERB MATRIX Monthly Population Parameters: Percentage of World Grid Target Areas with fewer than 3 samples (fewer than 3 days contributing to monthly parameters).

NOTE: 1) The zeros mean only that 3 or more days contributed - not that there was 100% data availability.

2) For many TA's the DN NFOV LW was normally sampled only for about 3 days in each month.

3) The P27 requires both AN and DN data presence.

4) The quantization interval for P25 and P27 is one day.

5.4 REASONABLENESS CHECKS

5.4.1 Reasonableness Checks on Albedo and Net Radiation

A number of exceptions to the reasonableness criteria for albedo and net radiation were found. These were explained after comparing the results with the MATRIX film product. Albedos greater than 35% were found in the tropics because of the seasonal variations in the Inter-Tropical Convergence Zone (ITCZ). Albedos less than 35% were seen in the polar regions (typically at the summer pole). These same factors account for the behavior of the net radiation. In summary, the reasonableness criteria were somewhat arbitrary. Exceptions to the criteria were found to be explainable in terms of the expected seasonal meteorological conditions.

5.4.2 Latitude Band Averages

As discussed in Subsection 3.3.4, day-to-day changes in daily latitude band averages of the principal MATRIX scientific parameters were studied. It was pointed out in that section that the daily latitude band averages are subject to unreasonable fluctuations caused by sampling problems within the bands. For this reason, the daily latitude band averages are probably not suitable for use in scientific investigations. This caveat is primarily intended to cover their use in quantitative studies since their behavior is qualitatively correct.

The monthly latitude band averages are not vulnerable to sampling problems. An appropriate method of viewing the monthly latitude band averages is use of time-latitude contour plots. These plots are presented in Appendix B for the principal MATRIX scientific parameters.

These monthly results exhibit the types of seasonal behavior that one might expect given the physical driving forces causing the observed variations. These plots are discussed in greater detail in the ERB Working Group Meeting (WGM) #35 report, RDS, March 26, 1982.

5.4.3 Regional Averages

Regional averages of the principal MATRIX parameters were computed on a monthly basis for six small regions (each consisting of four target areas). Averages were computed by averaging the target area values. Time plots of these results are presented in Appendix C. Some evidence of statistical fluctuations can be observed in these results. The plots show that the MATRIX data follows the appropriate behavior at the target area level. A possible approach which would improve the wide/narrow intercomparison in these results involves convolution of the narrow or deconvolution of the wide in order that the two results have similar resolution. The plots do indicate that the wide and the narrow results show the correct qualitative behavior across the year.

5.4.4 Global Averages

Global averages of the MATRIX parameters were computed. These are particularly well suited for studying the behavior of the parameters with time. The daily global averages of the principal MATRIX parameters were plotted across the year. These are presented in Appendix D. Several observations can be made from these plots. The scatter of the points gives an indication of the statistical variations in these parameters on a daily basis. Flyer points off the main curve indicate days impacted by data sampling problems. In general, these curves show excellent agreement with the monthly global averages. The correct seasonal behavior is also observed.

On a monthly basis, global and hemispherical averages were computed for the principal MATRIX parameters. These are presented in Appendix E. These curves also demonstrate the seasonal trends expected. Several observations can be made from these plots. First, the NFOV LW flux and NFOV net radiation appear to be unreliable in January and February (due to the LIMS Compromise). Biases can be seen between the wide and narrow of 4-5 Watts for LW flux, 2-3 percent for albedo, and 12-14 Watts for net radiation. Seasonal and geographical differences are highlighted in the plots of the hemispherical averages. These plots are discussed in greater detail in Section 2.

SECTION 6. CONCLUSIONS

The contour plots and wide/narrow plots presented in the appendices indicate close agreement between the wide and narrow sensors for the MATRIX parameters. Differences in calibration and in resolution probably contribute to the discrepancy between the wide and narrow results. As pointed out earlier in this document, the scientific algorithms are still under study and may also contribute to the observed wide/narrow differences. In the ERB WGM #35 report (RDS; March 26, 1982), it is pointed out that there is close qualitative agreement not only between wide and narrow, but also between the ERB results and those from a sensor aboard another spacecraft.

As a final note, analysis of the MATRIX film product indicates that the wide and narrow results also show close agreement on a geographical (regional) basis. (Several notes on the MATRIX film product appear in Appendix F).

The scientific algorithms were under study at the time of this writing. New developments in that area will be reported to users in updates to Volume I and Volume II of this document.

To summarize briefly, the results of the QC analysis presented here indicate that the MATRIX data is scientifically reasonable and valid for scientific use (with exceptions as noted in this report). Useful as checks on each other, the wide and narrow results show close qualitative agreement. Efforts are in progress which may produce significant improvement in the MATRIX data set.

APPENDIX A.

Data Sampling for Year-1

The daily population limit checking results were analysed to produce tables for Year-1 which give an indication of which days might have been impacted by data sampling problems. On a daily basis, the count of target areas having zero samples was used to make this assessment. By looking at enough data to determine what normal ranges of this count should be for the various wide and narrow population parameters, a determination of problem days can be made. As indicated on the next page, the sampling problems indicated in this appendix are all due to the spacecraft operational mode.

NOTES:

Y	:	Data was available for MATRIX processing
NOTE A	:	Scanner was not operating for part of the day
NOTE B	:	Scanner was not operating on Descending Node over Northern Hemisphere
NOTE C	:	Very sparse scanner data
NOTE D	:	Scanner was off for the day
NOTE E	:	Channel 12 was Narrow or Shuttered for part of this day
NOTE F	:	Channel 12 was Narrow or Shuttered for the day

Data Sampling for November, 1978

	DATA PRESENT	
DAY	WFOV	NFOV
320	Note E	Note A
321	Note E	Y
322	Note E	Y
324	Y	Y
325	Y	Y
326	Y	Y
328	Y	Y
329	Y	Y
330	Y	Y
332	Y	Y
333	Y	Y
334	Y	Note A

DATA SAMPLING FOR DECEMBER, 1978

DAY	DATA PRESENT WFOV	NFOV
336	Y	Y
337	Y	Y
338	Y	Y
340	Y	Y
341	Y	Y
342	Y	Y
344	Y	NOTE D
345	Y	Y
346	Y	Y
348	Y	NOTE C
349	Y	Y
350	Y	Y
352	Y	NOTE D
353	Y	Y
354	Y	Y
356	NOTE F	NOTE C
357	NOTE F	Y
358	NOTE F	Y
360	Y	NOTE C
361	Y	Y
362	Y	Y
364	Y	NOTE C
365		

DATA SAMPLING FOR JANUARY, 1979

DAY	DATA PRESENT WFOV	NFOV
1	Y	Y
3	Y	NOTE C
4	Y	NOTE B
5	Y	NOTE B
7	Y	NOTE C
8	Y	NOTE B
9	Y	NOTE B
11	Y	NOTE C
12	Y	Y
13	Y	NOTE B
15	Y	NOTE D
16	Y	NOTE B
17	Y	NOTE B
19	Y	NOTE D
20	Y	NOTE B
21	Y	NOTE B
23	Y	NOTE D
25	Y	NOTE B
27	Y	NOTE B
29	Y	NOTE B
31	Y	NOTE B

DATA SAMPLING FOR FEBRUARY, 1979

DAY	DATA PRESENT WFOV	NFOV
33	Y	NOTE B
35	Y	NOTE D
37	Y	NOTE C
39	Y	NOTE D
40	Y	NOTE B
41	Y	NOTE B
43	Y	NOTE C
44	Y	NOTE A
45	Y	NOTE B
47	Y	NOTE D
48	Y	Y
49	Y	NOTE A
51	Y	NOTE D
52	Y	NOTE B
53	Y	NOTE B
55	Y	NOTE D
57	Y	NOTE D
59	Y	NOTE C

DATA SAMPLING FOR MARCH, 1979

DAY	DATA PRESENT WFOV	NFOV
60	Y	NOTE A
61	Y	NOTE B
63	Y	NOTE D
64	Y	NOTE B
65	Y	NOTE B
67	Y	NOTE D
68	Y	NOTE B
69	Y	Y
71	Y	NOTE C
72	Y	Y
73	Y	Y
75	Y	NOTE C
76	Y	Y
77	Y	Y
79	Y	NOTE C
80	Y	Y
81	Y	Y
83	Y	NOTE D
84	Y	Y
85	Y	Y
87	Y	NOTE D
88	Y	Y
89	Y	Y

DATA SAMPLING FOR APRIL, 1979

DAY	DATA PRESENT WFOV	NFOV
91	Y	NOTE D
93	Y	NOTE D
95	Y	NOTE D
97	Y	NOTE D
99	Y	NOTE D
101	Y	NOTE D
103	Y	NOTE C
104	Y	Y
105	Y	Y
106	Y	Y
107	Y	Y
108	Y	Y
109	Y	Y
111	Y	NOTE C
112	Y	Y
113	Y	Y
115	Y	NOTE C
116	Y	Y
117	Y	Y
118	Y	Y
119	Y	Y

DATA SAMPLING FOR MAY, 1979

DAY	DATA PRESENT WFOV	NFOV
121	Y	NOTE D
123	Y	Y
124	Y	Y
125	Y	Y
127	Y	NOTE D
128	Y	Y
129	Y	NOTE D
131	Y	Y
133	Y	Y
134	Y	Y
135	Y	Y
137	Y	Y
139	Y	Y
140	Y	Y
141	Y	Y
143	Y	Y
144	Y	Y
145	Y	Y
147	Y	Y
148	Y	Y
149	Y	Y

DATA SAMPLING FOR JUNE, 1979

DAY	DATA PRESENT WFOV	NFOV
152	Y	Y
153	Y	Y
155	Y	Y
156	Y	Y
157	Y	Y
159	Y	Y
160	Y	Y
161	Y	Y
163	Y	Y
164	Y	Y
165	Y	Y
167	Y	Y
168	Y	Y
169	Y	Y
171	Y	Y
172	Y	Y
173	Y	Y
175	Y	Y
176	Y	Y
177	Y	Y
179	Y	NOTE A
180	Y	Y
181	Y	Y

DATA SAMPLING FOR JULY, 1979

DAY	DATA PRESENT WFOV	NFOV
183	Y	Y
184	Y	Y
185	Y	Y
187	Y	Y
188	Y	Y
189	Y	Y
191	Y	Y
192	Y	Y
193	Y	Y
195	Y	Y
196	Y	Y
197	Y	Y
199	NOTE E	Y
200	Y	Y
201	Y	Y
203	Y	Y
204	Y	Y
205	Y	Y
207	Y	Y
208	Y	Y
209	Y	Y
211	Y	Y
212	Y	Y

DATA SAMPLING FOR AUGUST, 1979

DAY	WFOV	NFOV
213	Y	Y
215	Y	Y
216	Y	Y
217	Y	Y
219	Y	Y
220	Y	Y
221	Y	Y
223	Y	Y
224	Y	Y
225	Y	Y
227	Y	Y
228	Y	Y
229	Y	Y
231	Y	Y
232	Y	Y
233	Y	Y
235	Y	Y
236	Y	Y
237	Y	Y
239	Y	Y
240	Y	Y
241	Y	Y
243	Y	Y

DATA SAMPLING FOR SEPTEMBER, 1979

DAY	DATA PRESENT WFOV	NFOV
244	Y	Y
245	Y	Y
247	Y	Y
248	Y	Y
249	Y	Y
251	Y	Y
252	Y	Y
253	Y	Y
255	Y	Y
256	Y	Y
257	Y	Y
259	Y	Y
260	Y	Y
261	Y	Y
263	Y	Y
264	Y	Y
265	Y	Y
267	Y	Y
268	Y	Y
269	Y	Y
271	Y	Y
272	Y	NOTE C
273	Y	Y

DATA SAMPLING FOR OCTOBER, 1979

DAY	DATA PRESENT WFOV	NFOV
275	Y	Y
276	Y	NOTE C
277	Y	Y
279	Y	Y
280	Y	Y
281	Y	Y
283	Y	Y
284	Y	Y
285	Y	Y
287	Y	Y
288	Y	Y
289	Y	Y
291	NOTE F	Y
292	NOTE F	Y
293	NOTE F	Y
295	Y	Y
296	Y	Y
297	Y	Y
299	Y	Y
300	Y	NOTE C
301	Y	Y
303	Y	Y
304	Y	NOTE C

APPENDIX B.

Time-Latitude Contour Plots

Time-latitude contour plots are presented for the principal MATRIX scientific parameters:

AN LW Flux	-	WFOV
DN LW Flux	-	WFOV
Total LW Flux	-	WFOV
AN LW Flux	-	NFOV
DN LW Flux	-	NFOV
Total LW Flux	-	NFOV
Albedo	-	WFOV
Albedo	-	NFOV
Net Radiation	-	WFOV
Net Radiation	-	NFOV

These plots cover the time period (along the X-axis) from November 16, 1978 to October 31, 1979. Units of flux parameters are Watts/meter^2. Units of albedo parameters are percent (albedo units).

CONTOURS OF LATITUDE BAND AVERAGES FOR WFOV L.W. FLUX - A.N.

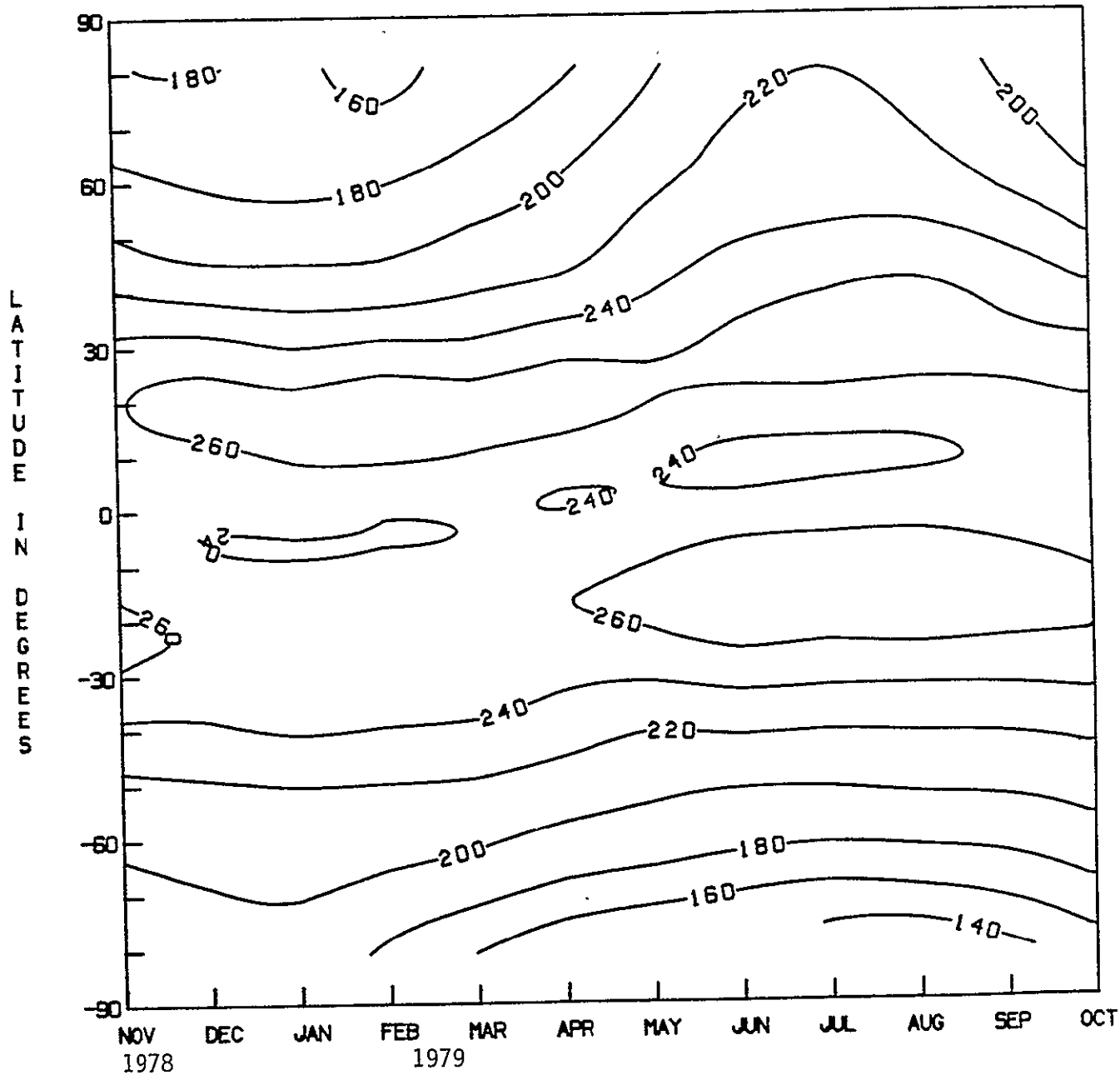

CONTOURS OF LATITUDE BAND AVERAGES FOR WFOV L.W. FLUX - D.N.

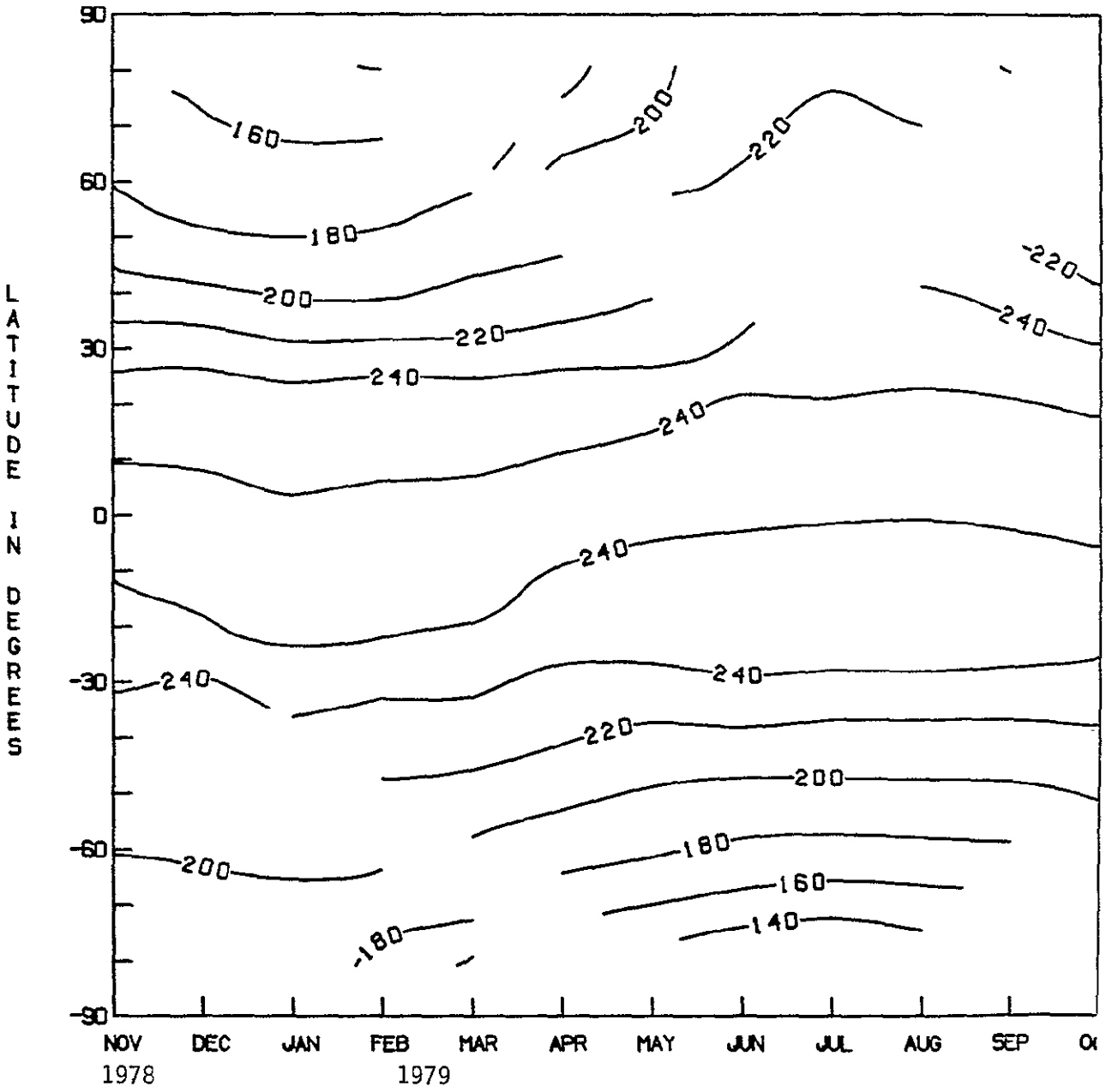

CONTOURS OF LATITUDE BAND AVERAGES FOR NFOV L.W. FLUX - A.N.

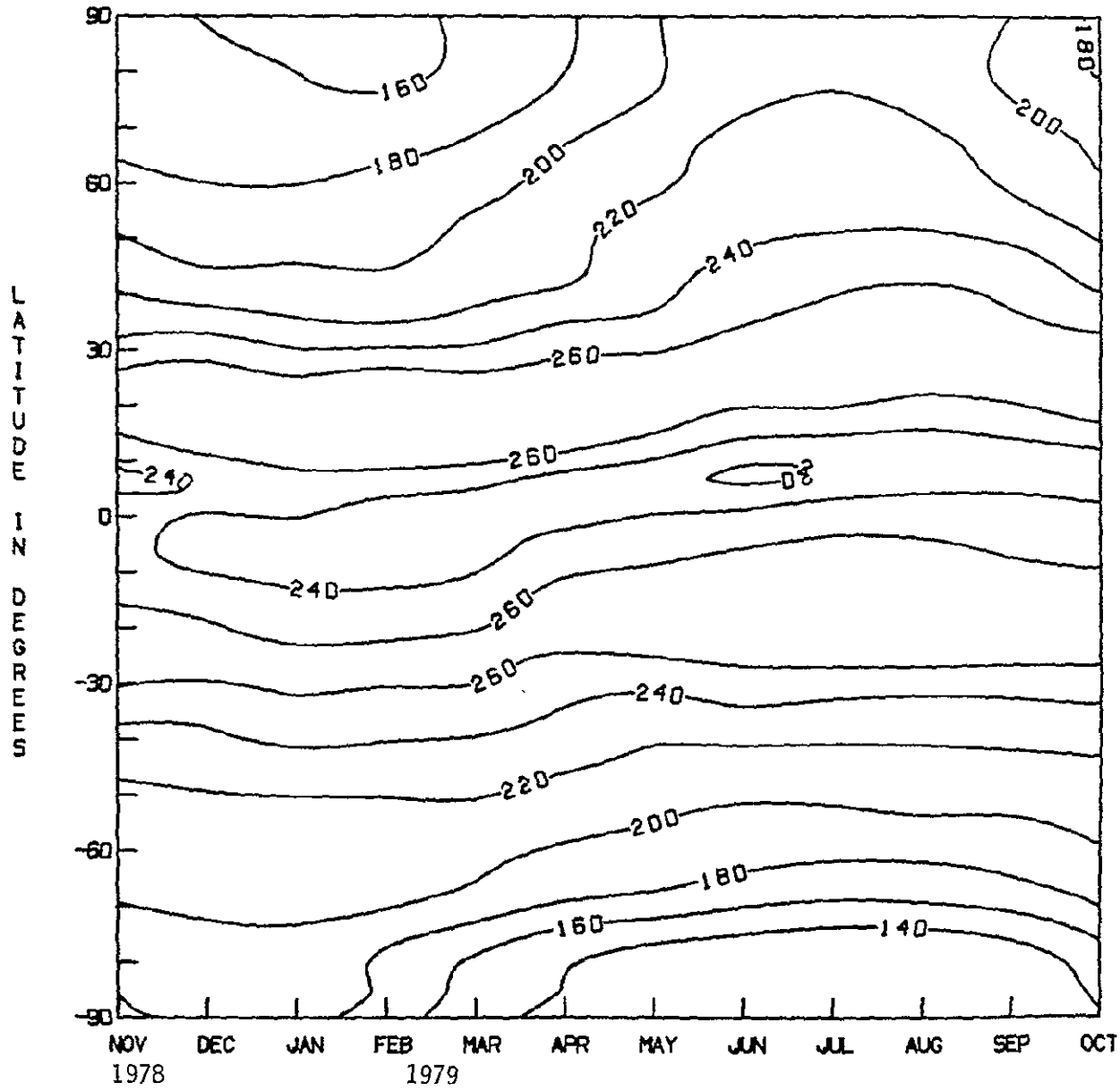

CONTOURS OF LATITUDE BAND AVERAGES FOR NFOV L.W. FLUX - D.N.

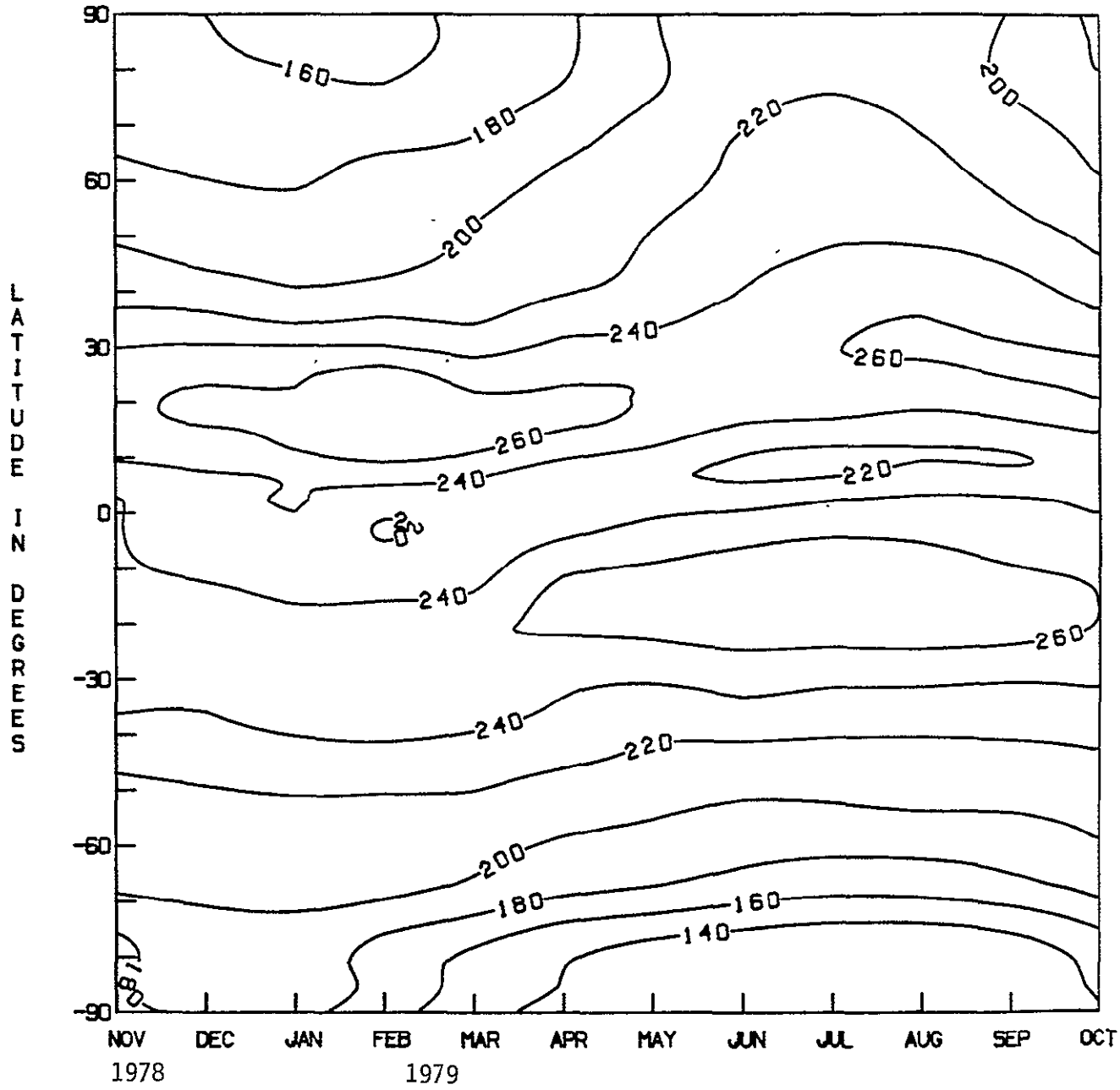

APPENDIX C.

Regional Average Plots

Plots of regional averages of MATRIX parameters are presented for six geographical regions:

1) Sahara

2) Central Pacific

3) South Pacific

4) South Pole

5) North Pole

6) Continental US

Each region consists of four ERB world grid target areas. Straight averages of the parameters values from the four TA's were computed for use here. The time period covered is November 16, 1978 to October 31, 1979. Some fluctuations appear to be due to statistical fluctuations (sampling) on the TA level. Albedo plots show gaps where the terminator crosses the indicated region. Large albedo values are also indicated in some cases near the terminator (see Subsection 3.2.4).

An interesting note is the behavior of the LW terrestrial flux (average of AN and DN) at the South Pole. Over most regions, the narrow instrument sees a "warmer" Earth than does the wide. This situation is reversed at the South Pole. This reversal is probably due to the difference in resolution of the two instruments. There is a significant amount of water in the Field of View (FOV) of the wide sensor. The narrow sensor sees only the indicated target areas, and has no water in its FOV. This plausibility argument can also be applied to explain the seasonal changes in the wide/narrow intercomparison at the South Pole.

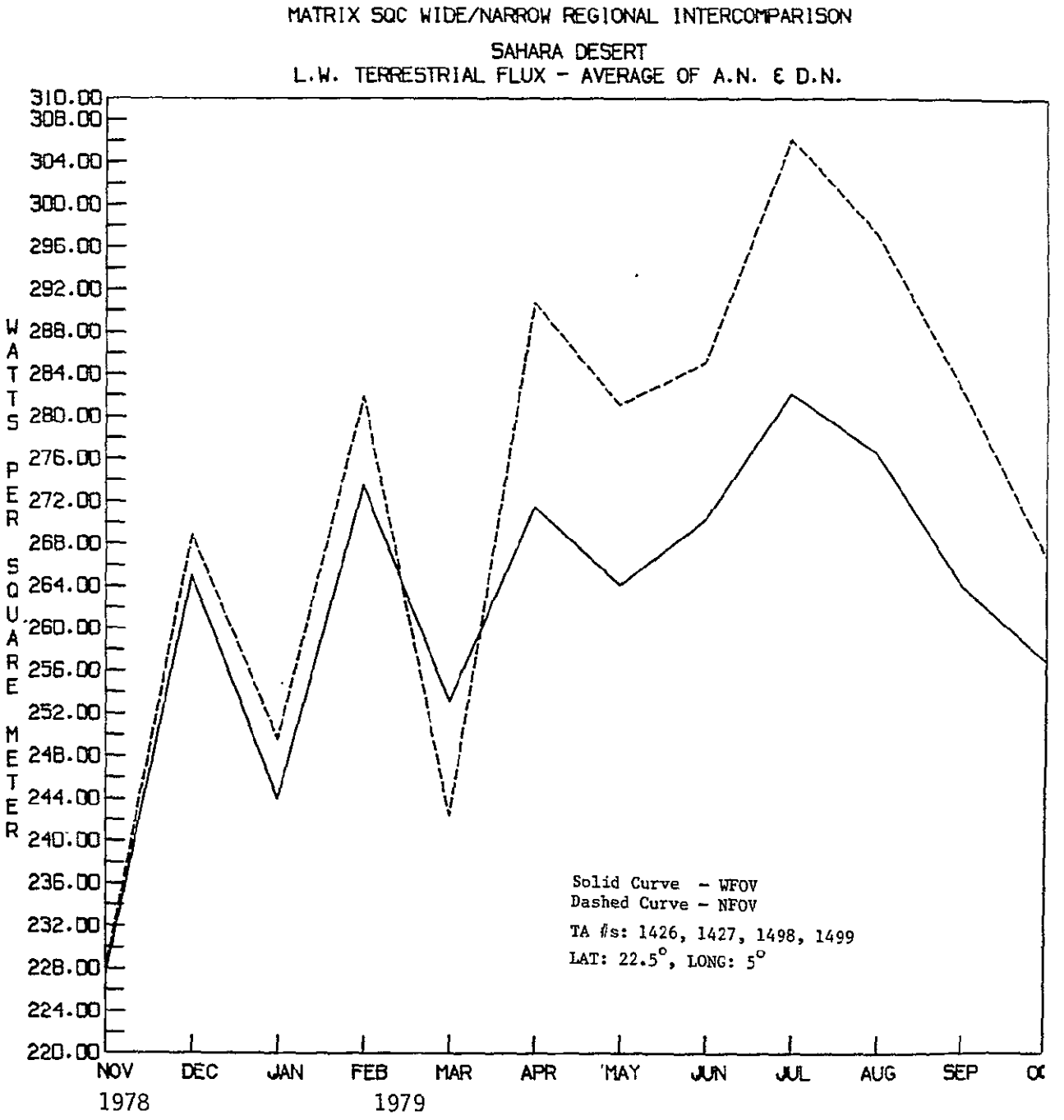

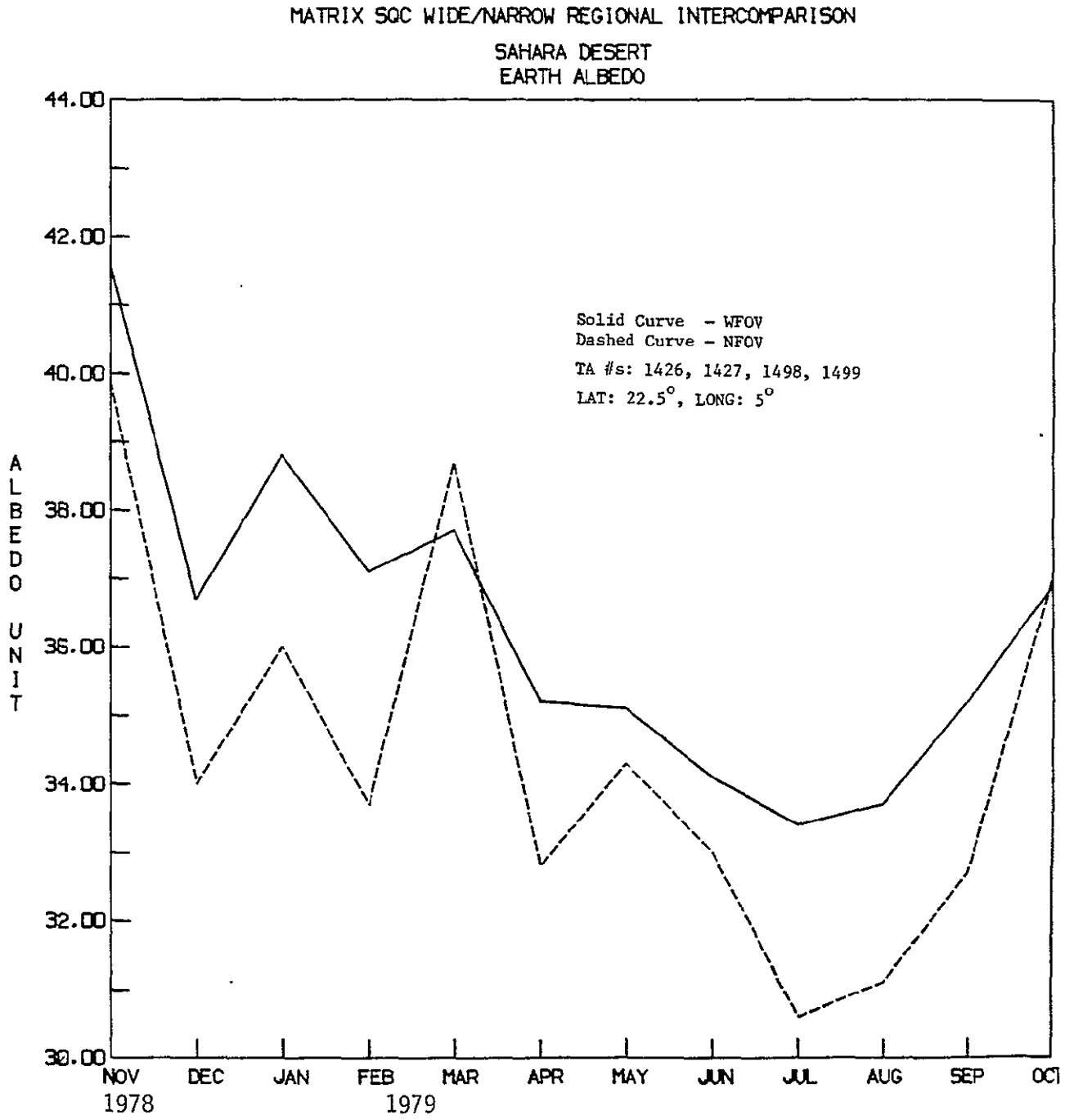

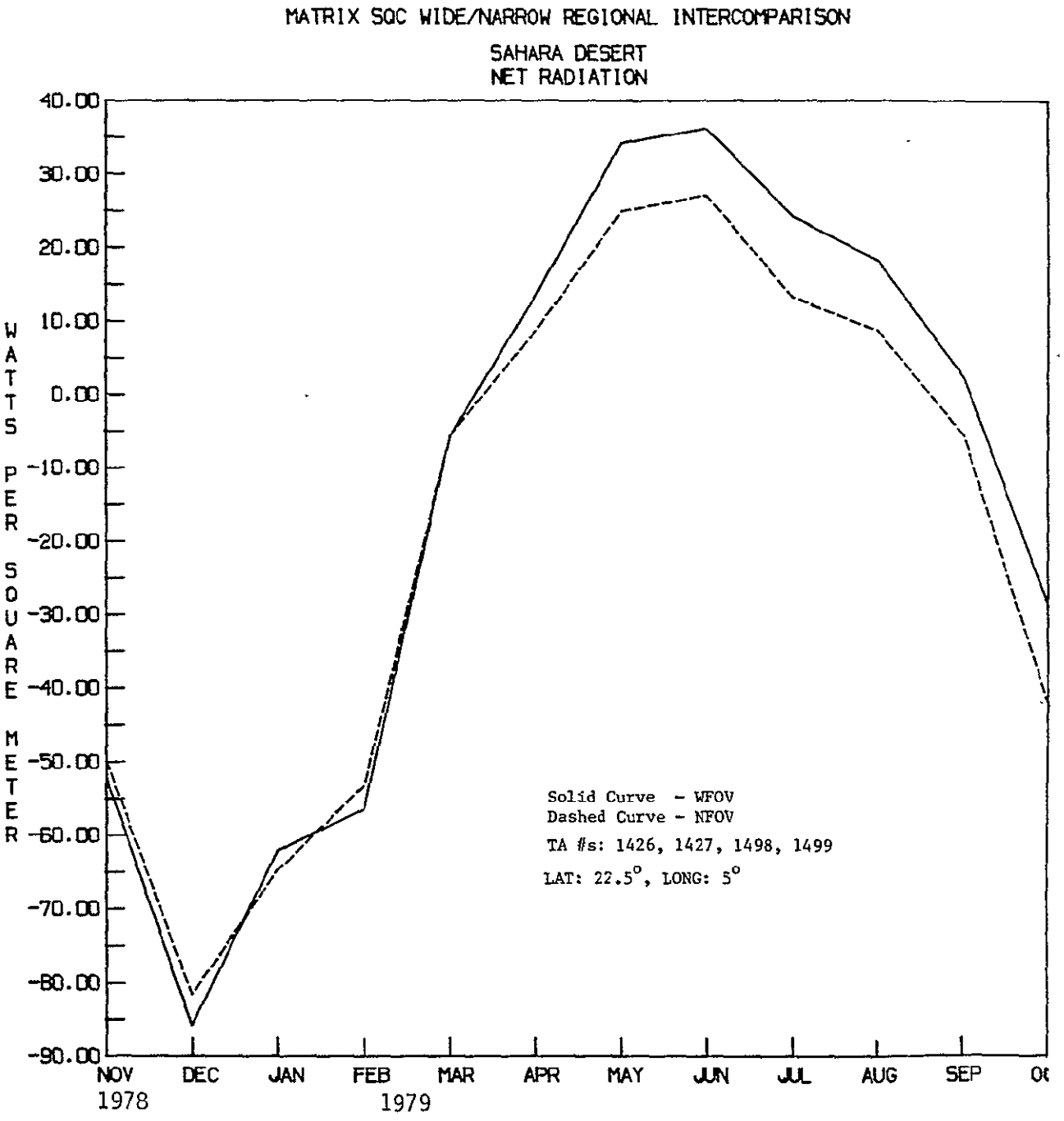

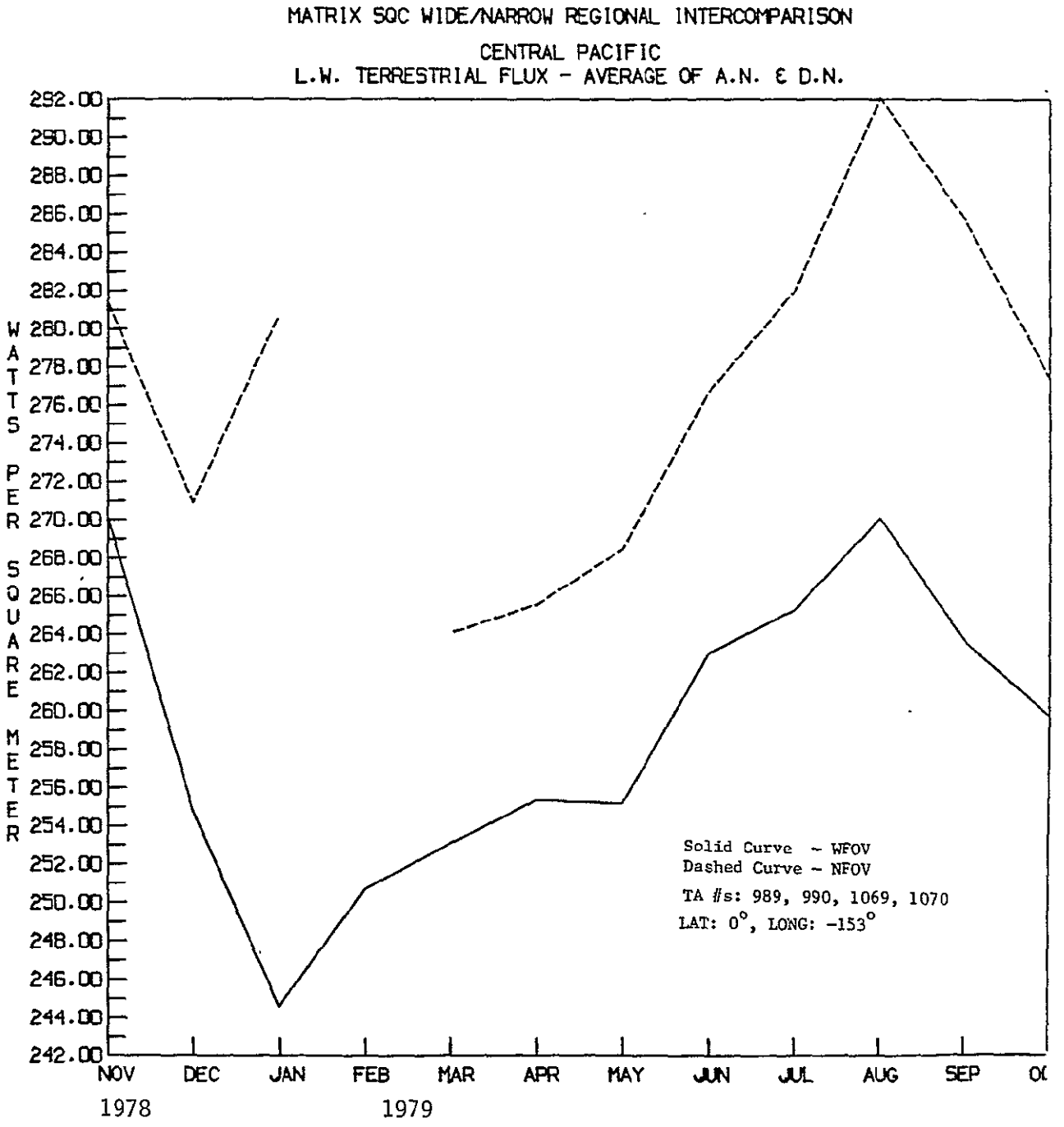

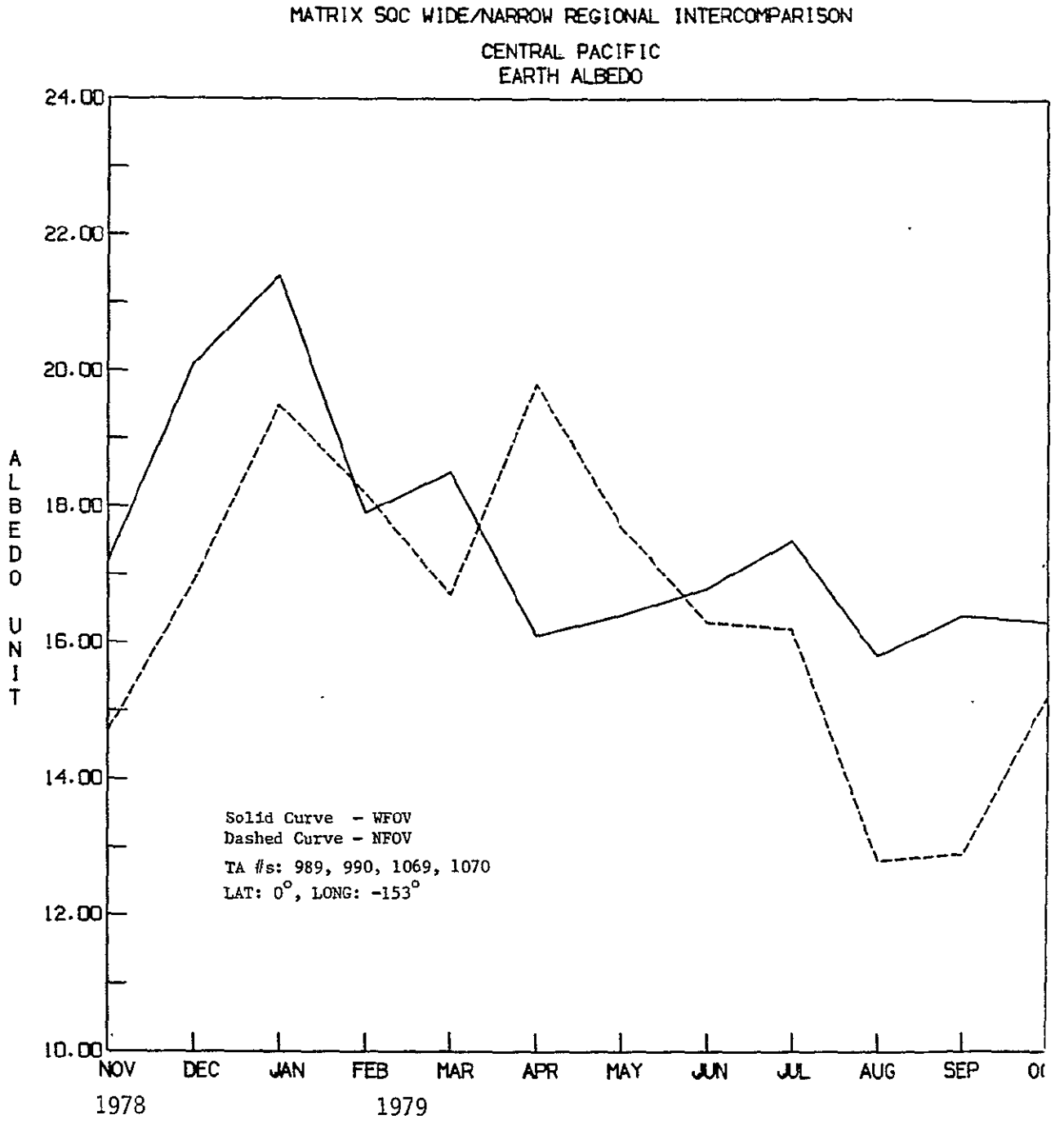

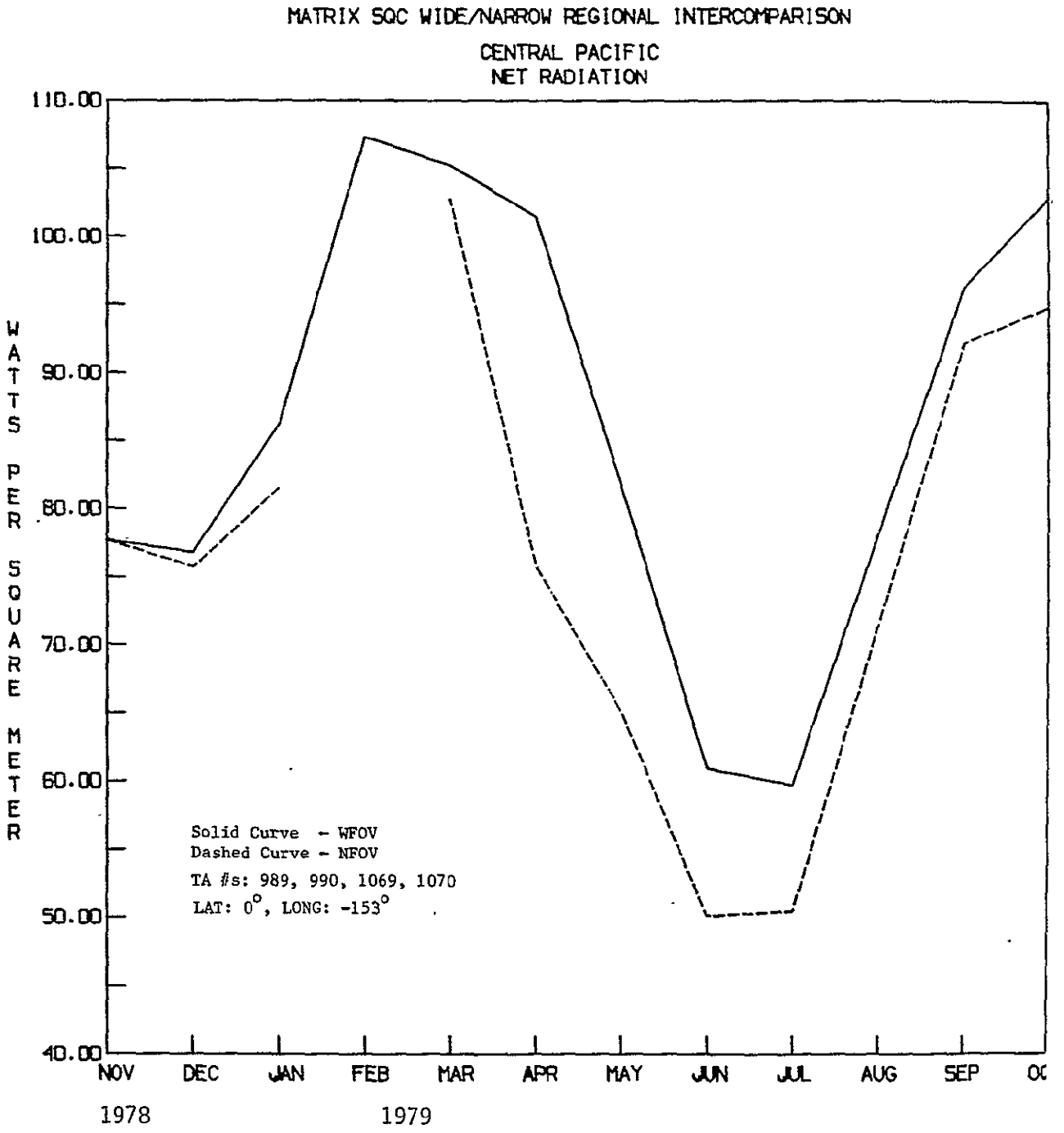

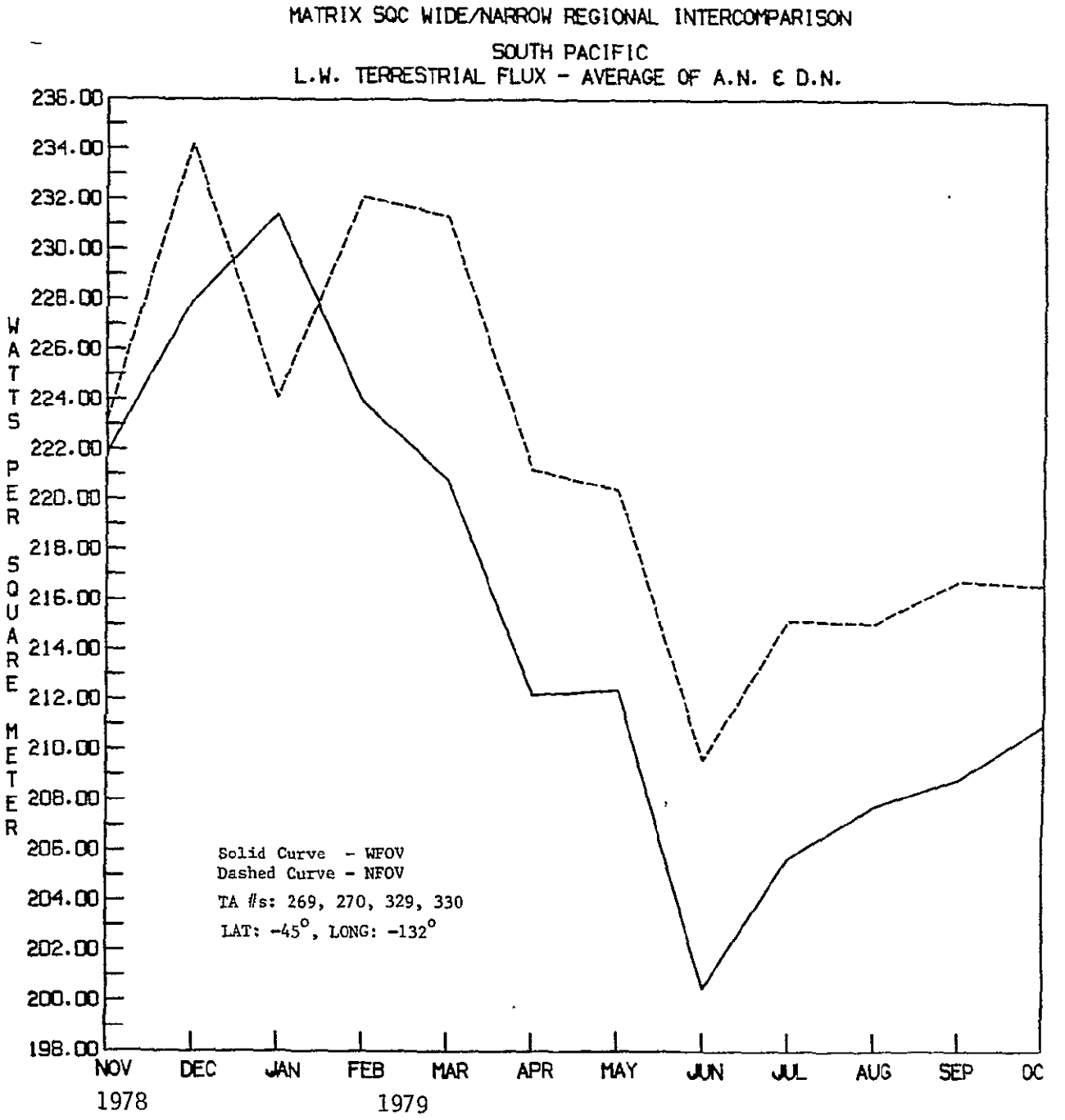

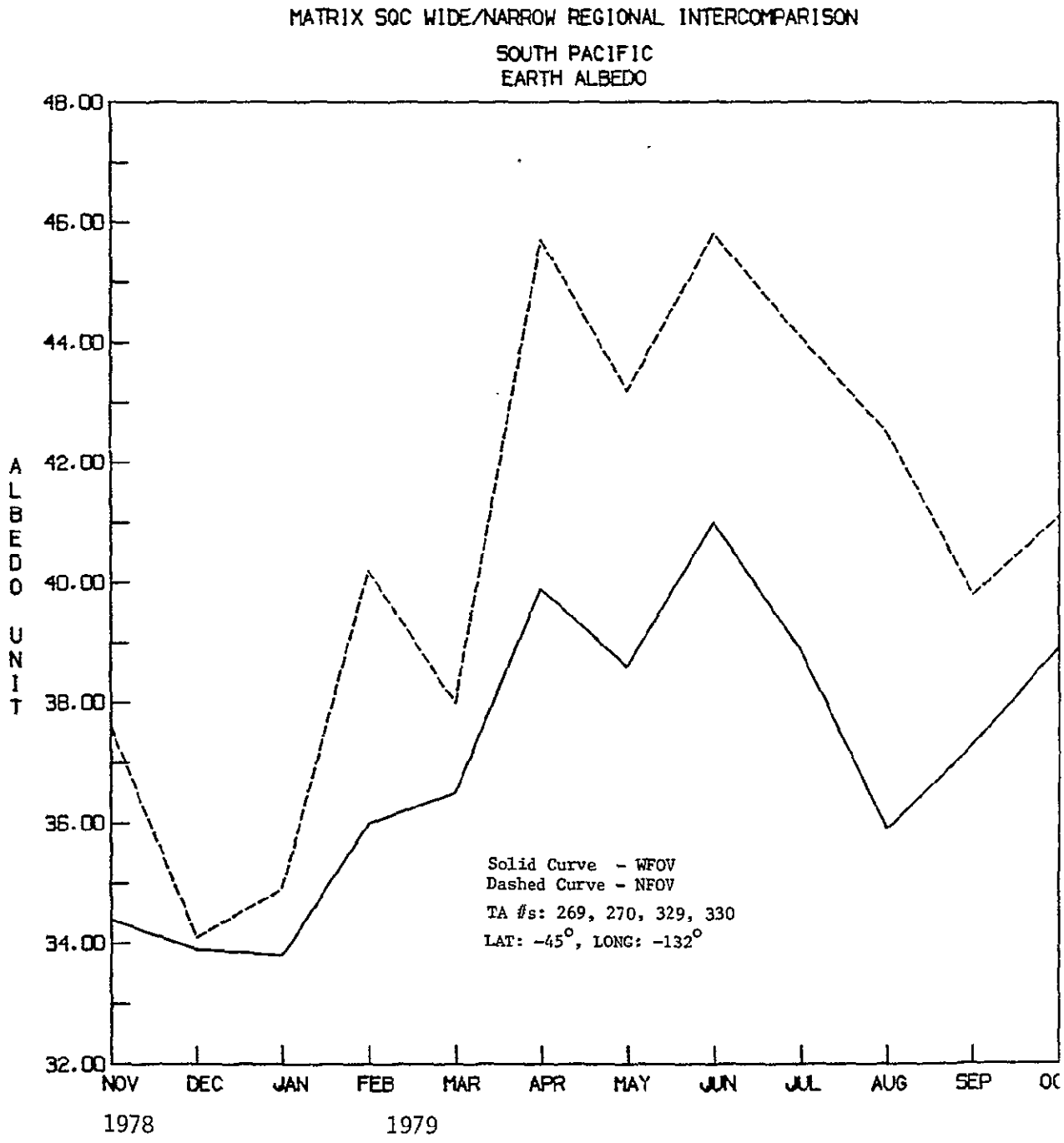

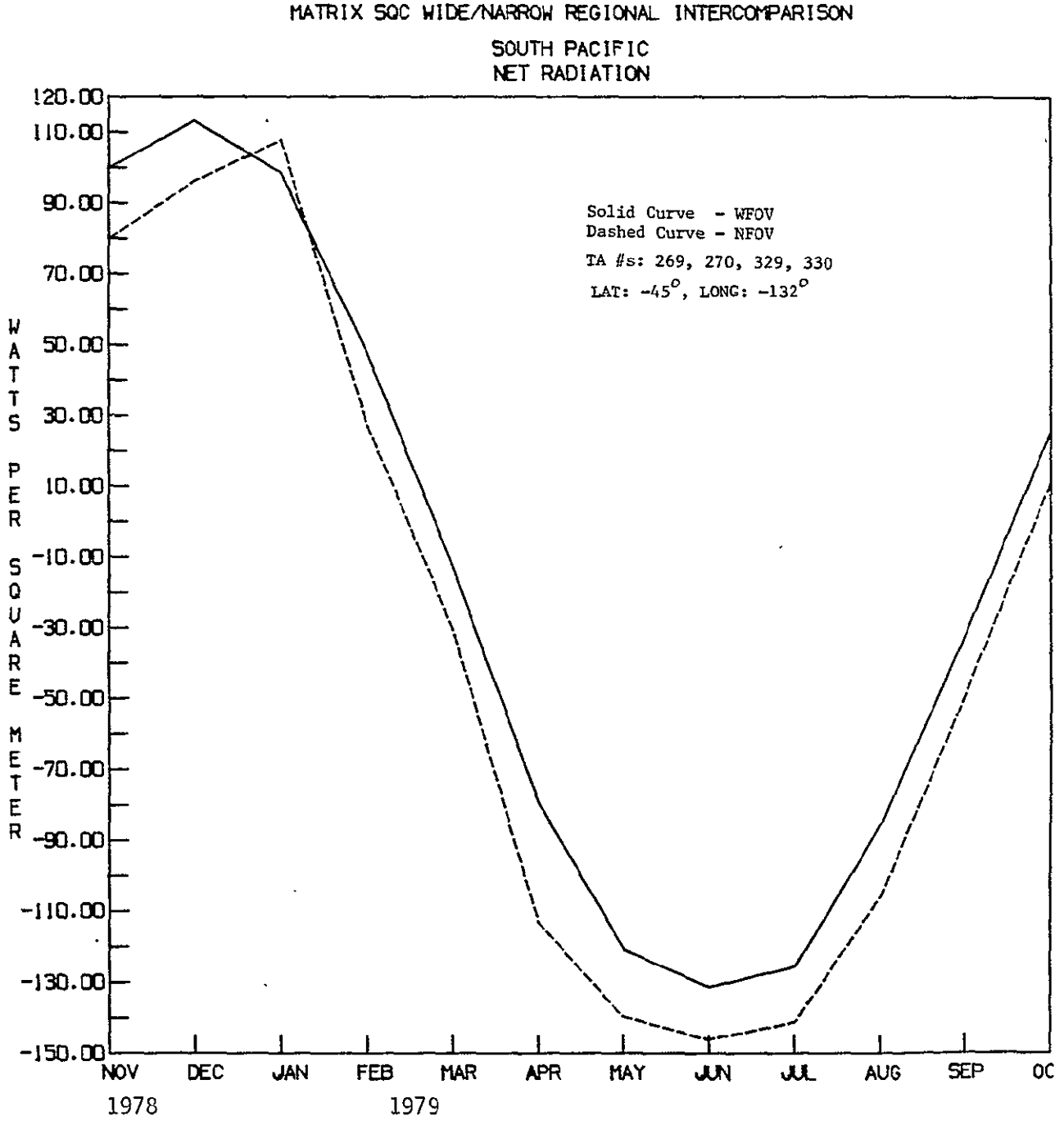

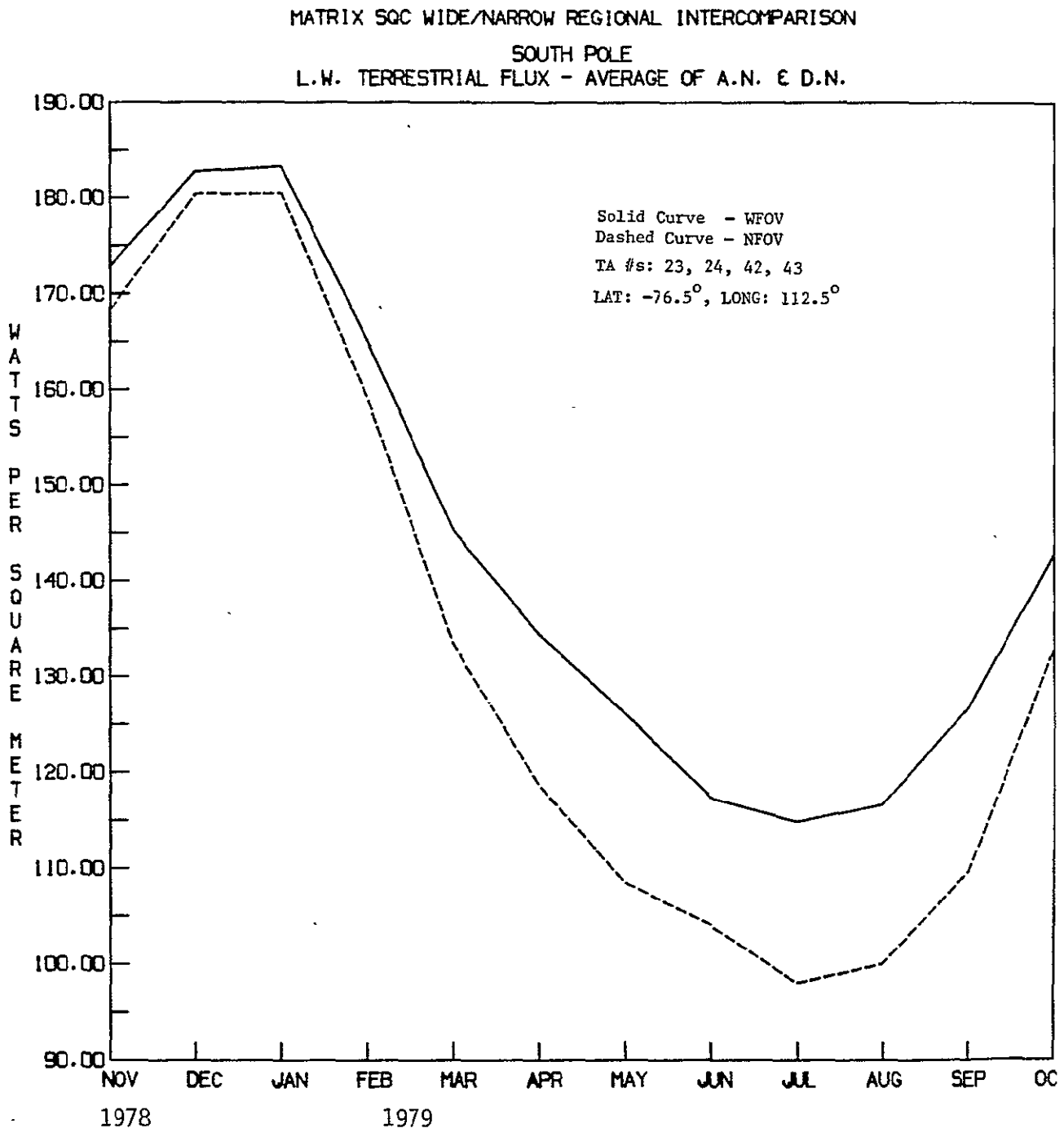

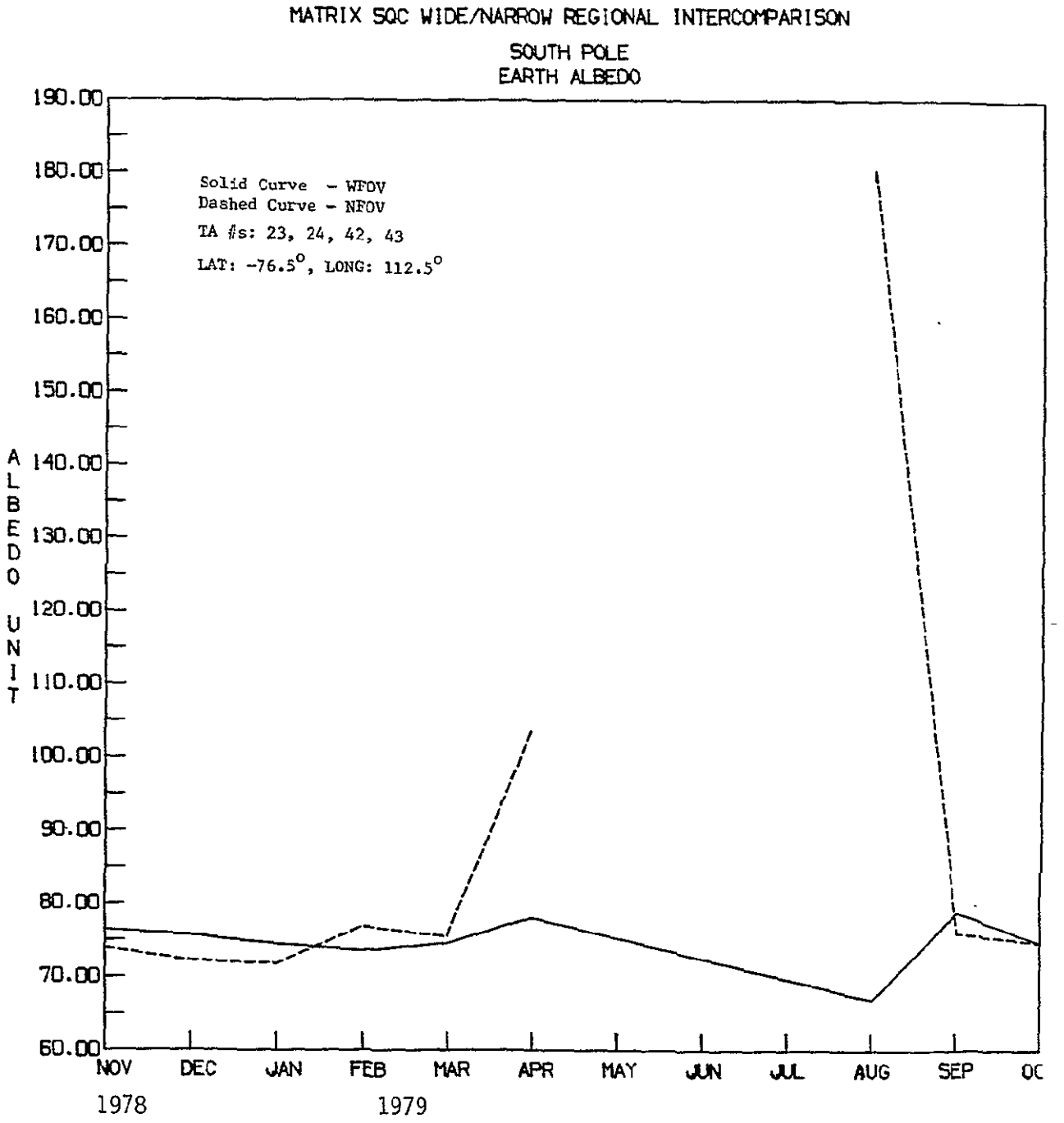

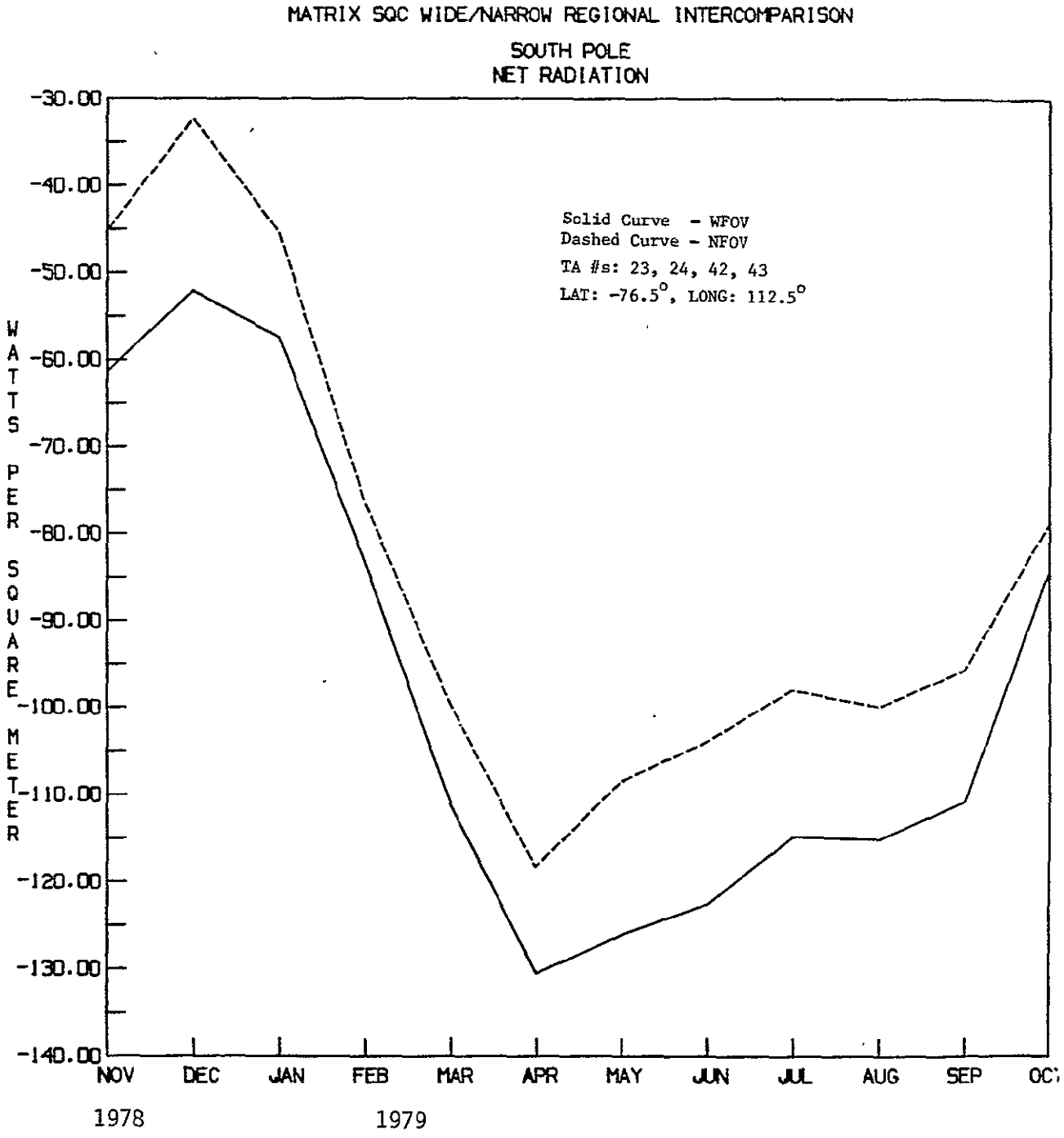

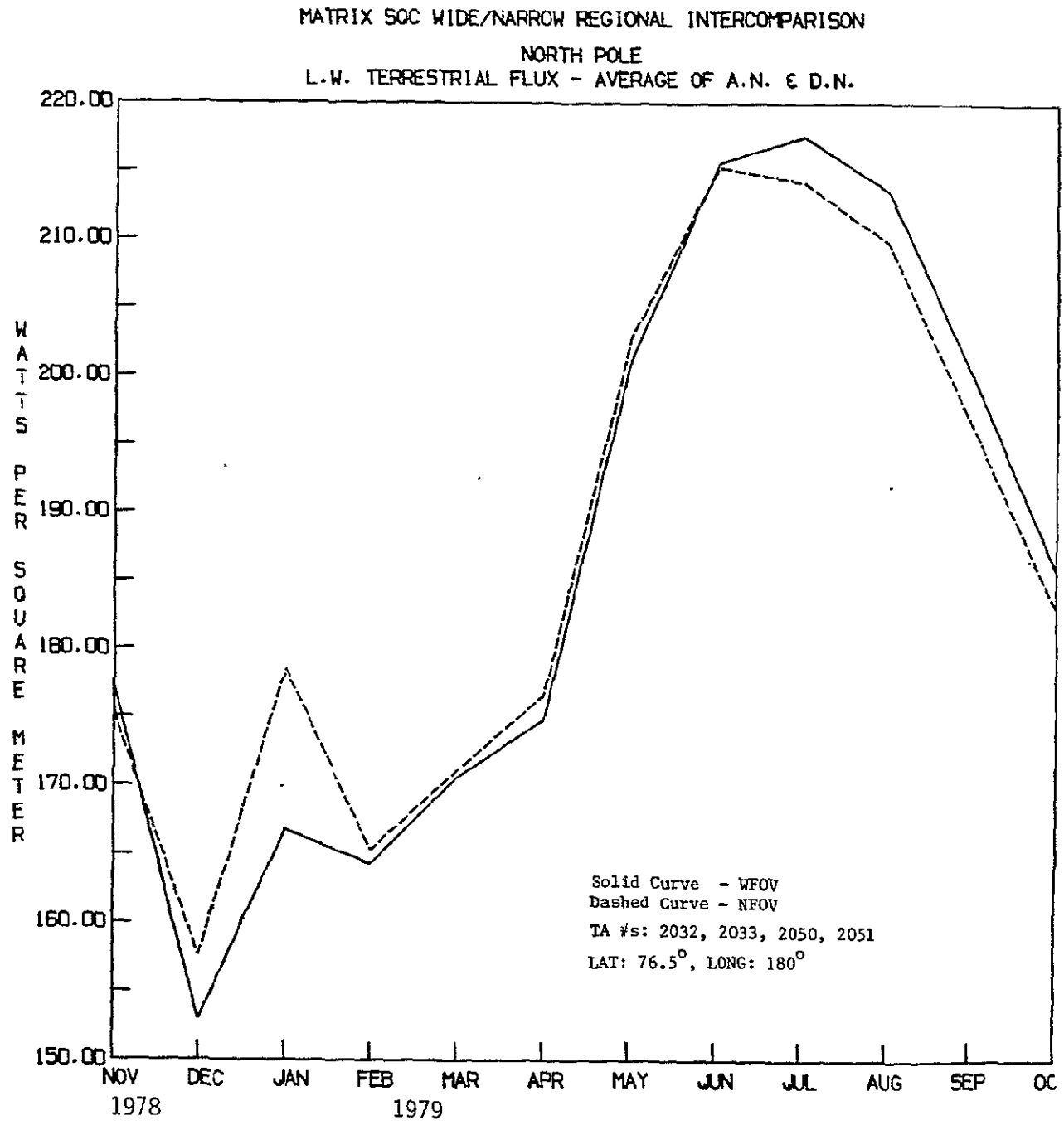

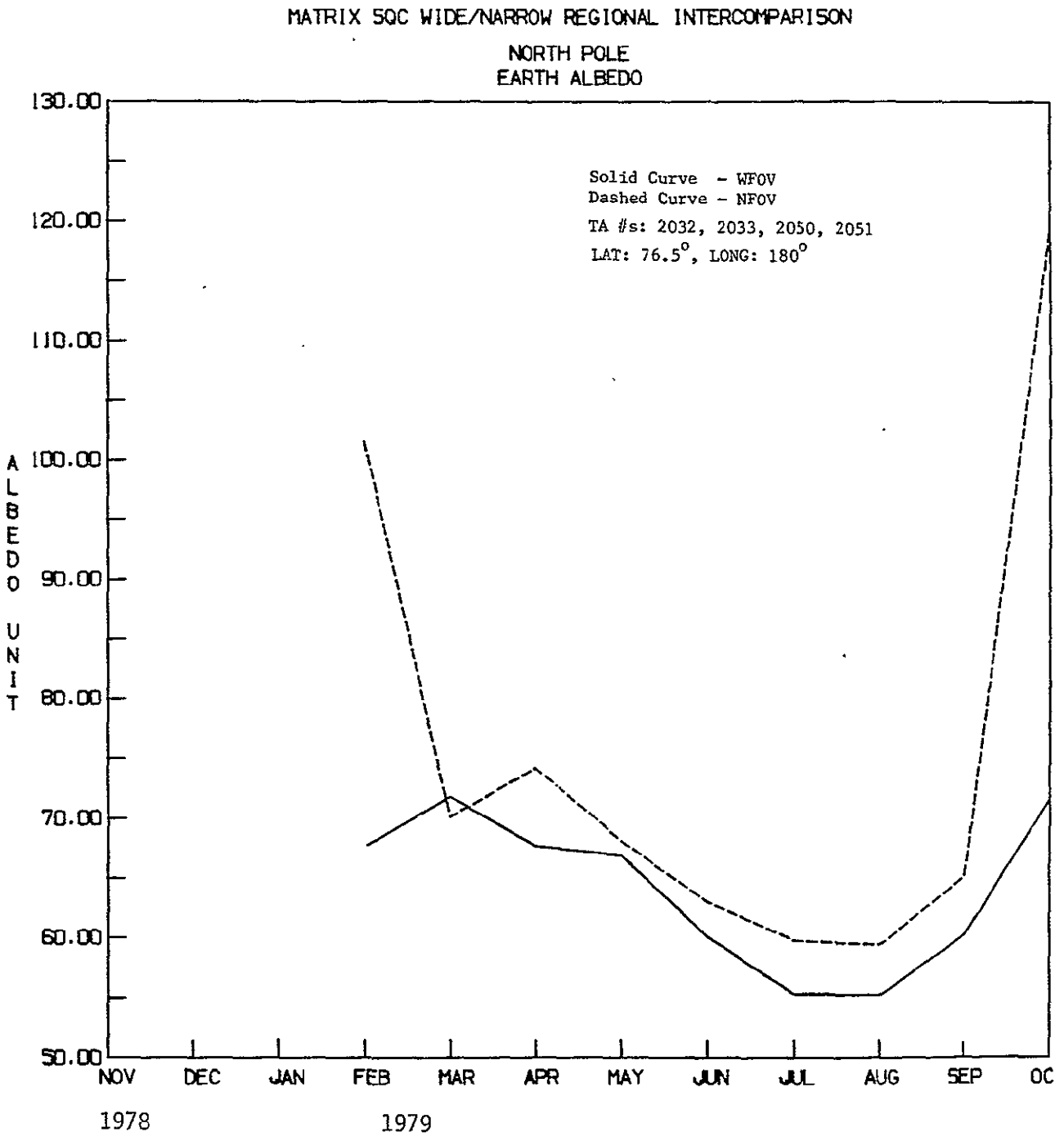

ORIGINAL PAGE IS
OF POOR QUALITY

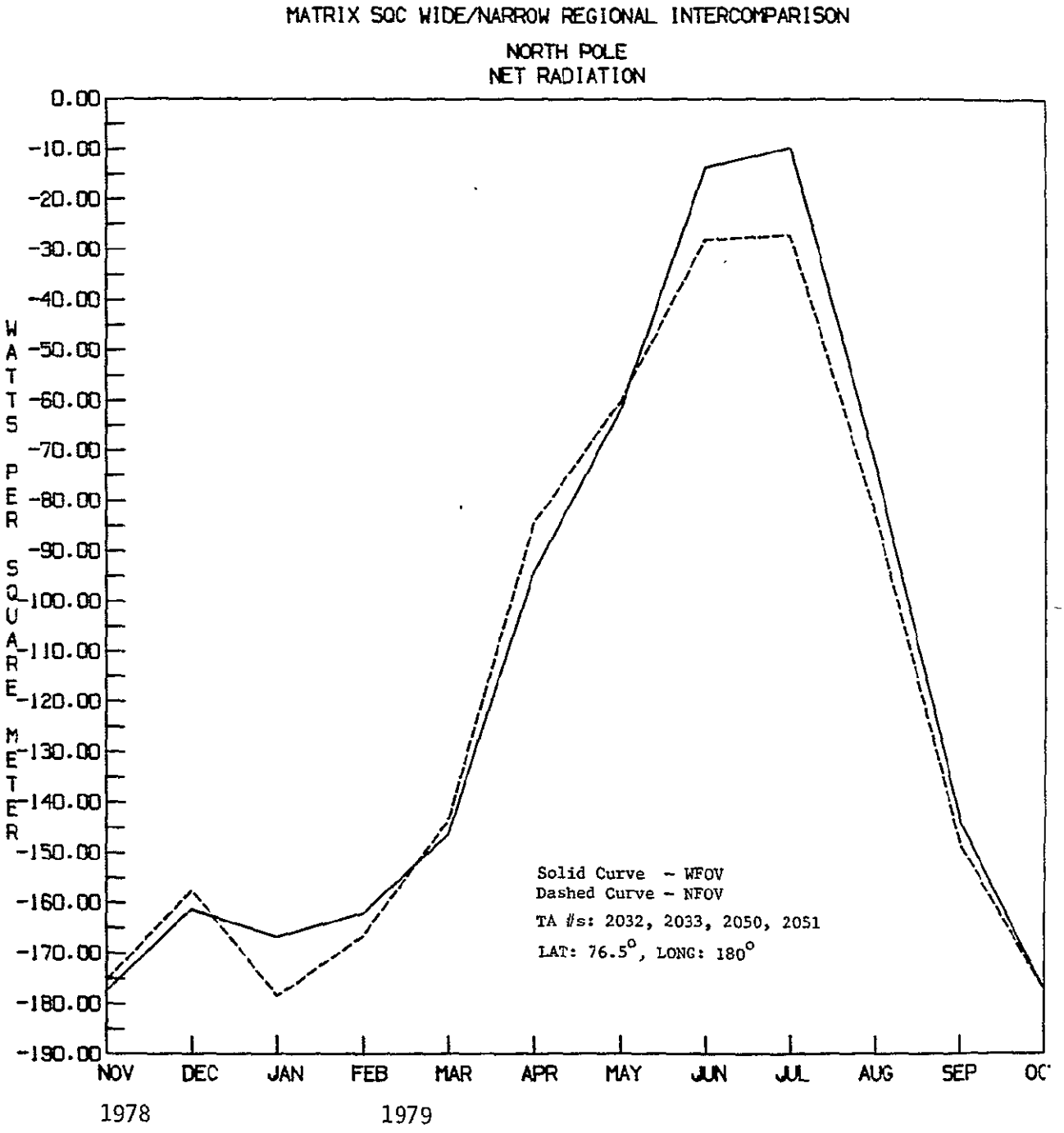

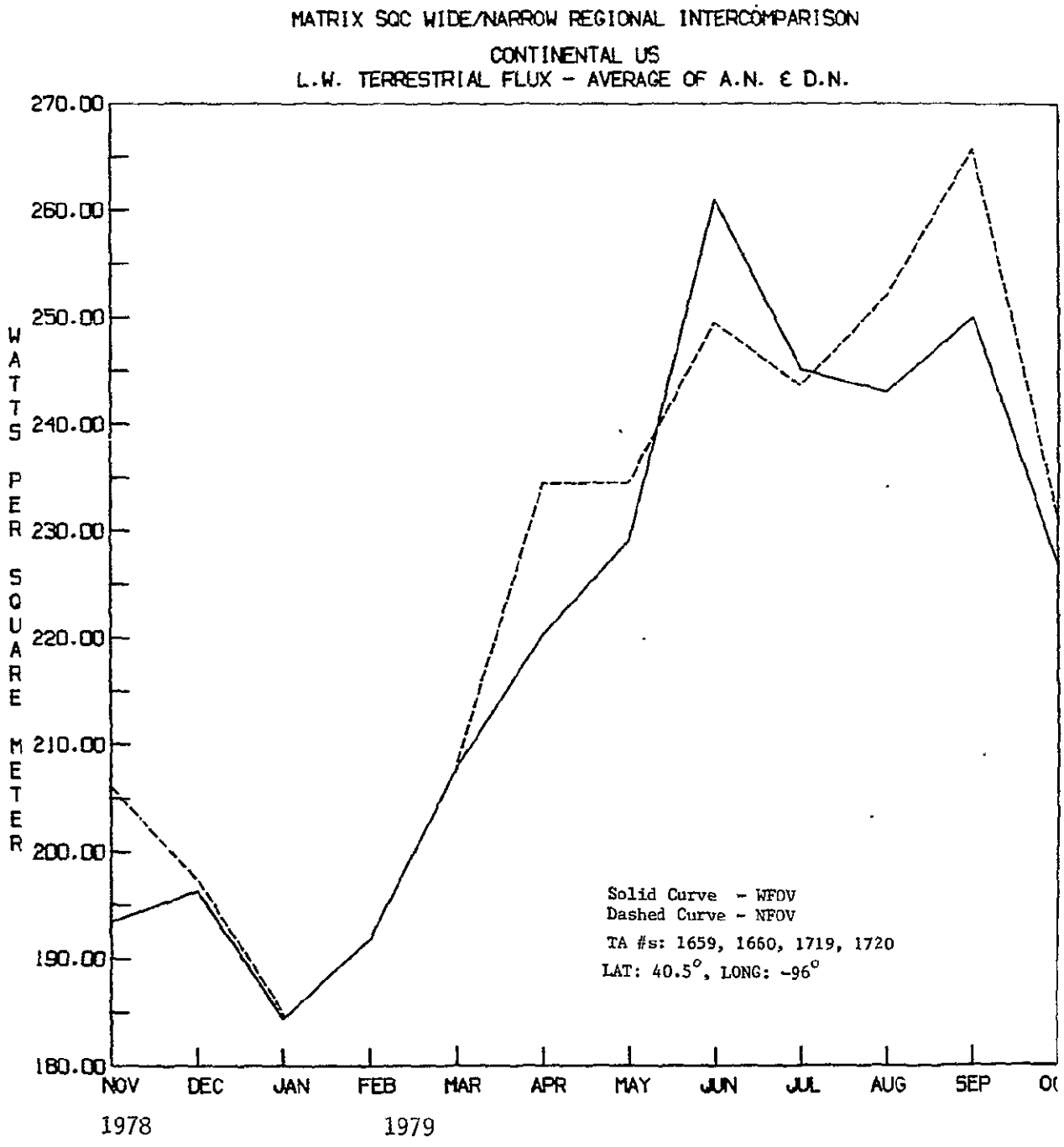

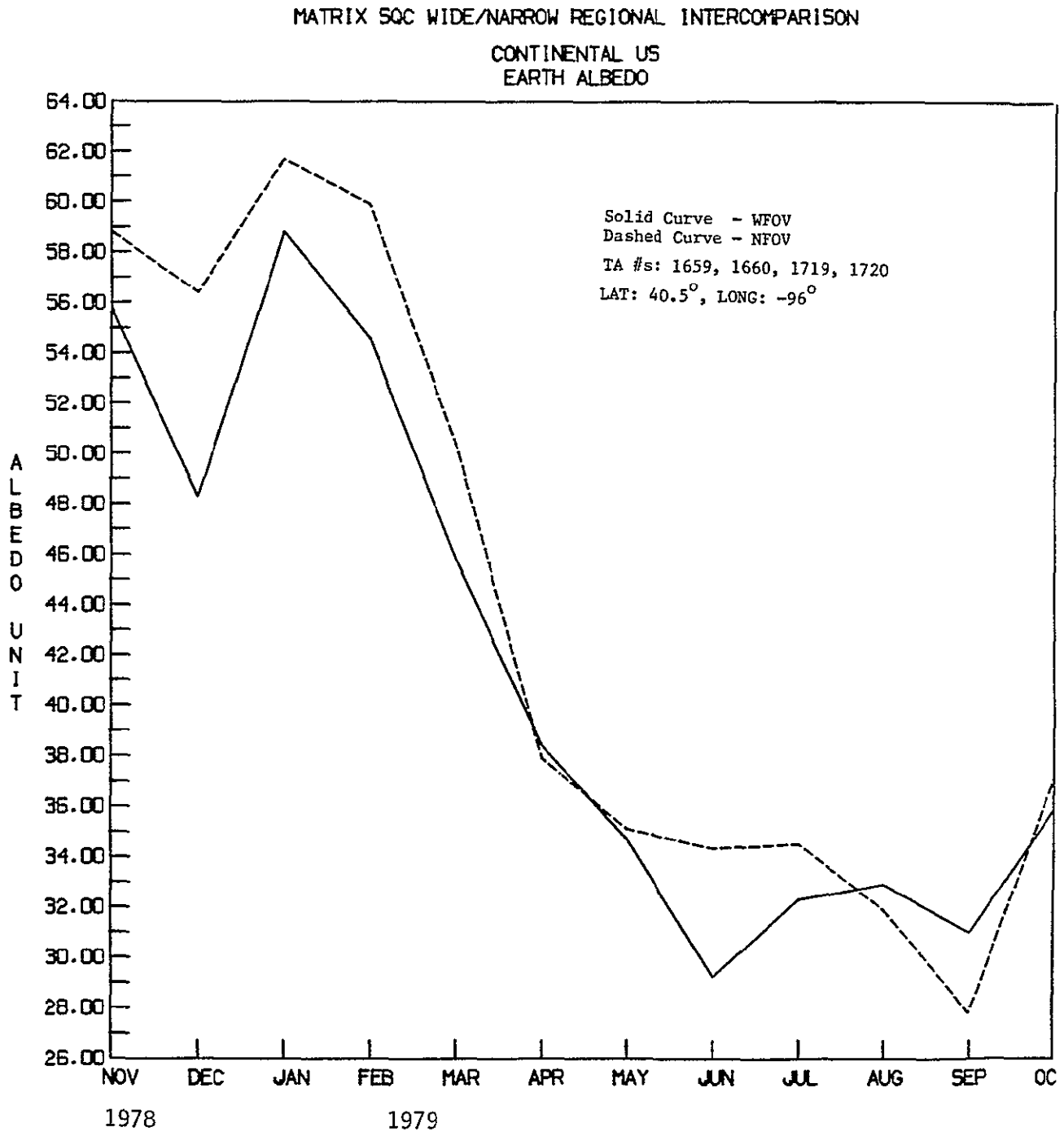

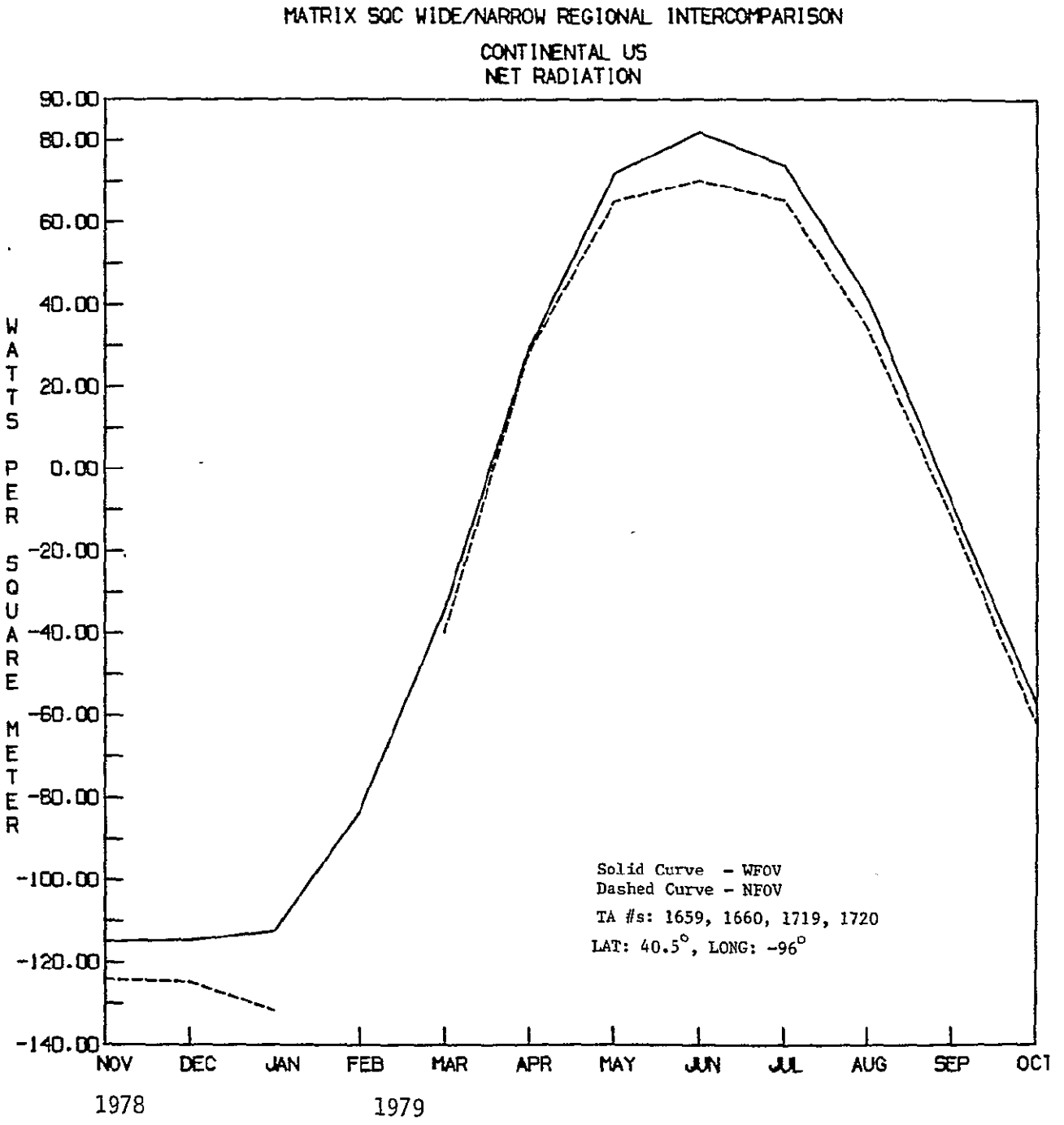

APPENDIX D.

Daily Global Average Plots

Plots of daily global averages for the principal MATRIX scientific parameters are presented. The units along the X-axis are a modified mission day number. Day 0 is November 1, 1978; etc. The time period covered by the data is November 16, 1978 to October 31, 1979. The scatter in the data is an indication of the statistical fluctuations in the daily averages of the MATRIX parameters. Flyer points can be correlated with the known days which have data sampling problems. The effect of the LIMS Compromise is especially noticeable in the NFOV LW flux and net radiation parameters.

GLOBAL AVERAGE FOR WFOV LW FLUX (AN)

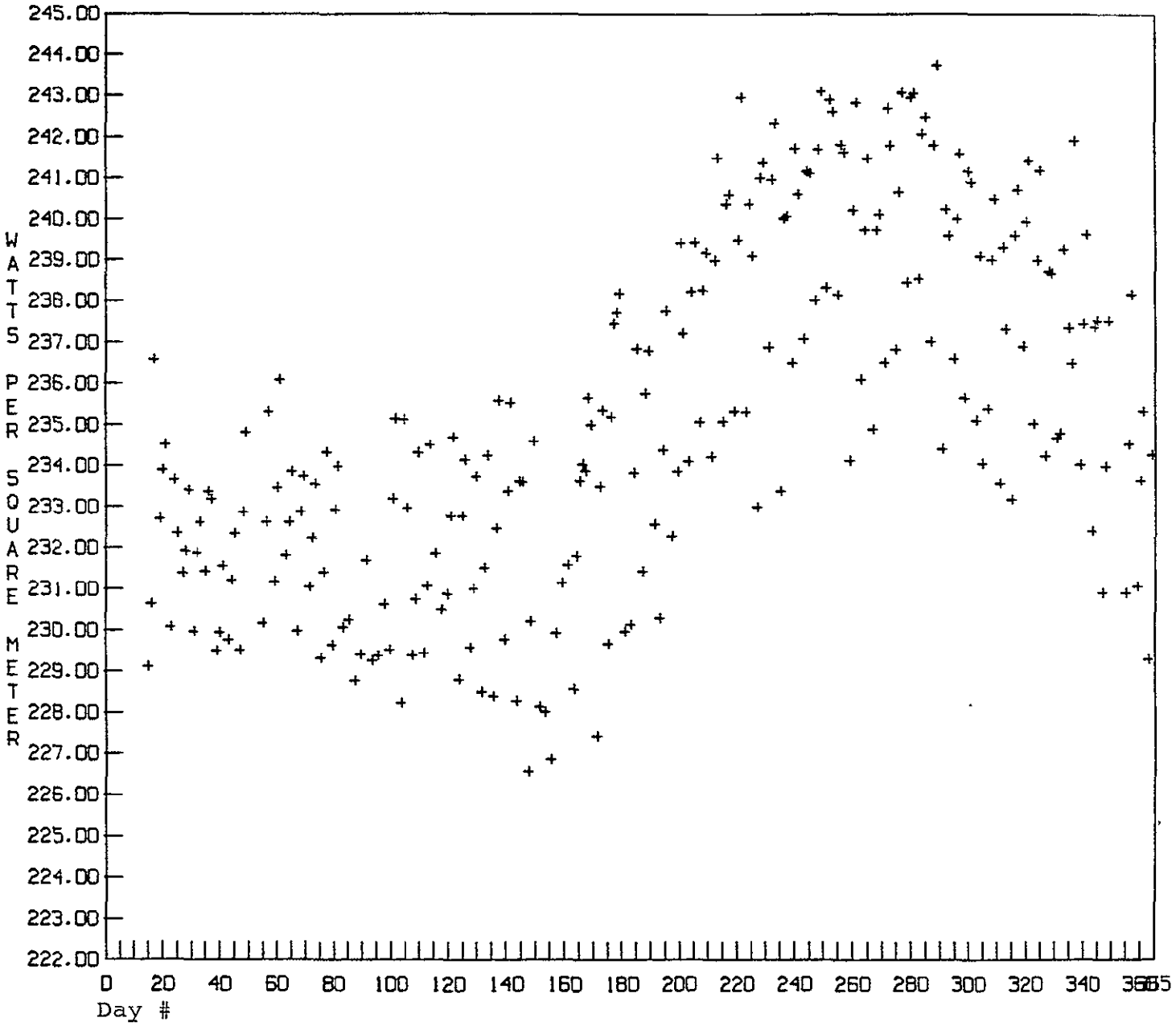

GLOBAL AVERAGE FOR NFOV LW FLUX (AN)

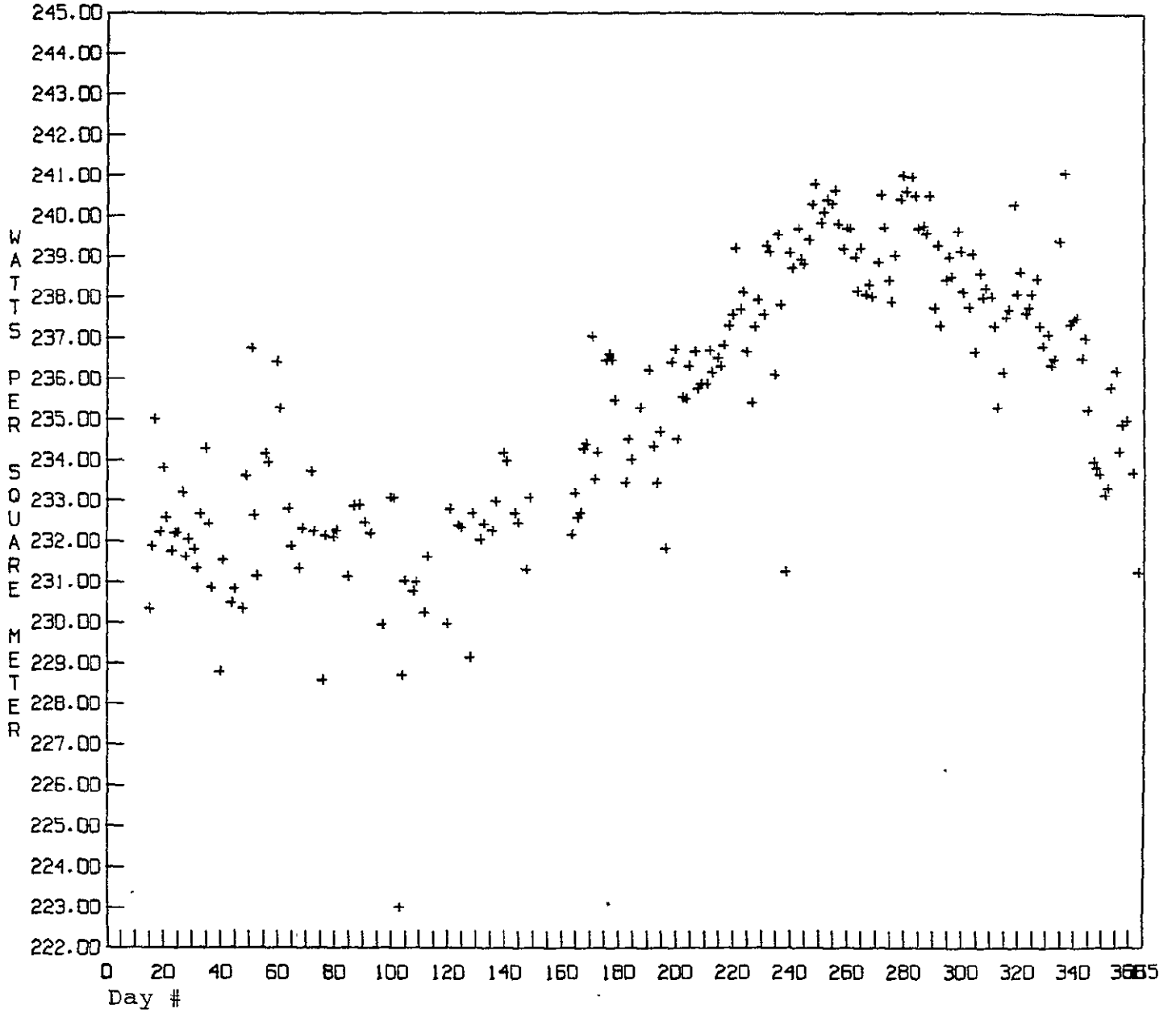

GLOBAL AVERAGE FOR WFOV LW FLUX (DN)

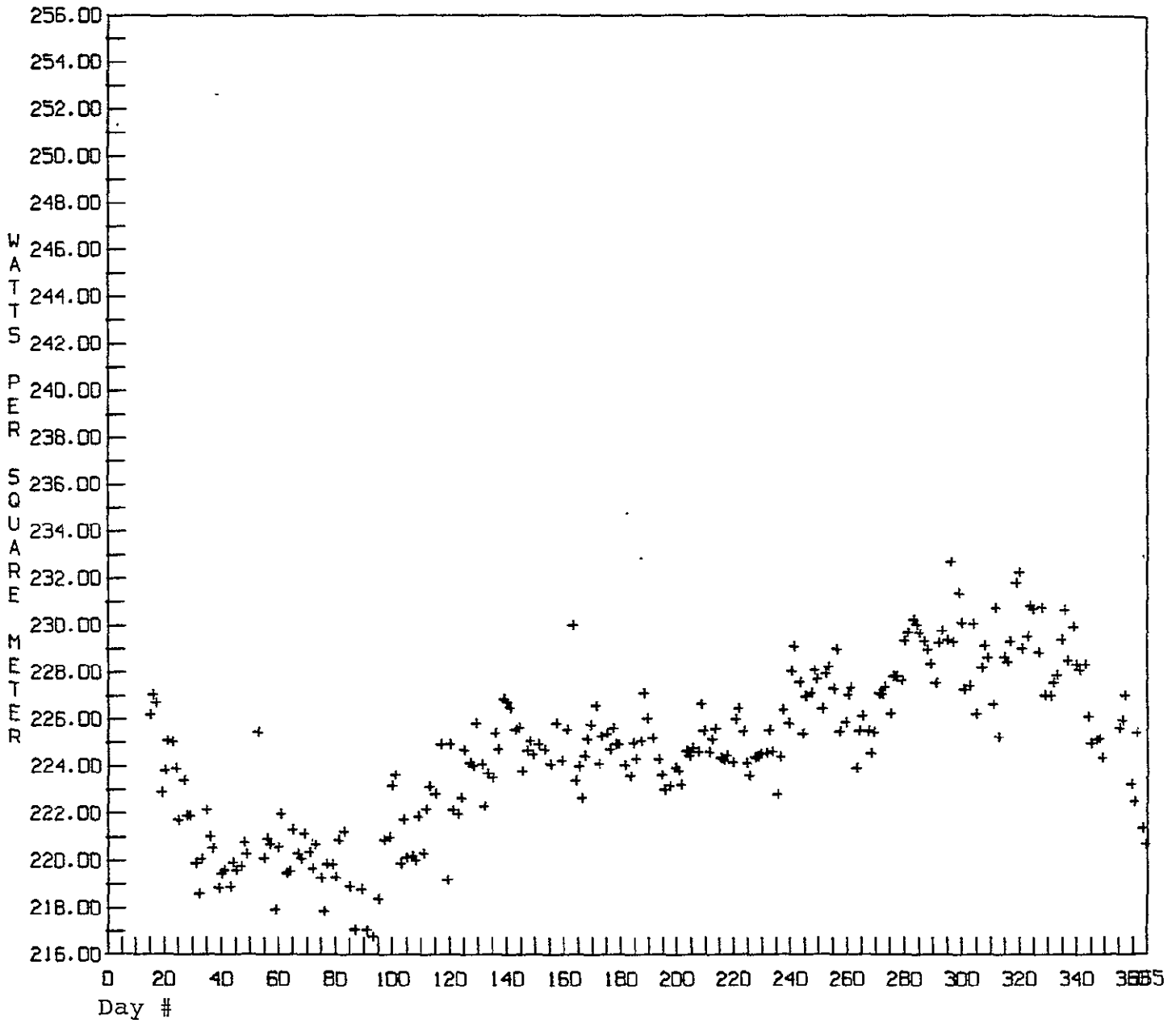

GLOBAL AVERAGE FOR NFOV LW FLUX (DN)

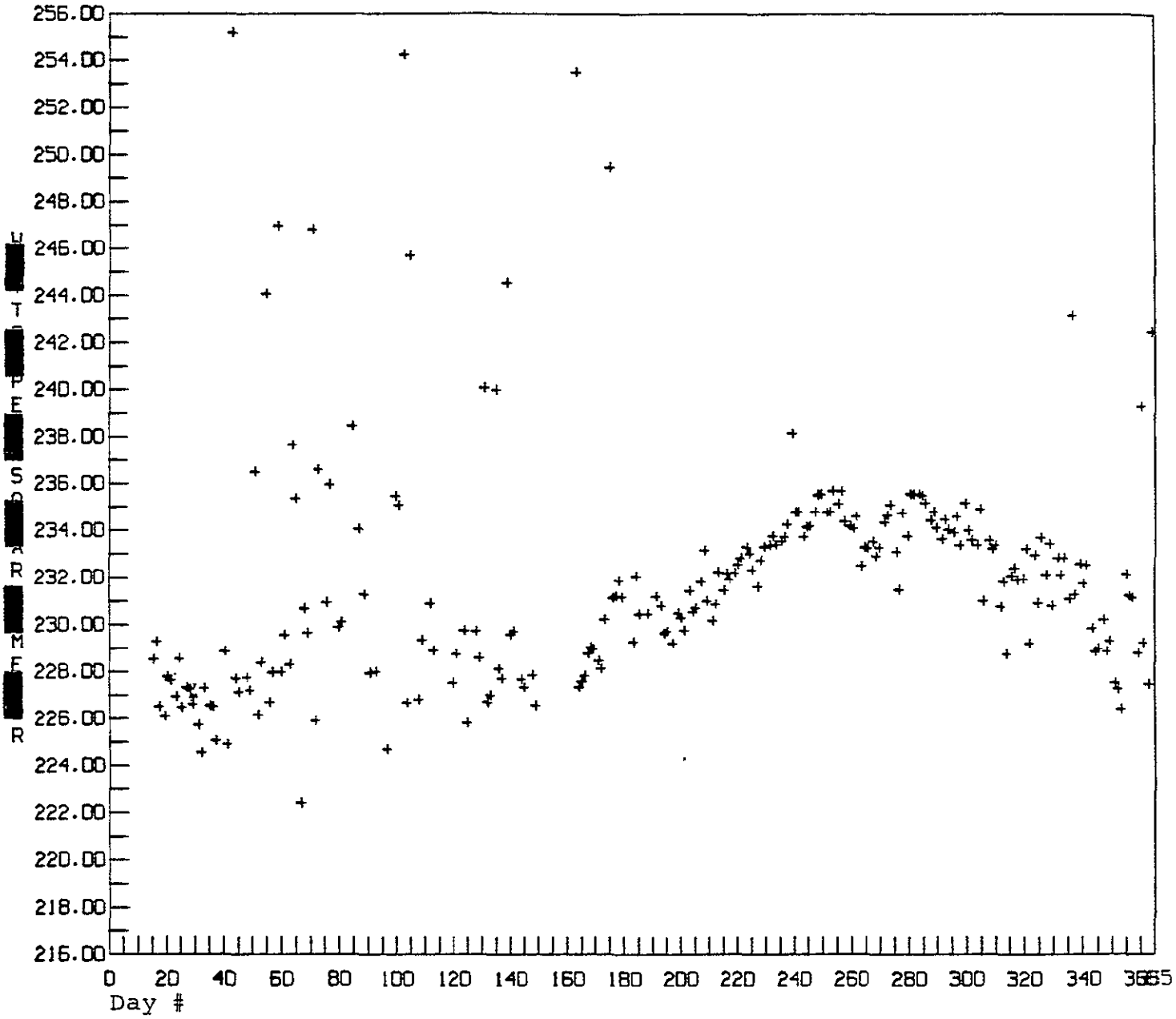

GLOBAL AVERAGE FOR NFOV LW FLUX (AVERAGE OF AN & DN)

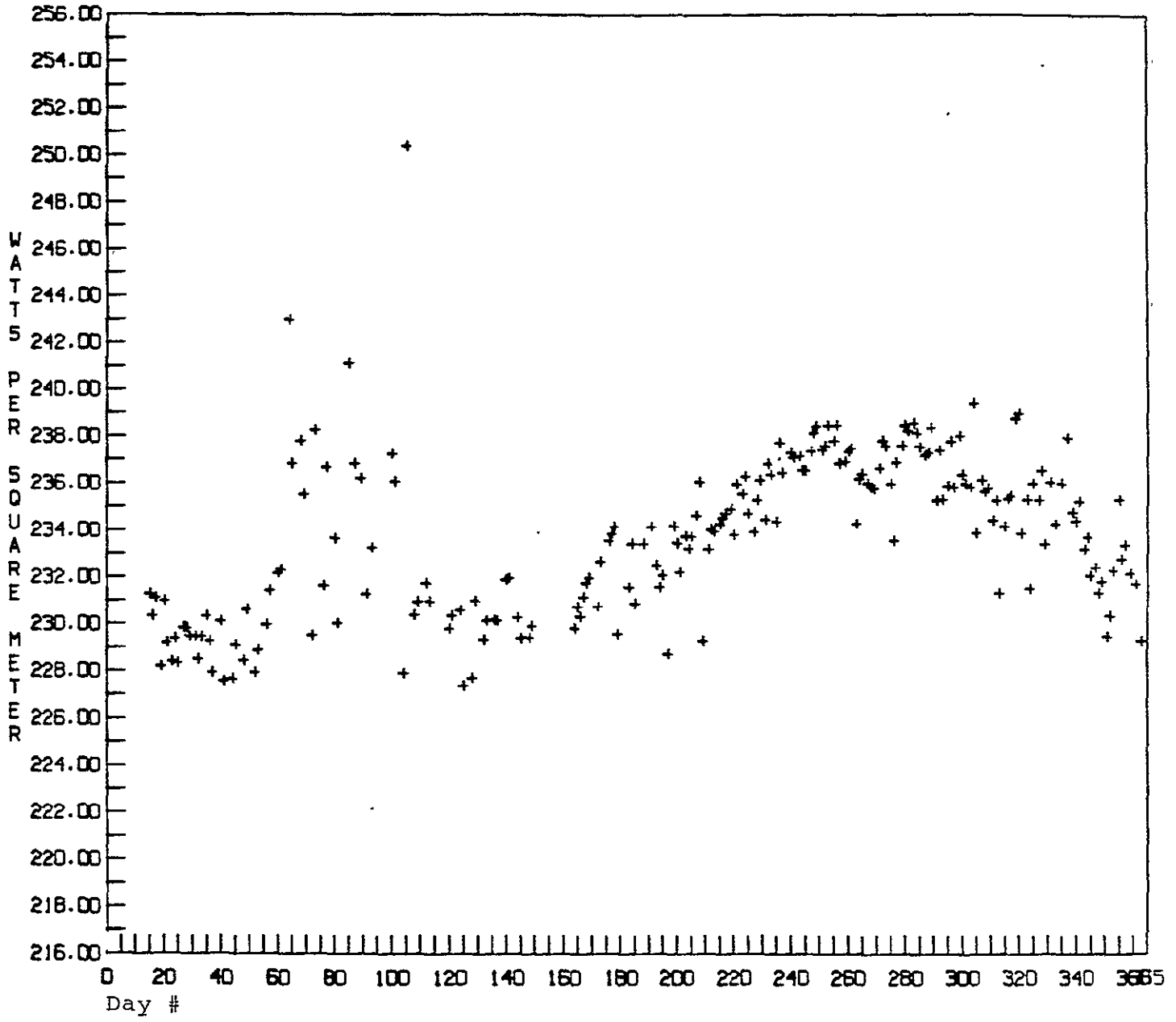

GLOBAL AVERAGE FOR NFOV LW FLUX (AVERAGE OF AN & DN)

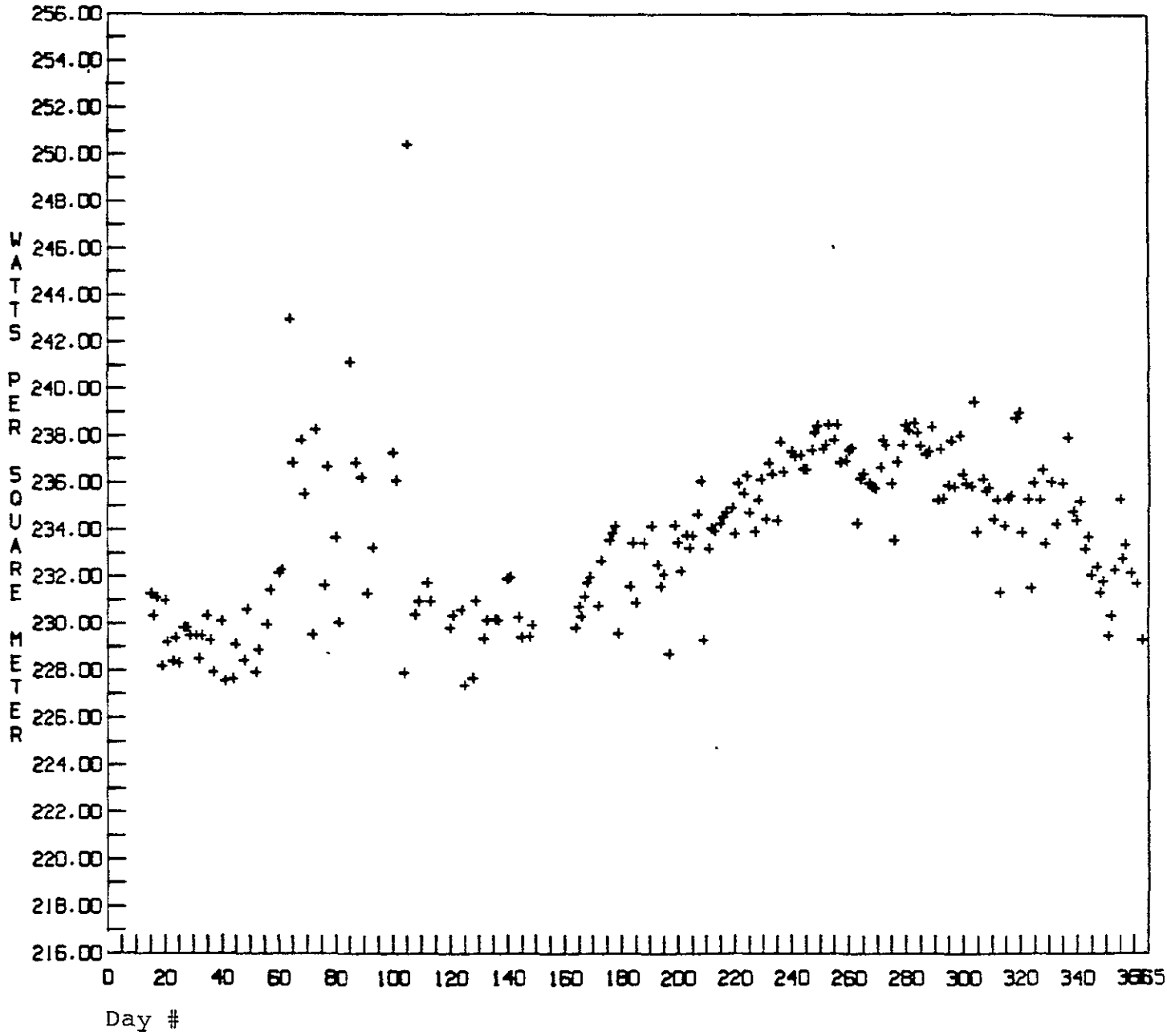

GLOBAL AVERAGE FOR WFOV ALBEDO

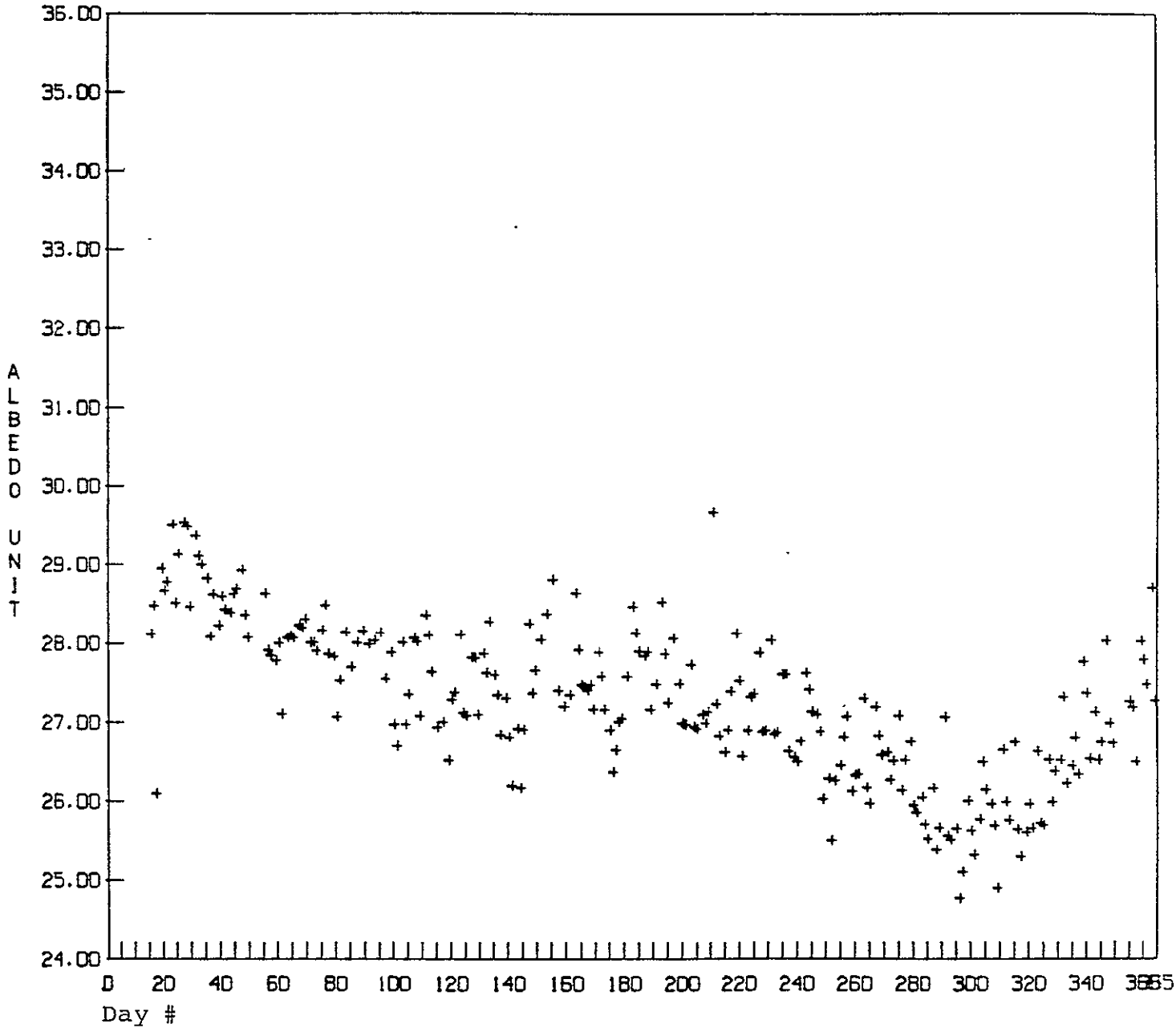

GLOBAL AVERAGE FOR NFOV ALBEDO

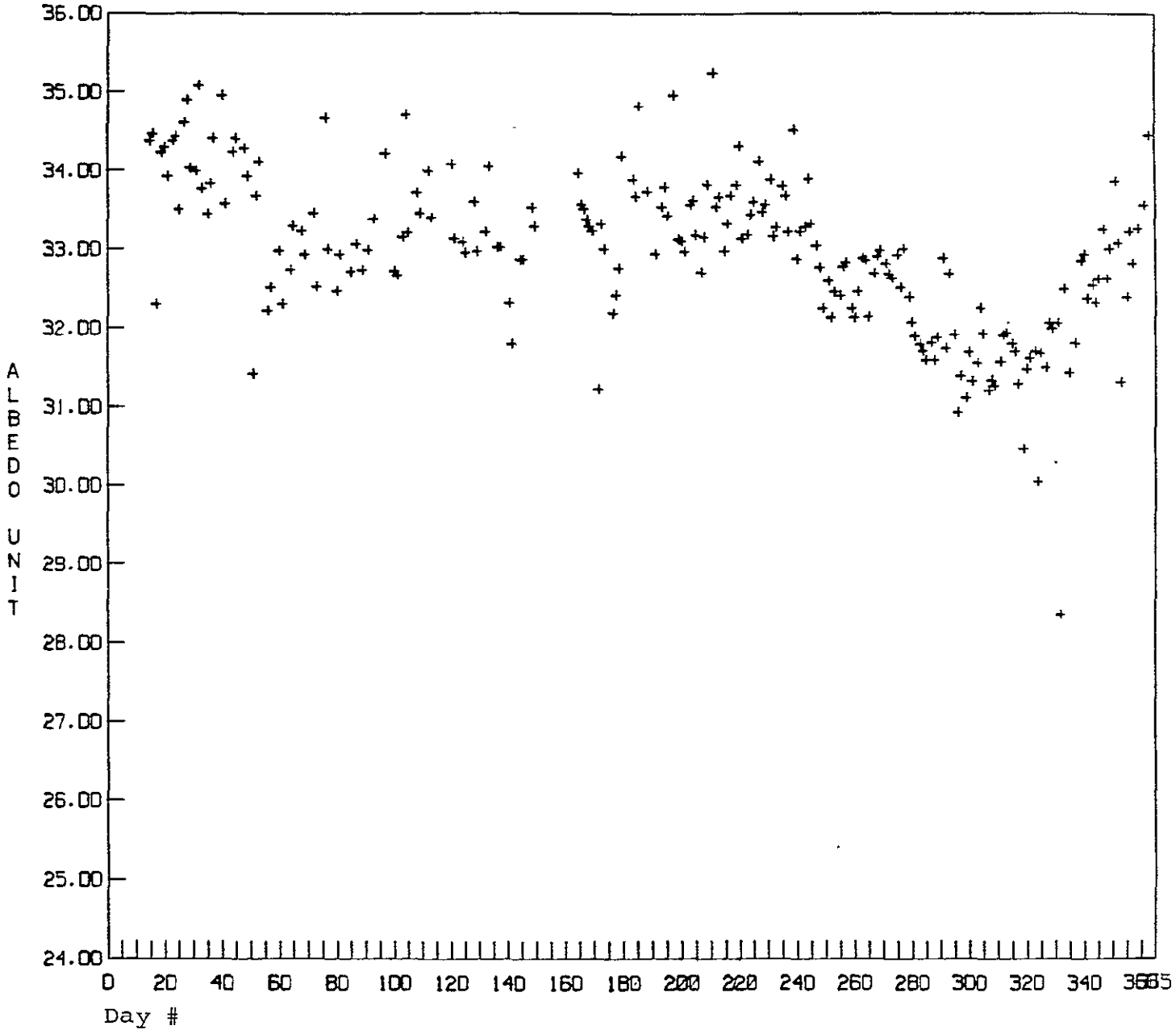

GLOBAL AVERAGE FOR WFOV NET RADIATION

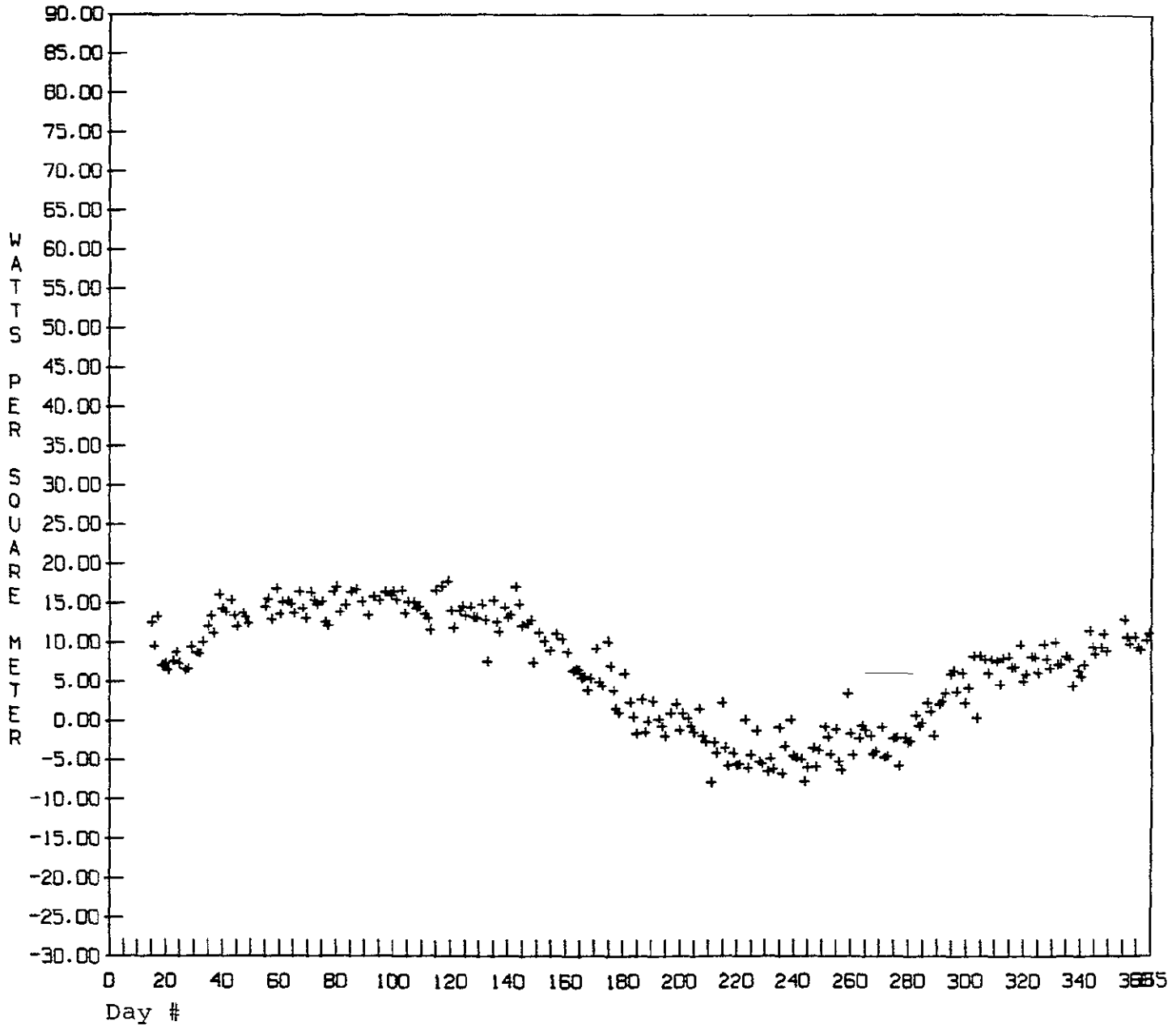

GLOBAL AVERAGE FOR NFOV NET RADIATION

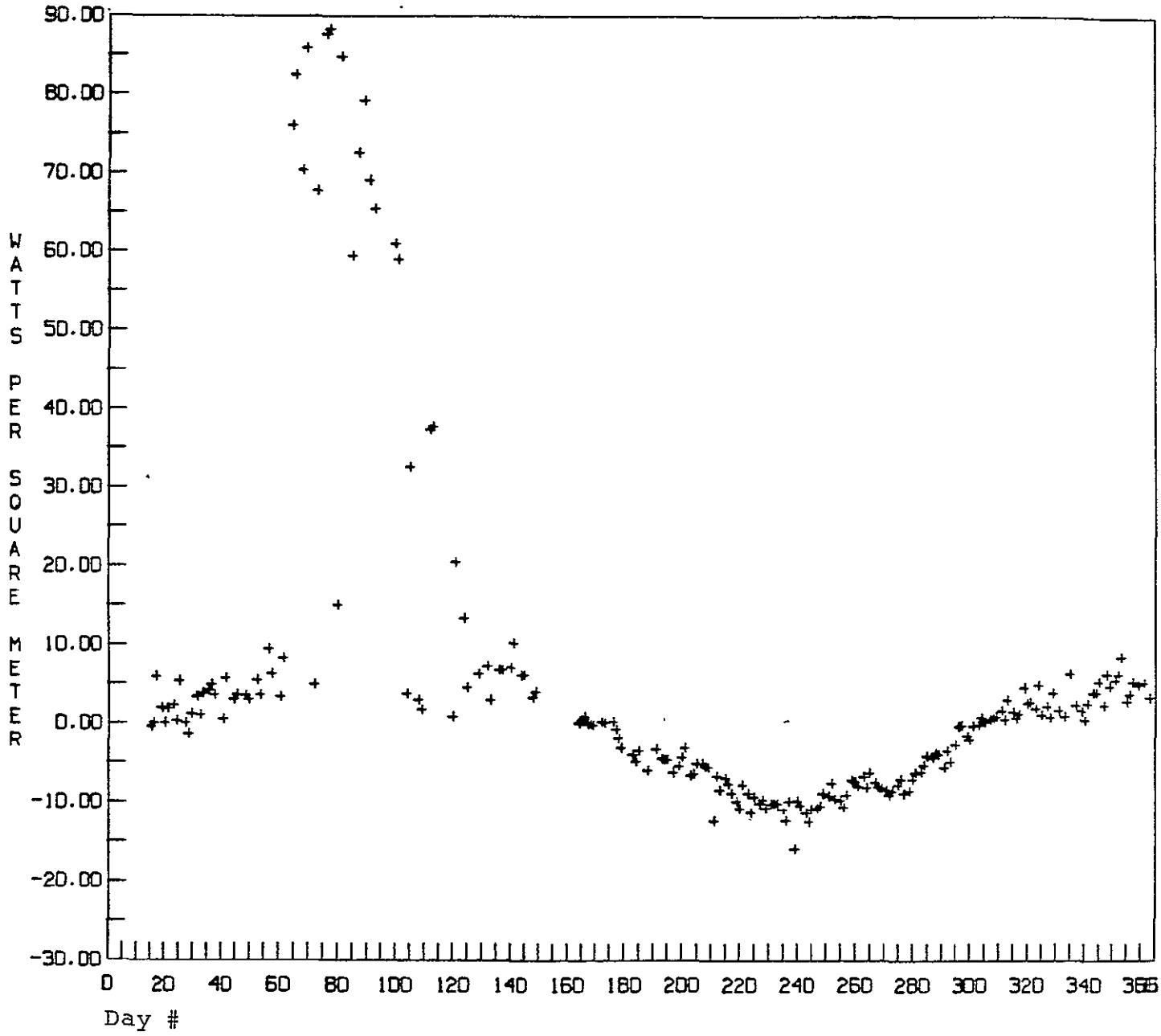

APPENDIX E.

Global and Hemispherical Average Plots

Plots of the monthly global and hemispherical averages of the principal MATRIX scientific parameters for Year-1 are presented. The data covers the period from November 16, 1978 to October 31, 1979.

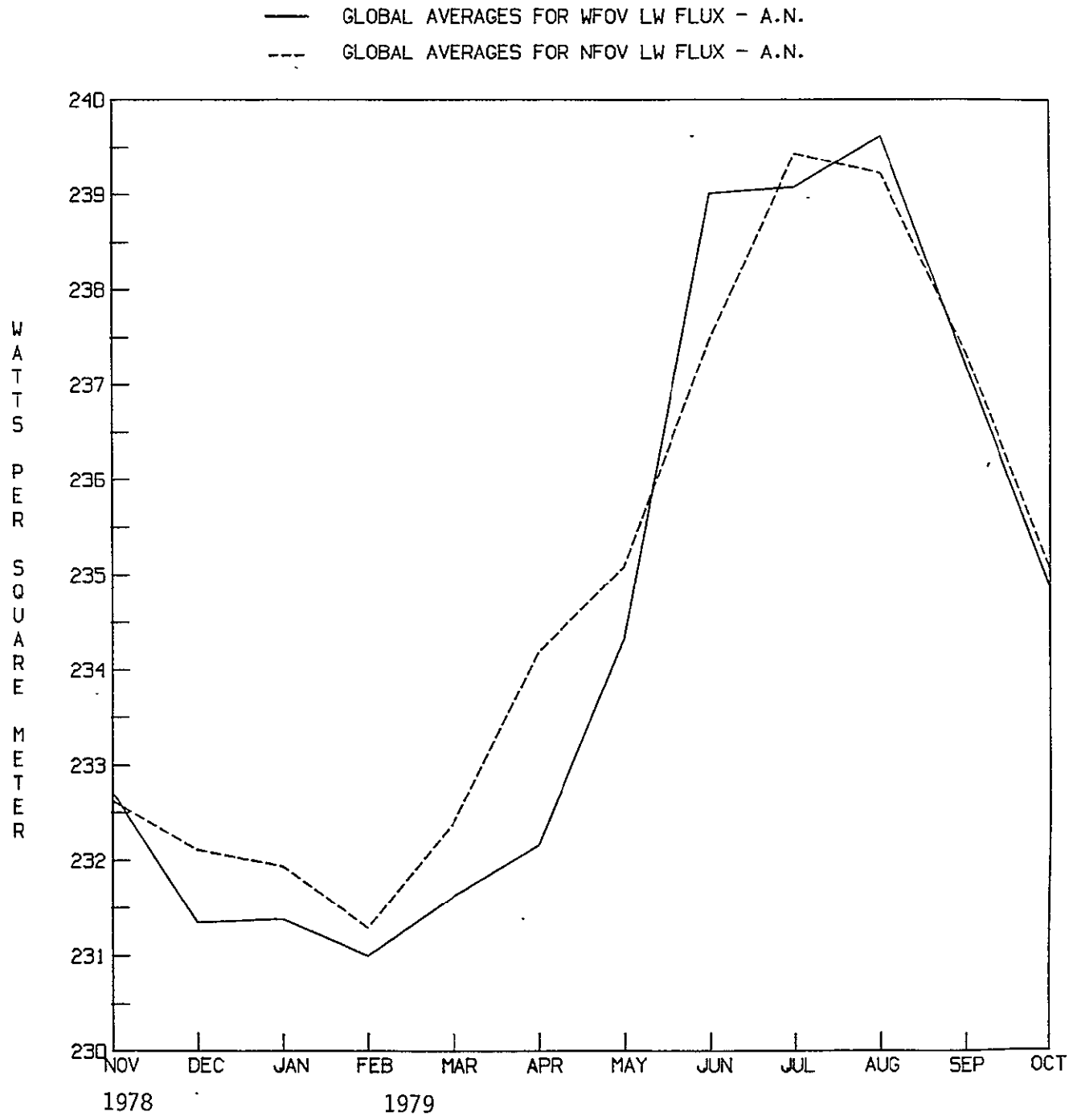

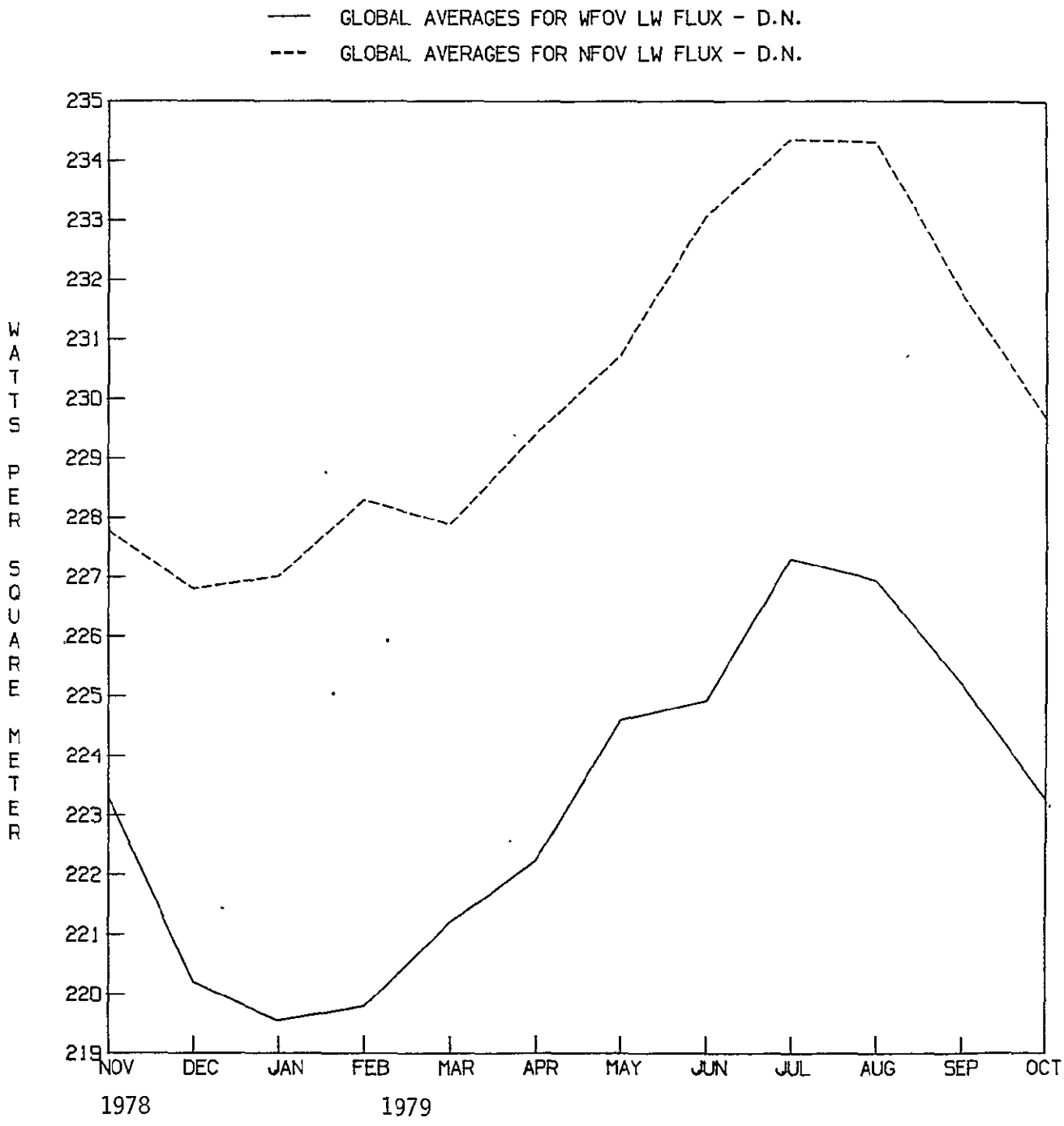

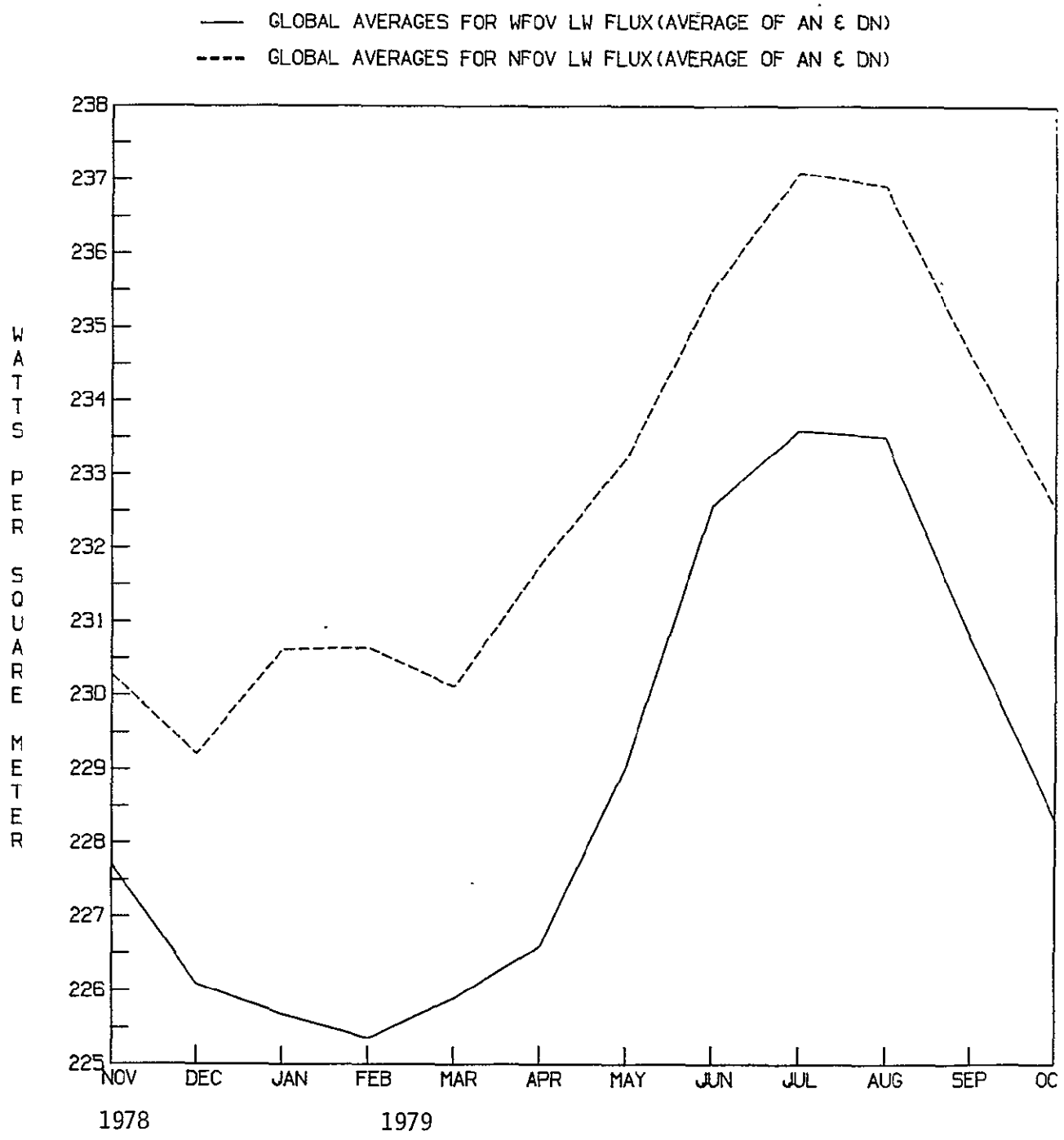

HEMISPHERICAL AVERAGES FOR L.W. FLUX - A.N.

—— - OBSERVATION FROM WIDE FIELD OF VIEW

---- - OBSERVATION FROM NARROW FIELD OF VIEW

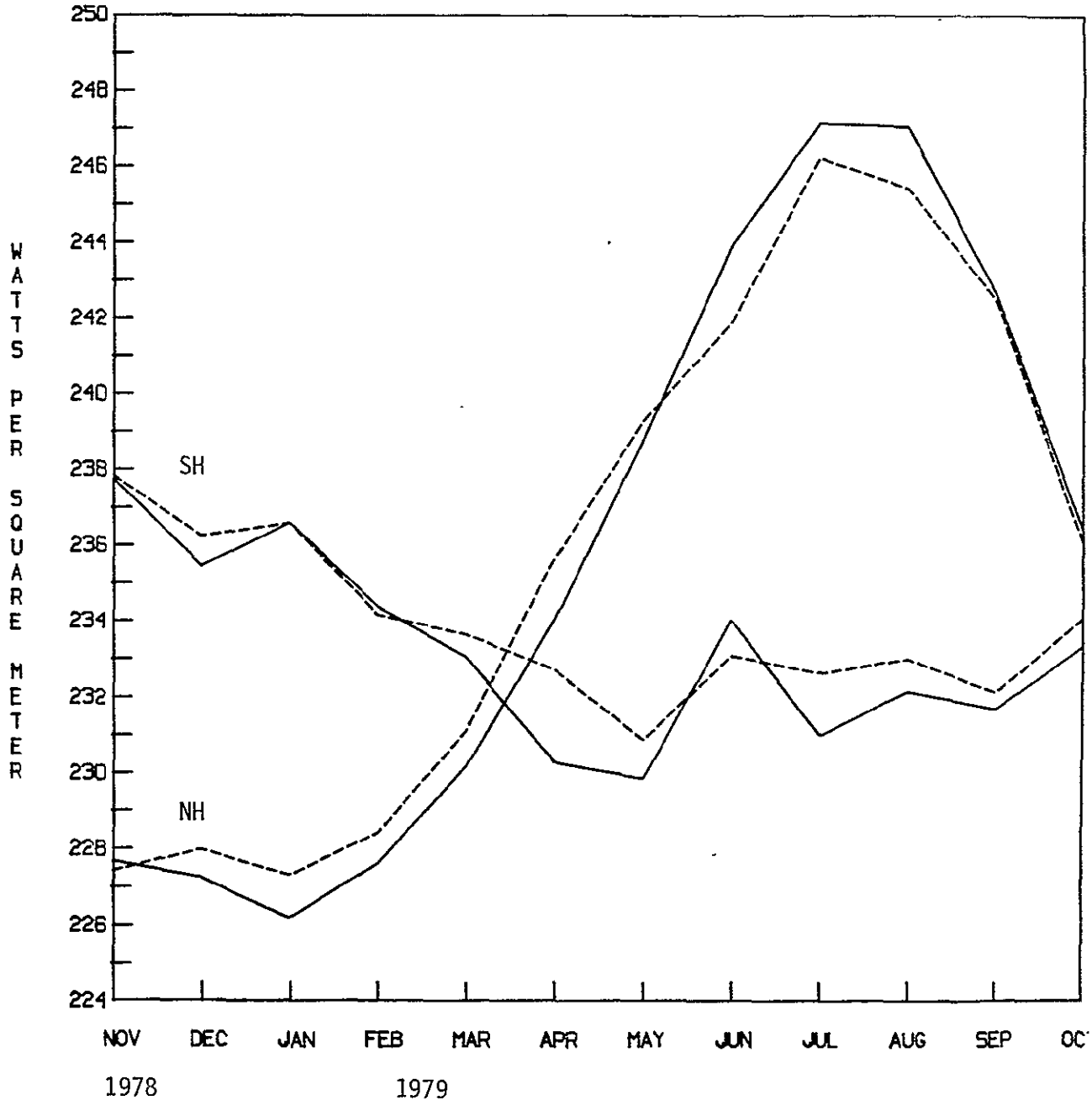

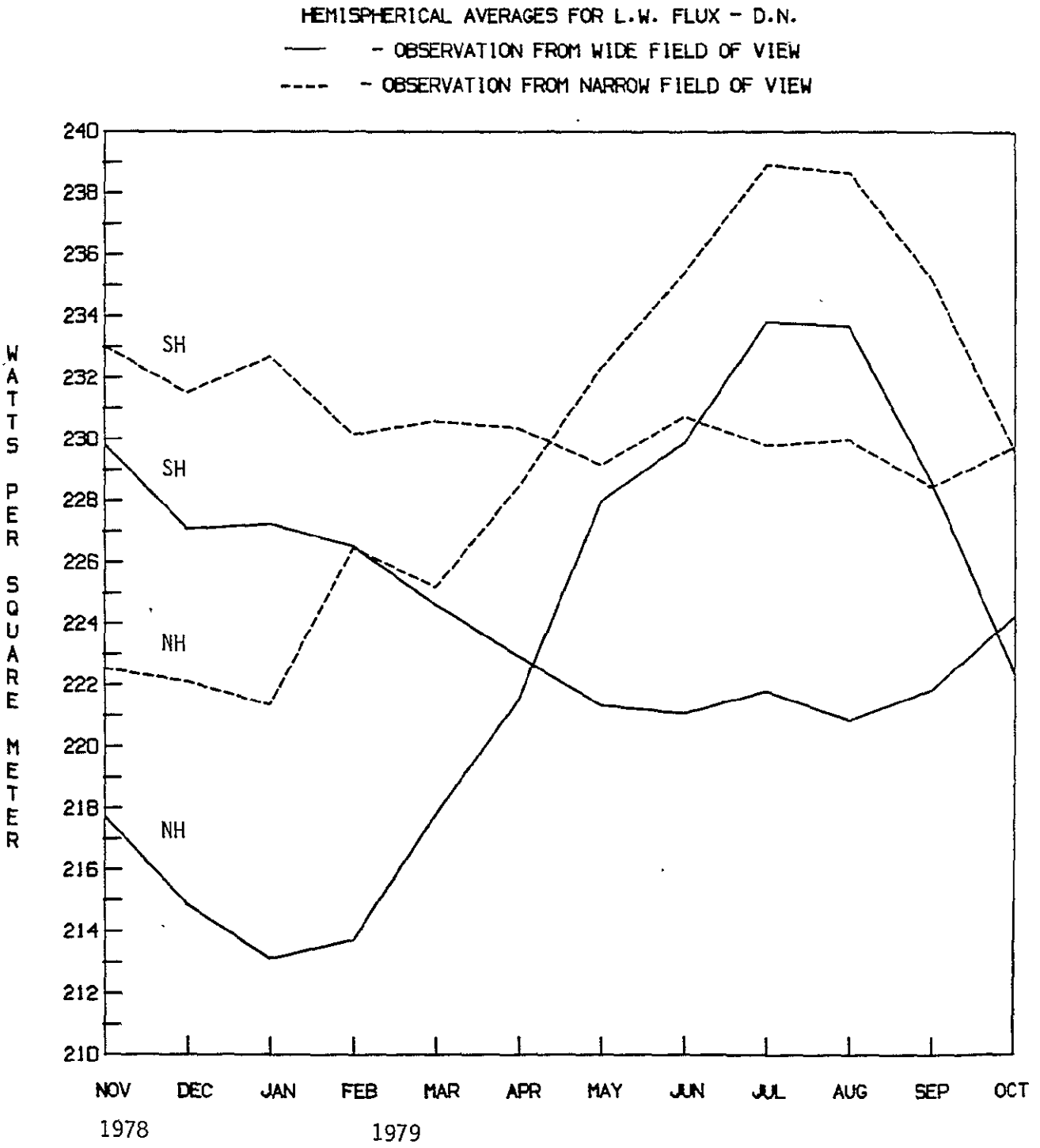

APPENDIX F.

Notes on the MATRIX Film Products

Several general comments can be made concerning the MATRIX film products. Short discussions of these are given in the following sections.

F.1 LIMS Compromise

The LIMS Compromise shows up dramatically in the film products. The population density diagrams indicate the full impact of this problem. During the months of January and February (and early March), the Northern Hemisphere polar stereographic projections show zero or sparse sampling for the NFOV LW data populations. The problem shows up very well on the mercator projection also.

Missing data is indicated in the contour products by broken contour lines. In the case of the LIMS Compromise, there are no contours in the region where the Compromise was in effect.

F.2 Sparse Data on WFOV Net Radiation Cyclic Contours

The 6-day cyclic averages are meant to provide results for net radiation at periods corresponding to complete global coverage by the spacecraft. However, the ON-OFF duty cycle of the ERB instrument causes lack of complete global coverage during the 6-day period. On the film products this shows up as data gaps on the WFOV cyclic contours. That is, there are broken contour lines on the WFOV cyclic net radiation contours. These are aesthetically unappealing but should not cause any sampling problems in the cyclic averages.

F.3 Normalized Dispersion of WFOV Albedo

The contour plots for the normalized dispersion of WFOV albedo show very dense contours. The plots appear to have a number of regions where there are actually spikes which produce the dense contours. This parameter measures the fluctuations of the daily averaged albedo for a target area about the mean of the daily albedos for that target area. The dense contours indicate that there are target areas (or groups of target areas) for which large day-to-day fluctuations occur in the values of WFOV albedo. This is not completely unexpected in view of the previously discussed fluctuations in latitude band averages (see Subsection 1.3.3). These dense contours do not indicate that the monthly average of WFOV albedo is unreliable.

C-3

F.4 Standard Deviation of NFOV Net Radiation

The standard deviation of NFOV net radiation show very dense contours. The same discussion applies here that was given in Section F.3.

F.5 Spikes in the WFOV DN LW Flux

Sharp spikes appear in the contour plots of WFOV DN LW flux for the months of February and August, 1979. (Other spikes may appear in the contour products in addition to these). The spikes are indicated by very dense, highly localized, closed contour lines at the following locations:

February : 0° Longitude, 40° N. Latitude

10° E. Longitude, 40° N. Latitude

August : 20° E. Longitude, 50° N. Latitude

These spikes in LW flux are well correlated with spikes in the Normalized Dispersion of WFOV LW flux. An important note to users is that contour plots of the statistical parameters should be used to check for spikes or other anomalous behavior in the MATRIX parameter contour plots. In this manner, users can assure that scientific studies involving specific geographic regions are not biased by instrument noise or statistical breakdowns. The statistical parameter contour plots are recommended as a valuable cross-check on the quality of the MATRIX data.

APPENDIX G.

REFERENCES

1) "User's Guide for ERB-7 MAT", NASA Contractor Report CR-170514, Brian S. Groveman, Research and Data Systems, April 1984.

2) "ERB-7 Channel 13 Sensitivity Study, November 1978 - October 1979", Parmesh Hari Dwivedi, Research and Data Systems, April 1982.

3) "The In-flight Asymmetric Degradation and Recovery of Earth Radiation Budget SW Radiometers", Preliminary Task Report, Phillip Ardanuy, Research and Data Systems, August 1982.

4) "Nimbus-7 ERB MATRIX Scientific Algorithms", NASA Reference Publication, Dr. Richard J. Tighe, Systems and Applied Sciences Corporation, February 1983.

5) Kyle, H.L., F.B. House, P.E. Ardanuy, H. Jacobowitz, R.H. Maschhoff and J.R. Hickey, "New In-flight Calibration Adjustment of the Nimbus-6 and -7 Earth Radiation Budget Wide Field of View Radiometers", submitted to J. Geophys. Res. (1983).

6) Maschhoff R.H., A. Jalink, J. Hickey and J. Swedberg, "Nimbus Earth Radiation Budget Censor Characterization for Improved Data Reduction Fidelity", submitted to J. Geophys. Res., (1983).

7) "Minutes of the ERB Calibration Workshop", NASA/Goddard Space Fight Center, August 4-5, 1982, Greenbelt, Maryland 20771.